DISSERTATION

SUBMITTED TO THE

COMBINED FACULTIES OF THE NATURAL SCIENCES AND MATHEMATICS

OF THE RUPERTO-CAROLA-UNIVERSITY OF HEIDELBERG, GERMANY

FOR THE DEGREE OF

DOCTOR OF NATURAL SCIENCES

DISSERTATION

PUT FORWARD BY

RORY HOLMES

BORN IN: BIRKENHEAD, UNITED KINGDOM

ORAL EXAMINATION: DECEMBER $14^{th}$, 2011

# THE NEAR-INFRARED IMAGING CHANNEL FOR THE EUCLID DARK ENERGY MISSION

# DEVELOPMENT OF CRITICAL OPTOMECHANICAL COMPONENTS AND AN INSTRUMENT CALIBRATION CONCEPT

REFEREES: PROF. DR. HANS-WALTER RIX
PROF. DR. ANDREAS QUIRRENBACH

I would like to dedicate this thesis to two good friends lost along the way: Frithjof Brauer and Crystal Brasseur.

**Abstract**

This thesis describes a number of instrumentation and mission design developments performed to prepare the European Space Agency's (ESA's) Euclid Mission. This space-based mission will enable unprecedented experimental probes of the nature of dark energy. As the Near-Infrared Photometry Scientist – one of three Instrument Scientists within the Euclid Consortium – my work focused on the mission's near-infrared photometric channel, which is required for the photometric redshift measurements of the $\sim 1.5$ billion galaxies within the large Euclid imaging survey. This thesis addresses and solves a range of specific problems relating to implementation of this channel, with the ultimate goal of proving mission feasibility during the selection process of ESA's Cosmic Vision Program. To that end, this thesis details requirement breakdowns and error budgets used to translate scientific requirements into lower level instrument requirements. The performance validation of the baseline implementation of the mission against high level requirements has formed an important part of the mission verification process; those applicable to the photometric channel are presented in this thesis. I have also developed a calibration strategy to meet the channel's stringent high level calibration requirement. This includes specific work on optimizing the survey strategy for the retrospective calibration of the survey-wide dataset and also hardware development relating to a potential implementation of an internal flat-field calibration source. An assessment of the channel's critical, single-point-failure filter wheel mechanism – which is needed to allow multi-band near-infrared photometry – is also detailed.

Much of this effort has been incorporated into official Euclid documentation that has formed the basis of the Euclid Consortium's response to the Cosmic Vision Program selection process. The baseline implementation of the near-infrared photometric channel, the performance of which was under my stewardship, meets all the high level science requirements.

## Zusammenfassung

Diese Doktorarbeit beschreibt die Entwicklung verschiedener Instrumentierungs- und Missionskonzepte in Vorbereitung auf die ESA (European Space Agency) Euclid Mission. Ziel der Euclid Mission ist es, die Natur der dunklen Energie mit bisher unerreichter Genauigkeit zu untersuchen. In meiner Position als verantwortlicher Wissenschaftler für den Nahinfrarot-Photometrie-Bereich (im Euclid Konsortium gibt es insgesamt drei Instrumente, mit je einem verantwortlichen Wissenschaftler) habe ich mich insbesondere mit dem Nahinfrarot-Photometrie-Instrument auseinandergesetzt, welches für photometrische Rotverschiebungsmessungen von mehr als 1.5 Milliarden Galaxien in der großen Euclid Durchmusterung genutzt werden soll. In dieser Arbeit untersuche ich eine Vielzahl von Problemstellungen, welche die Implementierung dieses Photometriekanals in die Mission betreffen. Die von mir erarbeiteten Lösungen zeigen, dass die Missionsziele erreicht werden können. Der Nachweis dieser Machbarkeit ist essenziell in Hinblick auf den weiteren Auswahlprozess im ESA Cosmic Vision Programm. In dieser Arbeit leite ich Missionsanforderungen und Fehlerbudgets ab, um die wissenschaftlichen Zielsetzungen in Anforderungen auf Instrumentierungsebene zu überführen. Einen wichtigen Anteil am Nachweis der Missionsmachbarkeit stellen die Funktionsbewertungen des Instrumentierungskonzepts in Hinblick auf das Erreichen der wichtigsten wissenschaftlichen Anforderungen dar. Daher sind die Funktionsbewertungen für den photometrischen Kanal ebenfalls aufgeführt. Um die hohen Anforderungen an die Kalibrierung des Nahinfrarot-Photometrie-Kanals erfüllen zu können, habe ich eine Kalibrierungsstrategie entwickelt. Spezielles Augenmerk lag dabei auf der Optimierung der Durchmusterungsstrategie für die nachträgliche Kalibrierung der Gesamtheit der wissenschaftlichen Daten sowie an der Entwicklung von Komponenten für eine potenzielle Einbindung einer internen 'flat-field' Kalibrierungsquelle. Des Weiteren wurde eine detaillierte Untersuchung des Filterradmechanismus durchgeführt. Diese systemkritische Komponente, für die es keine Redundanz gibt, wird benötigt um photometrische Messungen in verschiedenen Bändern des Nahinfraroten durchführen zu können. Viele der in dieser Arbeit gewonnen Erkenntnisse sind in die offizielle Euclid-Projekt-Dokumentation eingeflossen. Diese Dokumentation bildet die Grundlage der Antwort des Euclid Konsortiums für das weitere Auswahlverfahren im Cosmic Vision Programm der ESA. Das Instrumentierungskonzept für den Euclid Nahinfrarot-Photometrie-Kanal, welches unter meiner Verantwortung entwickelt worden ist, erfüllt alle grundlegenden wissenschaftlichen Anforderungen.

# Contents

# List of Figures

# List of Tables

# Chapter 1

# Introduction

The Euclid Space Mission promises to tackle one of the most fundamental physics questions of our time: what is the nature of dark energy? The successful implementation of the Euclid Mission, however, is a formidable technological challenge. Astrophysical instrumentation and mission development for the Euclid Mission is at the heart of this thesis, not the physics of dark energy and its consequences. Nonetheless, I start by laying out the science case for the Euclid mission, which is well documented in the *Euclid Assessment Report* [1], the *Euclid Development Report* [2] and the report by the *ESA-ESO Working Group on Fundamental Cosmology* [3]. I draw much of the introductory material from these documents. I first start by introducing the problem that the Euclid Mission will aim to address in Subsection 1.1.1, namely our understanding of the mysterious "dark sector" of our Universe. Subsection 1.1.2 goes on to detail the science probes that the Euclid Mission will utilize to constrain the dark Universe: Weak Lensing and Galaxy Clustering. Even though there are secondary science probes planned, the baseline implementation of the mission is optimized for these two probes alone. The required surveys and the case for a space based mission are outlined in Subsection 1.1.3, before I turn to a detailed introduction of the current implementation of the Euclid Mission in Section 1.2, and how it is optimized for these science probes. In Subsection 1.2.5, I go on to introduce the Euclid Mission's near-infrared instrument that this thesis is based on. In this context it proves unavoidable to outline the rather complex programmatic changes that the mission has gone through during the last three turbulent years; I do this in Subsection 1.2.3. Section 1.3 goes on to detail the scope of the work presented in this thesis. Since Euclid is being developed by a large number of people ($> 800$ at the last count), I have collaborated with a number of people during the course of this work. Our work is often heavily intertwined and therefore I spend the final section in this chapter (Section 1.4) detailing my main collaborations.

# 1.1 The Euclid Science Case

## 1.1.1 The Dark Universe

Our view of the Universe is incomplete. The laws of nature we are used to living with on a day-to-day basis cannot be translated to the large scale Universe. Either our theory of gravity is incorrect on large scales, or there is a significant hitherto unobserved contribution to the mass-energy content of the Universe. Which of the two options, if either, is correct? This is one of the most important questions in modern physics, and one that the Euclid Mission aims to answer.

The concordance cosmological model, which is built upon Einstein's theory of General Relativity, explains our observations of the Universe on large scales well. But this model's success requires the introduction of two hitherto unobserved constituents of our Universe: dark matter and dark energy, which would account for 20 % and 76 % of the mass-energy content in the Universe respectively. In this view, dark matter is a substance that gravitationally interacts in the standard way, but does not absorb or emit light. The nature of dark energy is less constrained, although this is the quantity driving the acceleration of the Universe's expansion in this model.

It is fruitful to delve into a more mathematical description of the problem. From Einstein's General Relativity, under the constraints of a homogeneous and isotropic Universe, it is possible to derive the Friedmann equation for the time dependence of the Universe's scale factor $a(t)$. The scale factor relates proper distances to comoving distances, and therefore encapsulates the expansion rate of the Universe. The Friedmann equation is often cast in terms of the Hubble parameter $H$:

$$H^2(t) = \left[\frac{\dot{a}(t)}{a(t)}\right]^2 = H_0^2 \left(\frac{\Omega_\mathrm{R}}{a^4(t)} + \frac{\Omega_\mathrm{M}}{a^3(t)} + \frac{\Omega_\mathrm{K}}{a^2(t)} + \Omega_\nu \, e^{-\int 3\,[w(a)+1]\,\mathrm{d}\ln a}\right) \quad , \tag{1.1}$$

where $H_0^2$ is the current value of the Hubble parameter, $a$ is the cosmological scale factor and $\Omega_\mathrm{R}$ is the fractional energy density currently in radiation, $\Omega_\mathrm{M}$ in matter and $\Omega_\mathrm{K}$ in curvature. For a flat Universe, which recent observations suggest, then $\Omega_\mathrm{K} = 0$ with the remaining fractional energy densities summing to unity for all times. The $\Omega_\nu \, e^{-\int 3\,[w(a)+1]\,\mathrm{d}\ln a}$ contribution comes from a very general consideration of the nature of dark energy, with its equation of state parameter $w(a) = P(a)/\rho(a)\,c^2$ relating its pressure $P$ to its density $\rho$. From simply considering the limiting cases in Equation 1.1, it is clear to see that it is only the contribution from the $\Omega_\nu$ term that can lead to the observed accelerating expansion of the Universe. Particularly, only dark energy with an equation of state parameter $w < -1/3$ could lead to such an expansion. If dark energy is just a cosmological constant with $w = -1$, as Einstein first proposed, then this term would reduce to a constant: $\Omega_\nu \, e^{-\int 3\,[w(a)+1]\,\mathrm{d}\ln a} \to \Omega_\Lambda$. This case of a (dominant) cosmological constant would lead to an exponentially accelerated expansion of the Universe. Different dark energy models require different values and evolutions of the equation of state parameter, which can be simply expanded as $w(a) = w_0 + w_a\,(1-a)$. The Euclid mission aims to distinguish between the different theories of dark energy by precisely measuring the current value $w_0$ of this quantity, and its evolution with time $w_a$. An alternative explanation could be that one of the pillars that the concordance cosmological model is built on is wrong; the General Relativity theory of gravity, which has been precisely confirmed on small-scales, may need modifying on cosmological scales. The Euclid Mission will distinguish between these different possibilities by measuring the Universe's expansion history and the growth of large-scale structure.

### 1.1.2 The Euclid Mission's Primary Science Probes

Different models for dark energy lead to different behaviors of the cosmological scale factor $a(t)$, which will in turn affect the angular diameter distances and the rate of structure growth in the Universe (see below). Euclid will provide highly accurate constraints on the angular diameter distances and on the structure growth rate to differentiate such dark energy models. In most cases, the most notable observational differences occur at a redshift $z$[1] between $0.5 < z < 1.5$. The Euclid Mission will sample this range extensively as it reaches out to a depth of $z \sim 2$; a time when the Universe was only a quarter of its current age. By measuring (statistically) the growth of matter inhomogeneities at these different epochs, the Euclid Mission will be able to investigate both the growth of structure and the Universe's expansion history. Distances in the Universe depend on its expansion history. For example, in a flat Universe, the comoving transverse distance to an object is given by

$$D_{\rm tran}(z) = \int_0^z \frac{c}{H(z')} {\rm d}z' \quad , \tag{1.2}$$

where $c$ is the speed of light and $H(z)$ is the Hubble parameter, which depends on the object's redshift $z$. The comoving angular diameter distance can be related to this as

$$D_{\rm ang}(z) = \frac{D_{\rm tran}(z)}{1+z} \quad . \tag{1.3}$$

Distance measurements at different redshifts can therefore be used to probe the evolution of the Hubble parameter $H$, which can then be used to investigate the evolution of the fractional energy densities in the Universe (Equation 1.1).

The growth of large scale structure in the Universe is sensitive to the competition between the expansion of the Universe, which damps growth, and gravity. Measurements of this growth can not only probe the expansion history, but also test the theory of gravity directly. By considering how perturbations grow in an almost smooth, expanding Universe it is possible to arrive at an equation for the relative density contrast $\delta = \delta\rho/\rho_0$, for a perturbation $\delta\rho$ to the uniform background energy density $\rho_0$. In a simplified form, applicable to late epochs and the linear perturbation regime, this becomes

$$\ddot{\delta}_k + 2\,\frac{\dot{a}(t)}{a(t)}\,\dot{\delta}_k = \delta\left(4\,\pi\,G\,\rho_m - \frac{c_s^2\,k^2}{a^2(t)}\right) \quad , \tag{1.4}$$

[1] $a(t) = (1+z)^{-1}$

where $a$ is the cosmological scale factor, $G$ is the gravitational constant, $\rho_m$ is the fractional density of matter, $c_s$ is the speed of sound and $k$ is the comoving wavenumber ($2\pi$ / comoving wavelength). By measuring structures at different cosmological epochs it is possible to probe the expansion history of the Universe, which can in turn be used to investigate the evolution of the fractional energy densities, and also test General Relativity against simple modified gravity theories.

To meet the high level science goals, the Euclid Mission is optimized for two *independent* science probes: Weak Lensing and Galaxy Clustering. When combined, these two probes will allow Euclid to investigate both the growth of structure and the expansion history in more detail, as well as providing an important cross check between their individual results.

**Weak Lensing**

The Weak Lensing science probe focuses on precise shape measurements of distant galaxies. Slight perturbations to their observed shape, or "shear", caused by intermediate matter gravitationally interacting with the light are measured. Coupling this information with the observed galaxies' redshifts allows the distribution of mass, both normal and dark, in the Universe to be mapped in three dimensions. Comparing the distribution of matter at different redshifts will allow the growth of structure in the Universe to be investigated, as well as providing information on the expansion of the Universe. Two channels have been optimized on the Euclid Mission for this science probe. The high precision shape measurements of distant galaxies will be performed with a wide-field visible imager. A near-infrared channel will supplement these measurements with photometric data, which will be combined with ground-based, multi-band, visible photometry to estimate the redshift of the galaxies imaged. These photometric redshift estimates, or "photo-zs", are obtained by comparing the fluxes received from an object in different wavelength bands to identify spectral features, the wavelength position of which can be used to estimate the object's redshift. The implementation of these two channels is detailed in Sections 1.2.4 and 1.2.5. The work presented in this thesis focuses on various aspects of the near-infrared photometric channel.

**Galaxy Clustering**

The second science probe centers around the distribution of galaxies within the Universe. The Euclid Mission will incorporate a near-infrared spectrometer that will be used to precisely measure the redshifts of galaxies out to $z \sim 2$, allowing an accurate three-dimensional galaxy distribution map to be constructed. This science probe utilizes the measurements of Baryonic Acoustic Oscillations (BAO) at different cosmological epochs. In the early Universe, before recombination, sound waves formed from the interaction of gravity and pressure in the coupled matter-radiation plasma. After recombination, the characteristic wavelengths of these waves were frozen into the Cosmic Microwave Background (at $z \sim 1100$). The angular power spectrum of the resulting temperature anisotropies has been accurately constrained by missions such as WMAP [4]. Euclid will measure the descendants of these features, which will regain the large scale signal, in the power spectrum of galaxy clustering out to $z \sim 2$, again in angular coordinates. By constraining the angular diameter distance at multiple epochs, Euclid will provide a direct measure of the expansion history (Equation 1.3).

### 1.1.3 The Euclid Surveys and Legacy Science

The statistical approach of the two main science probes requires a very large survey. The Euclid Mission aims to survey over $15,000$ deg$^2$ of the extragalactic sky out to $z \sim 2$ with visible imaging, near-infrared photometry and near-infrared spectroscopy. As a result, the Euclid Mission will generate a vast dataset for legacy science including broadband visible images and near-infrared photometry of $\sim$ 1.5 billion galaxies and near-infrared spectroscopy of $\sim$ 50 million galaxies. Such a large dataset will touch on many aspects of astrophysics, on many different scales, from the formation and evolution of galaxies down to the detection of brown dwarfs.

The surveys required to meet Euclid's primary science goals can only be performed in space. The high precision visible shape measurements of lensed galaxies require highly stable imaging to prevent systematic effects dwarfing the shear signal. The turbulent nature of the atmosphere and less stable temperature environment makes such measurements from the ground very difficult. The mission also requires a deep photometric and a spectroscopic near-infrared survey. Space observations, without the bright sky background at these wavelengths, allow these surveys to be performed much more efficiently than ground-based observations. Essentially, to cover the survey area with the precision and the depth required to meet the high level science goals, there is no alternative to a space-based experiment.

In addition to the mission's $15,000$ deg$^2$ survey, called the "Wide Survey", Euclid will also perform a "Deep Survey" by regularly observing two $\sim$ 20 deg$^2$ patches of the sky at the ecliptic poles. This deeper survey is not only required for calibration purposes (see Chapter 4), but will also provide additional information for some of the secondary science cases, such as Type Ia Supernova searches.

## 1.2 The Euclid Mission

### 1.2.1 The Cosmic Vision Program

The European Space Agency (ESA) launched the Cosmic Vision Program in 2004 to develop the next generation of Europe's space based scientific missions. The program will deliver multiple cutting edge satellites to be launched in the 2017 - 2020 time frame. ESA suggested a broad spectrum of scientific themes for the program: ranging from the origin and composition of the Universe to the Solar System and the emergence of planets and life. Over 150 mission proposals were submitted by the European scientific community, and after two rounds of down-selections only three remain: Solar Orbiter [5], Plato [6] and Euclid [2], the three of which are competing for only two launch opportunities.

### 1.2.2 The Beginnings of the Euclid Mission

The Euclid Dark Energy Mission is the amalgamation of two of the original 150 mission proposals: the **D**ark **UN**iverse **E**xplorer (DUNE) [7] and the **SP**ectral **A**ll Sky **C**osmic **E**xplorer (SPACE) [8]. The two concepts had similar science goals, namely to probe the dark Universe, but utilized different science probes: DUNE Weak Lensing and SPACE Galaxy Clustering. ESA decided that a combined mission was superior to both of the original proposals and as a result the Euclid Mission was born, with imaging channels inherited from DUNE and a spectroscopic channel from SPACE.

### 1.2.3 Implementation Overview and Programmatic Changes

The conceptual design of the Euclid Mission has remained relatively constant since this time. The satellite, which will operate at the second Lagrange point, will consist of a 1.2 m telescope and a payload of three channels: a visible imaging channel, a near-infrared photometric channel and a near-infrared spectroscopic channel. During the last three years, the mission has undergone an Assessment Study (September 2008 - November 2009) [1] and a Definition Study (July 2010 - July 2011) [2]. In these two phases the distribution of these channels was different. In the Assessment Phase the **Vis**ible Imaging Channel (VIS) and the **N**ear-**I**nfrared **P**hotometric Channel (called NIP at this time) were combined into an imaging instrument, with the **N**ear-**I**nfrared **S**pectroscopic channel (NIS) as a standalone instrument separated after the telescope's secondary mirror. After this phase, the mission was de-scoped – particularly relating to the number of near-infrared detectors – and as such the two near-infrared channels were combined into a single instrument: the **N**ear-**I**nfrared **S**pectrometer and **P**hotometer (NISP), with the spectroscopic and photometric channels abbreviated to NISP-S and NISP-P respectively. In this implementation the visible channel is considered as a separate instrument, again called VIS.

### 1.2.4 The Current Baseline Mission Implementation

The Euclid Mission will survey over $15,000\ \mathrm{deg}^2$ of the extragalactic sky with a broadband visible imager, a near-infrared multi-band photometer and a near-infrared slitless spectrometer. The mission's baseline optical design is shown in Figure 1.1(left), with the main components identified. At the heart of the Euclid Mission is a 1.2 m Korsch telescope. All channels will observe the same off-axis $\sim 0.55\ \mathrm{deg}^2$ patch of sky. A dichroic element is positioned at the exit pupil of the telescope and it is at this point that the visible and near-infrared channels are separated: visible light is reflected back into the visible instrument and near-infrared light is transmitted into the near-infrared instrument. As a result, simultaneous observations can be performed in both the visible and near-infrared wavelength regimes. The Visible Imager

(VIS) does not contain any optical elements, as the telescope itself is optimized for the imaging performance of this instrument. The instrument has a large focal plane consisting of 36 ($6 \times 6$) CCDs. It also incorporates a shutter mechanism, which is required to block external sources during the readout of the CCDs, and a flat-field calibration source. The visible imager will provide diffraction limited imaging in the wavelength range $550-900$ nm over a 0.55 deg$^2$ field-of-view, with a pixel scale of 0.1 arcsec. The visible dataset will reach an extended source depth of 24.5 mag$_{AB}$ ($10\sigma$). The NISP Instrument is more complex and, since this thesis concentrates on aspects of its development, it is described in detail in the next section.

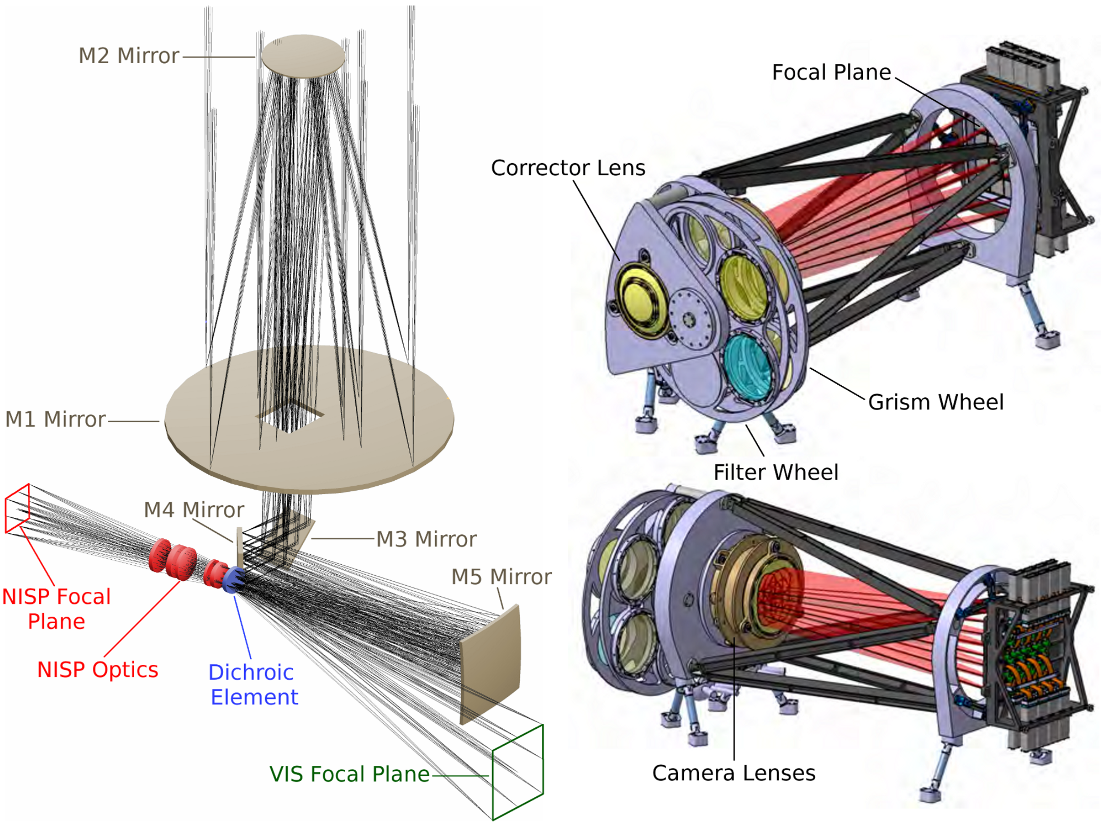


Figure 1.1: Left: The baseline optical design of the Euclid space telescope with the main components identified. The telescope's mirrors, M1→M5, are shown in beige. The two instruments – the Visible Imager (VIS) and the Near-Infrared Spectrometer and Photometer (NISP) – share a common optical path up to a dichroic element (blue), which reflects visible light back into the VIS Instrument (green) and transmits near-infrared light into the NISP Instrument (red). The VIS Instrument does not contain any optical elements, only a focal plane, as the telescope is optimized for the visible imaging quality. The off-axis nature of the telescope can be seen from the off-center hole in the primary mirror. Optical design provided by F. Grupp (Max-Planck-Institut für extraterrestrische Physik – Germany). Right: Two views of the baseline mechanical implementation of the NISP Instrument with the main subcomponents identified. Pictures, without annotations, provided by T. Pamplona (Centre de Physique des Particules de Marseille – France).

### 1.2.5 The Near-Infrared Spectrometer and Photometer (NISP)

As introduced in the Section 1.2.3, the NISP Instrument has two channels: a near-infrared photometer (NISP-P) and a near-infrared slitless spectrometer (NISP-S). The baseline implementation of the NISP Instrument can be seen in Figure 1.1(right). The two channels have common optics, focal plane, electronics and support structure. Two wheel mechanisms are used to switch between the different channels: (1) a filter wheel mechanism contains the three near-infrared photometry filters, a cold shutter and an open position and (2) a grism wheel with four grisms and an open position. To operate in the photometric mode, the grism wheel is rotated to the open position and the filter wheel is rotated to the required filter; to operate in spectroscopic mode the filter wheel is rotated to the open position and the grism wheel to a grism position. The optics consist of a corrector lens at the start of the instrument and a three lens camera after the grism/filter position that focuses light onto the focal plane. The large focal plane is made up from a mosaic of $4 \times 4$ of Teledyne's Hawaii 2RG 2k $\times$ 2k near-infrared detectors [9].

The NISP Photometric Channel (NISP-P) will image the sky in three near-infrared bands: Y ($0.920 - 1.146$ μm), J ($1.146 - 1.372$ μm) and a long H ($1.372 - 2.000$ μm). The resulting dataset will have a point source detection limit ($5\sigma$) of 24 $\mathrm{mag_{AB}}$ (see Section 2.3.1) for over 90 % of the survey (see Section 2.6), a depth that would be very difficult to reach from the ground over such a large area of the sky. The channel has a large 0.55 $\mathrm{deg}^2$ field-of-view. With only 16 2k $\times$ 2k detectors, this results in a pixel scale of 0.3 arcsec and therefore the channel is undersampled. The channel is a photometer; not an imager.

The NISP Spectroscopic Channel (NISP-S) will perform slitless $R = 250$ spectroscopy in two bands: filter coatings on the grism elements allow selection between the $1.10 - 1.45$ μm and $1.45 - 2.00$ μm wavelength ranges. The channel is a slitless spectrometer, so confusion between the spectra from different sources is a critical issue. To help distinguish between different sources, the channel includes two identical grism elements for each band. These are mounted with a 90 deg rotation between their lines, so that the spectrometer's dispersion direction can be changed to help distinguish overlapping spectra. The channel will be sensitive enough to detect ($3.5\sigma$) a $3 \times 10^{-16}\,\mathrm{erg\,cm^{-2}\,s^{-1}}$ line flux.

### 1.2.6 Observing Strategy

Euclid is a survey mission and not an observatory. The $15{,}000$ $\mathrm{deg}^2$ Euclid Wide Survey will be regularly tiled into patches of sky, each of which will be observed in turn with a common observing mode. Each patch of sky will be measured with four slightly offset exposures. This "dithering" has two purposes: (1) to provide a better sampling of the imaging channels' point-spread-functions and (2) to fill the gaps between active detector areas on the focal planes (see Section 2.6). The Euclid satellite will operate in a "step and stare" mode from the second Lagrange point; it will slew to the target coordinates, expose and then slew to the next.

Each dithered observation will be performed in a standard way. First the Visible Imaging

Channel and the NISP Spectroscopic Channel will observe in parallel, followed by a period in which only the NISP Photometric Channel will observe. The motion of the wheel mechanisms in the NISP Instrument, required to switch between different channels and different photometry filters, will introduce enough torque into the satellite to cause its pointing to drift sufficiently to contaminate the visible galaxy shape measurements. The Visible Imaging Channel cannot therefore be operated during the photometry exposures. The three Euclid channels will generate a large amount of scientific data: roughly 850 Gbits will be downloaded to ground every day.

The mission will also perform a deep survey. This “Deep Survey” will be 2 $\mathrm{mag_{AB}}$ deeper than the Wide Survey (see Section 2.4), and will be used for calibration and secondary science purposes. In Chapter 4, I discuss ways in which this observing strategy was optimized for calibration of the photometric channel.

### 1.2.7 Future Developments

The three missions competing in the Cosmic Vision Program: Euclid, Plato and Solar Orbiter, will be down-selected for two launch slots by the end of this year (2011). If successful in this final selection process, the Euclid Mission will be launched towards the end of this decade.

## 1.3 Thesis Scope

I have worked exclusively on Euclid, and in particular the near-infrared photometric channel, over the course of my thesis. My duties have changed over this time as the project, and the Max-Planck-Institut für Astronomie’s involvement, has evolved with the different study phases. During the Euclid Assessment Phase (September 2008 – November 2009), I focused on the development of hardware for the mission. In particular, I had a leading role in the design and the development of the flat-field calibration source (Chapter 5) and a filter wheel mechanism (Chapter 6). After this study phase the Euclid Consortium was reorganized as the two near-infrared channels were merged into one instrument. As a result, the filter wheel mechanism was no longer under the responsibility of the Max-Planck-Institut für Astronomie and therefore this work was stopped prematurely. During the Euclid Development Study (July 2010 – July 2011), I held the position of Photometry Instrument Scientist, one of three Instrument Scientists within the Euclid Consortium. With this senior scientific position, I was not only a member of the NISP Instrument team, but I also sat on the high level Euclid Coordination Board. With this role, I was responsible for the photometric performance of the NISP Instrument, and the work I conducted on this is presented in Chapter 2. As the Photometry Instrument Scientist, I was also responsible for the photometric calibration of the NISP Instrument. Chapter 3 presents general calibration concerns, such as the calibration budgets and the calibration strategy, with Chapter 4 presenting a detailed study into how the survey strategy can be optimized for the retrospective calibration of the dataset.

## 1.4 Collaborations

Euclid is a collaborative effort; at the last count the Euclid Consortium is made up of over 800 people. My work is therefore intertwined with that of others, particularly the work conducted under my duties as NISP Instrument Scientist. In this section I hope to summarize my collaborations with others. Throughout this thesis I reference the appropriate people in the footnotes.

As NISP Photometry Instrument Scientist, I have collaborated very closely with the NISP Spectroscopic Instrument Scientist A. Ealet[2], my counterpart for the near-infrared spectroscopic channel. We have worked closely on defining the instrument's performance parameters, performance validations and the instrument's calibration strategy. As also an active member of the NISP Detector working group, Ealet has provided much of the information relating to detector performances, in addition to contributions from F. Bortoletto[3] and C. Bonoli[4]. Other members of the NISP Instrument team have contributed data. Of particular importance are the optical designs provided by F. Grupp[5], which have been used for the performance evaluations in Chapter 2.

On a higher system level, J. Amiaux[6] has provided satellite wide data, such as – but not limited to – the telescope's throughput, stability estimates and the central obscuration size, all of which have been included in the performance evaluations presented in Chapter 2. Amiaux and R. Scaramella[7] have studied the missions observing strategy and their proposed implementation of the Euclid Deep Field survey strategy is analyzed in Chapter 4. This work, on the retrospective calibration of the photometry dataset, has been performed in a close collaboration with D. Hogg[8].

During my time as NISP Photometry Instrument Scientist, I have collaborated closely with G. Seidel[9]; his work on developing an image simulator for the photometric channel has not only allowed performances to be tested in detail, but has allowed us to gain a deep understanding of many of the subtle instrument effects.

[2] A. Ealet (Centre de Physique des Particules de Marseille – France)
[3] F. Bortoletto (Istituto Nazionale di Astrofisica – Italy)
[4] C. Bonoli (Istituto Nazionale di Astrofisica – Italy)
[5] NISP Optical Lead: F. Grupp (Max-Planck-Institut für extraterrestrische Physik – Germany)
[6] J. Amiaux (Commissariat à l'Energie Atomique et aux Energies Alternatives – France)
[7] R. Scaramella (Istituto Nazionale di Astrofisica – Italy)
[8] D. W. Hogg (New York University – USA)
[9] G. Seidel (Max-Planck-Institut für Astronomie – Germany)

# Chapter 2

# Towards Euclid Implementation[1]

**Chapter Abstract:** This chapter presents the work I completed as the NISP Photometry Scientist, a senior scientific position within the Euclid Consortium that is responsible for the performance of the NISP Photometric Channel. This broad responsibility required a large number of diverse tasks, calculations and estimations; the common theme is that they all deal with the photometric performance of the instrument. In some cases, this work has been used in the day-to-day development of the NISP Instrument, and in others, it has formed part of the official performance verification process required by the European Space Agency's Cosmic Vision Program.

## 2.1 Introduction

In this chapter, I detail the work I conducted during my time as the NISP Photometry Scientist, one of the senior members of the NISP Instrument Team. My responsibility started at the higher level science requirements [12], which were derived by the Euclid Science Teams, and was to ensure that the instrument was capable of satisfying them. In practice, the tasks fell into two categories: (i) flowing down the science requirements into instrument requirements and (ii) verifying the performance of the proposed instrument against these higher level requirements. This chapter details the calculations and simulations used to perform these two duties. Many of them have been targeted at specific issues and therefore this chapter is rather multifaceted, with the performance of the NISP Photometric Channel as the common theme. Much of this work has been intertwined with that of others, where appropriate I reference the relevant people in the footnotes.

After detailing the construction of the reference optical performance parameters for the current instrument design in Section 2.2, this chapter turns to address a number of key questions about the NISP Photometric Channel:

[1] Aspects of this work have been included in the *NISP Performance Analysis Report* [10] and the *NISP Requirement Flow Down Report* [11].

- Section 2.3.1: What is the radiometric performance of the channel, and what exposure times are needed to meet the detection limit requirements?
- Section 2.3.2: Subsequently, what should the baseline observing mode of the channel be?
- Section 2.3.3: How can the higher level science requirements be flown-down to instrument level requirements?
- Section 2.3.4: How can the detector performance requirements be expressed in a way that allows the vendor some flexibility, but still ensures that the science requirements can be met?
- Section 2.3.5: How sensitive is the channel's radiometric performance to satellite instability?
- Subsection 2.4: How many revisits to the Euclid Deep Field are required to reach the deeper detection limit?
- Subsection 2.5: What is the channel's saturation limit?
- Subsection 2.6: How do the gaps in the focal plane detector mosaic impact on the sky coverage?
- Subsection 2.7: What is the channel's coverage of the Euclid Wide Survey?

## 2.2 Constructing the Reference Performance Parameters

### 2.2.1 Reference Point-Spread-Functions

The optical quality of the NISP Photometric Channel is constrained by two high level science requirements. The first ([12], WL.2.1-19) relates to crowding concerns: to reduce source blending the channel's point-spread-function (PSF) is required to be relatively compact. The second, more indirect constraint comes from the channel's detection limit requirement ([12], WS.2.2-3). Here, a wider PSF will result in a lower detection limit, as a source's flux will be spread over more pixels and therefore noise will be more significant (see Section 2.3). There are no requirements on the NISP Photometric Channel coming from pure imaging; the channel is a photometer and not an imager.

In this section, the construction of the channel's reference PSFs is detailed. These have been subsequently distributed to the wider Euclid Consortium. The reference *system* PSF for each photometric band is generated from three components: (i) an optical design with realistic manufacturing errors[2], (ii) a spacecraft jitter model[3] and (iii) a detector model[4].

[2] F. Grupp (Max-Planck-Institut für extraterrestrische Physik – Germany)
[3] J. Amiaux (Commissariat à l'Energie Atomique et aux Energies Alternatives – France)
[4] A. Ealet (Centre de Physique des Particules de Marseille – France)

The performance of a perfect optical system, one free from manufacturing and alignment errors, is normally superior to a physically realizable implementation of it. To estimate realistic performances, Monte Carlo simulations are performed in which errors – within realistic ranges – are introduced into the system. When a sufficiently large number of Monte Carlo samples have been created, it is possible to assess the performance of the optical system statistically. A near-worst case Monte Carlo implementation of the channel has been selected as the reference optical design[5]. There is therefore a high probability that the manufactured system will perform better than the reference presented here. From this reference design, I have used the *ZEMAX* optical design software to produce polychromatic optical PSFs in each of the three photometry bands, with a $1\,\mu$m resolution, at positions on a $3 \times 3$ grid across the channel's focal plane. These PSFs are degraded with a telescope instability model and a detector model to produce *system* PSFs. The satellite's fine guidance system will not be perfect and the instabilities in the telescope's pointing ("jitters") will lead to a blurring of the optical PSF. This degradation is modeled as convolution of the optical PSFs with a Gaussian function that has a full-width-at-half-maximum (FWHM) of 0.05 arcsec[6]. The final degradation of the channel's PSF comes from the detector, where effects such as inter-pixel capacitance and charge diffusion will distribute some of the signal into neighboring pixels. For the baseline Hawaii -2RG near-infrared detectors [9], this degradation is modeled as a convolution with a Gaussian function that has a FWHM of 0.06 arcsec. For each photometry band, *system* PSFs are generated from these three contributors on the $3 \times 3$ grid across the focal plane[7].

The optical performance of the channel is assessed by calculating the simulated *system* PSFs' encircled energies' 50 and 80 values (EE50 and EE80 respectively). These are defined as the radii at which 0.5 and 0.8 of the total energy is enclosed (compact PSFs have lower values). These values are presented in Table 2.1 for the simulated system PSFs. The encircled energy values are used to identify the focal plane position with the widest PSF, and therefore the worst optical performance. The PSFs from these worst performing focal plane positions in each band are defined to be the references for the channel. The three simulated reference PSFs are shown in Figure 2.1 (top). As can be seen in Table 2.1, the NISP Photometric Channel easily meets the optical quality requirement (originating from crowding concerns) at all focal plane positions tested. The corresponding en*squared* energies for these simulated reference PSFs are also shown in Figure 2.1 (below). The en*squared* energy is a quantity similar to the en*circled* energy, but one that represents the fraction of light falling within a square aperture as opposed to a circular aperture. The fractions of light from a point source falling within centered $1 \times 1$, $2 \times 2$ and $3 \times 3$ pixel apertures are also identified (pixel size = 18 $\mu$m) This information is used

[5]Zemax File: 06_032_001MC_T0055.ZMX – F. Grupp (Max-Planck-Institut für extraterrestrische Physik – Germany)

[6]I have confirmed that this model is consistent with the results of the satellite stability simulations provided by the European Space Agency in support of the Euclid Definition Study, but since this data is proprietary and unpublished, I am unable to present this work here.

[7]The NISP Photometry Simulator (G. Seidel – Max-Planck-Institut für Astronomie, Germany) was used to perform these convolutions.

in the radiometric performance evaluation presented in Section 2.3.

| **Field Point** | **Y** | | **J** | | **H** | |
|---|---|---|---|---|---|---|
| | **EE50 (")** | **EE80 (")** | **EE50 (")** | **EE80 (")** | **EE50 (")** | **EE80 (")** |
| **1** | 0.18 | 0.45 | 0.18 | 0.48 | 0.23 | 0.59 |
| **2** | 0.18 | 0.46 | 0.18 | 0.47 | 0.22 | 0.58 |
| **3** | 0.18 | 0.44 | 0.18 | 0.45 | 0.22 | 0.58 |
| **4** | 0.21 | 0.48 | *0.21* | *0.50* | *0.25* | *0.61* |
| **5** | 0.20 | 0.48 | 0.20 | 0.49 | 0.23 | 0.60 |
| **6** | 0.19 | 0.47 | 0.18 | 0.47 | 0.23 | 0.58 |
| **7** | 0.18 | 0.47 | 0.18 | 0.47 | 0.24 | 0.60 |
| **8** | 0.18 | 0.47 | 0.18 | 0.48 | 0.22 | 0.59 |
| **9** | *0.23* | *0.49* | 0.19 | 0.48 | 0.24 | 0.61 |
| **Requirement** | $< 0.30$ | $< 0.62$ | $< 0.30$ | $< 0.63$ | $< 0.33$ | $< 0.70$ |

Table 2.1: The encircled energies 50 and 80 (EE50 and EE80 respectively) of the NISP Photometric Channel's simulated *system* PSFs. The worst performing focal plane positions in each band are highlighted in red. The optical quality requirement originating from crowding concerns ([12], WL.2.1-19) is also presented.

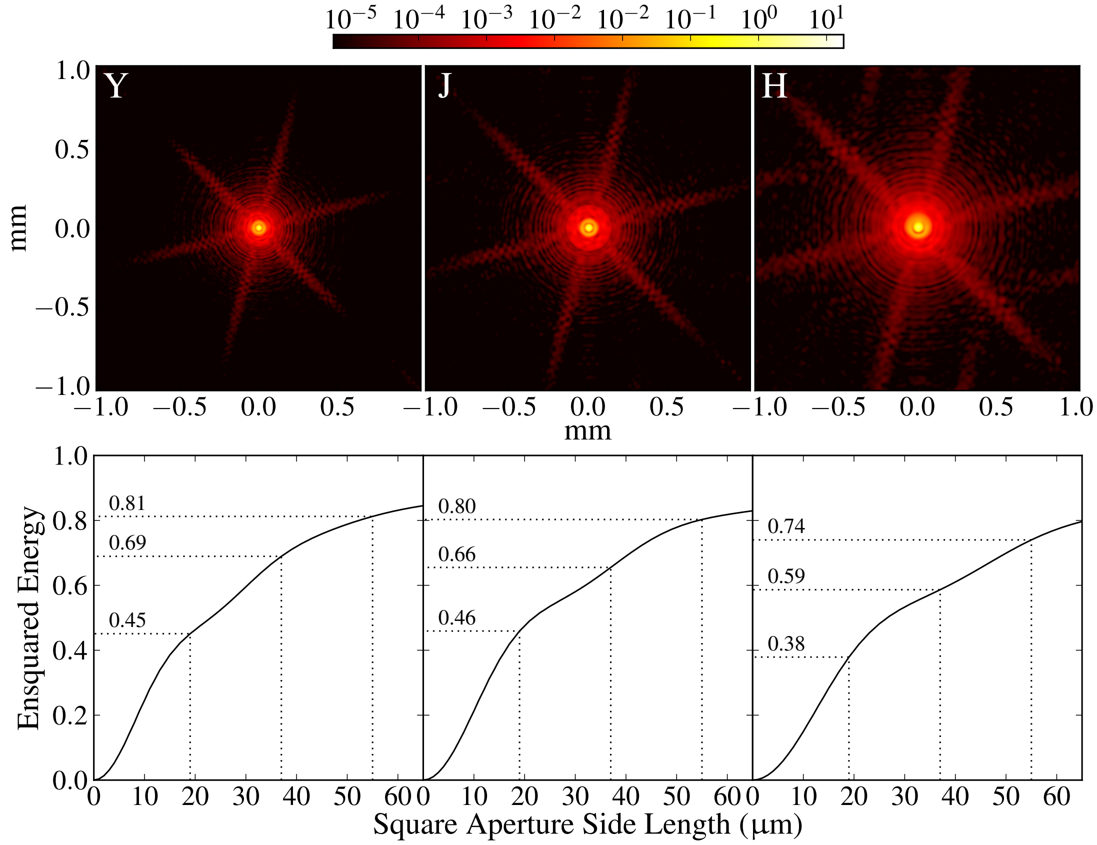


Figure 2.1: Top: The polychromatic reference point-spread-function models for the NISP Photometry Channel in the Y-band: $0.920 - 1.146$ μm (left), J-band: $1.146 - 1.372$ μm (middle) and H-band: $1.372 - 2.000$ μm (right). Low level computational artifacts, coming from the optical PSF simulations, can be seen in the H-band PSF. Bottom: The corresponding en*squared* energies, with the fractions of light falling within a centered $1 \times 1$, $2 \times 2$ and $3 \times 3$ pixel area identified with the dotted lines (pixel size = 18 μm).

### 2.2.2 Reference Photon-to-Electron Conversion Efficiency

Another important performance parameter for the NISP Photometric Channel is its photon-to-electron conversion efficiency. This quantity is simply the ratio of the signal recorded in the detectors to the photon flux entering the telescope. It includes contributions from the telescope's central obscuration, the telescope's throughput, the instrument's throughput and the detector's quantum efficiency. This is particularly important for the radiometric performance evaluations presented in Section 2.3 and the photometric redshift ("photo-z") simulations conducted by the Euclid Science Teams.

The reference photon-to-electron conversion efficiency has been generated from: (i) the telescope optical throughput (including the dichroic element)[8], (ii) the instrument optical through-

[8]The European Space Agency

put[9], (iii) realistic filter transmission profiles[10] and assuming (iv) a central telescope obscuration of 11 %[11] and (v) a detector quantum efficiency of 0.7 [13]. The resulting reference curves are shown in Figure 2.2. The low efficiency at the short wavelength end of the Y-band is a result of the low transmission of the dichroic element at these wavelengths. This element must reflect light into the visible instrument up to 900 nm; a sharp wavelength transition from reflecting to transmitting is not possible. The kinks in the profile are due to the low resolution of the dichroic data. The reduction in efficiency towards long wavelengths in the H-band is due to one of the NISP Instrument's lens materials: S-FTM16. It is hoped that this material can be replaced in the future, but no other suitable radiation hard glasses have been qualified for space applications yet.

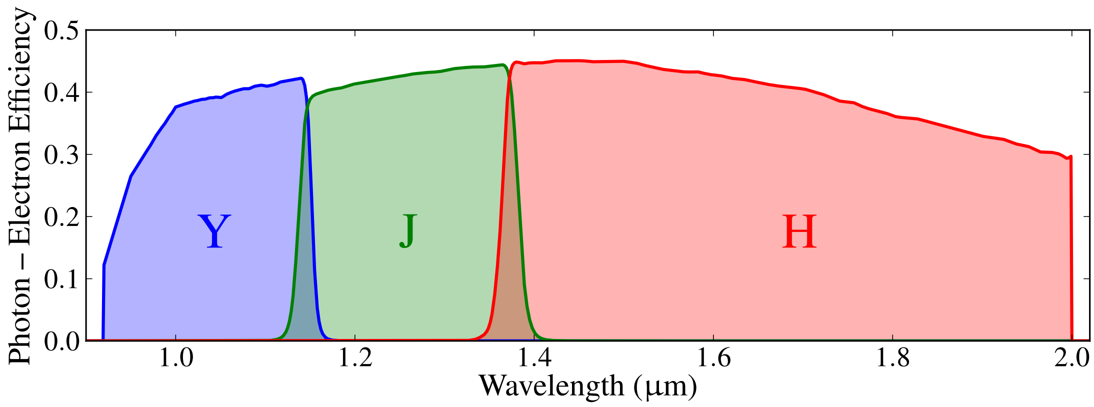


Figure 2.2: The reference photon-to-electron conversion efficiency for the three photometric bands of the NISP Instrument. These curves include contributions from the telescope's throughput, the instrument's throughput, the detector's quantum efficiency and the telescope's central obscuration.

## 2.3 Radiometric Performance

The primary purpose of the NISP Photometric Channel is to supplement the visible galaxy shape measurements with multi-band, near-infrared photometry. When combined with ground-based visible photometry, these measurements will be used to estimate the photometric redshifts of the galaxies within the survey. The requirement on the statistical error of the photometric redshifts ([12], WL.1-5) is propagated, by the Euclid Weak Lensing Working Group[12], into a ($5\sigma$) point source detection limit requirement for the NISP Photometric Channel of $Y_{AB}$, $J_{AB}$, $H_{AB}$ = 24

[9] F. Grupp (Max-Planck-Institut für extraterrestrische Physik – Germany) and E. Prieto (Centre de Physique des Particules de Marseille – France)

[10] Materion Barr Precision Optics, USA

[11] J. Amiaux (Commissariat à l'Energie Atomique et aux Energies Alternatives – France)

[12] Coordinators: H. Hoekstra (Leiden Observatory – The Netherlands) and T. Kitching (University of Edinburgh – United Kingdom)

mag ([12], WS.2.2-3). In the following subsections, various issues associated with meeting this requirement are considered.

### 2.3.1 Scientific Exposure Times

Euclid is a survey mission; the survey area will be tiled and observed in a regular manner. In each photometry band the patches of sky will be imaged with four dithered exposures. Originally, a time of 100 s had been allocated to each of these dither exposures, which must include house-keeping activities such as filter wheel motions. In this subsection, I detail the radiometric performance calculation I performed to refine the reference exposure times by considering the point source detection limit requirement. This depth requirement applies to the final photometric catalog, which will be formed by combining the multiple dithered images. Gaps in the active focal plane area, due to the imperfect mosaicking of the $4 \times 4$ infrared detectors, will introduce depth variations in the resulting catalog. The four pointing dither strategy is designed to limit the impact of these gaps. When calculating the exposure times needed to meet the detections limit requirement, I assume that the point source is measured in three or more of the four dithered exposures, corresponding to $\sim 92\%$ of the survey (see Section 2.6).

The required exposure times are identified with an analytical signal-to-noise calculation. This radiometric calculation is based on aperture photometry of a point source falling at the center of a $2 \times 2$ pixel aperture. Subsequent full image simulations and PSF fitting photometry[13] gives results consistent with this analytical calculation. The reference PSFs and photon-to-electron conversion efficiencies introduced in Subsections 2.2.1 and 2.2.2 respectively are used to calculate the signal from a point source falling within this aperture. Noise contributions from the source, the sky background, the scattered light contamination, the detector dark currents and the detector readout are all considered.

A common sky background model for all of the mission's science channels is defined in [14]. The average sky background surface brightness across the survey is used in this calculation, which is defined as $Y_{AB} = 22.09$, $J_{AB} = 22.07$ and $H_{AB} = 22.20$ mag arcsec$^{-2}$ in the photometric bands. In addition to the sky background, there will also be a diffuse background signal coming from scattered light and thermal emission within the satellite, the noise from which must also be accounted for. The permissible magnitude of this contamination is defined in terms of the signal that would be measured from the sky background at the ecliptic poles: the contamination is required ([12], WL 2.1-12) to be below 20% of this. The sky surface brightness at the ecliptic poles is also defined in [14], as $Y_{AB} = 22.69$, $J_{AB} = 22.67$ and $H_{AB} = 22.80$ mag arcsec$^{-2}$.

In a single dithered exposure, indexed $i$, the different noise contributions are assumed to be uncorrelated and they are therefore added in quadrature. The total noise contribution in a single

[13] G. Seidel (Max-Planck-Institut für Astronomie – Germany)

dither exposure $\sigma_i$ is

$$\sigma_i = \sqrt{\sigma^2_{i,\mathrm{src}} + \sigma^2_{i,\mathrm{sky}} + \sigma^2_{i,\mathrm{sct}} + \sigma^2_{i,\mathrm{DC}} + \sigma^2_{i,\mathrm{RN}}} \quad , \tag{2.1}$$

where the individual noise contributors are from the source signal $\sigma_{i,\mathrm{src}}$, the sky background signal $\sigma_{i,\mathrm{sky}}$, the scattered light contamination $\sigma_{i,\mathrm{sct}}$, the detector dark currents $\sigma_{i,\mathrm{DC}}$ and the detector readout noise $\sigma_{i,\mathrm{RN}}$. The form and fiducial values of these noise contributions are summarized in Table 2.2. To produce the final measurement, the signals and noise contributions from $d = 3$ single dither exposures are combined. The final measurement signal $S_{\mathrm{tot}}$ is found by combining the individual dither signals $S_i$ linearly:

$$\begin{aligned} S_{\mathrm{tot}} &= \sum_{i=1}^{d} S_i \\ &= R\alpha \sum_{i=1}^{d} t_i \quad , \end{aligned}$$

where $R$ is the electron flux in the detectors from the source, $\alpha$ is the fraction of light from the source falling within the pixel aperture and $t_i$ are the individual dither exposure times. Since all the individual dithers will have the same exposure time $t$, this can be rewritten as

$$S_{\mathrm{tot}} = R\alpha t d \quad . \tag{2.2}$$

To estimate the noise $\sigma_{\mathrm{tot}}$ on the final combined dither measurement, the total noise from the individual dithers $\sigma_i$ are summed in quadrature:

$$\sigma_{\mathrm{tot}} = \sqrt{\sum_{i=1}^{d} \sigma_i^2} \quad . \tag{2.3}$$

A detection level $\phi$ would then require a total source signal such that $S_{\mathrm{tot}} = \phi\,\sigma_{\mathrm{tot}}$ (for example a $5\sigma$ detection limit would require $S_{\mathrm{tot}} = 5\,\sigma_{\mathrm{tot}}$). From Equations 2.1, 2.2 and 2.3 and the form of the single dither noise contributions given in Table 2.2, it is possible to write the detection level explicitly as

$$\phi = \frac{S}{\sigma_{\mathrm{tot}}} \tag{2.4}$$

$$= \frac{R\alpha t d}{\sqrt{\left[R\alpha + n\Omega^2\left(R_{\mathrm{sky}} + \gamma R_{\mathrm{pole}}\right) + nD\right] t d + d n \beta^2}} \quad . \tag{2.5}$$

This equation can then be rearranged to find the source signal $R$ that would be needed, as a function of a single dither exposure time $t$, to reach a given detection level $\phi$. The source signal can be translated into point source magnitudes using the photon-to-electron conversion efficiency in Figure 2.2 and the Euclid main mirror diameter of 1.2 m.

| Quantity | Notation | Formulation / Fiducial Value |
|---|---|---|
| **Single Dither Source Signal** | $S_i$ | $R\alpha t$ |
| **Single Dither Noise Contributions** | | |
| Source Noise | $\sigma_{i,\mathrm{src}}$ | $\sqrt{S}$ |
| Sky Background Noise | $\sigma_{i,\mathrm{sky}}$ | $\sqrt{\Omega^2 R_{\mathrm{sky}}\, n t}$ |
| Scattered Light Noise | $\sigma_{i,\mathrm{sct}}$ | $\sqrt{\gamma\Omega^2 R_{\mathrm{pole}}\, n t}$ |
| Dark Current Noise | $\sigma_{i,\mathrm{DC}}$ | $\sqrt{D n t}$ |
| Read Noise | $\sigma_{i,\mathrm{RN}}$ | $\sqrt{n\beta^2}$ |
| **Signals** | | |
| Source Signal (24 $\mathrm{mag_{AB}}$) | $R$ | Y: 1.243 $\mathrm{e^- \, sec^{-1}}$<br>J: 1.298 $\mathrm{e^- \, sec^{-1}}$<br>H: 2.386 $\mathrm{e^- \, sec^{-1}}$ |
| Sky Background Signal | $\Omega^2 R_{\mathrm{sky}}$ | Y: 0.650 $\mathrm{e^- \, sec^{-1}\, pix^{-1}}$<br>J: 0.691 $\mathrm{e^- \, sec^{-1}\, pix^{-1}}$<br>H: 1.127 $\mathrm{e^- \, sec^{-1}\, pix^{-1}}$ |
| Scattered Light Signal | $\gamma\Omega^2 R_{\mathrm{pole}}$ | Y: 0.075 $\mathrm{e^- \, sec^{-1}\, pix^{-1}}$<br>J: 0.080 $\mathrm{e^- \, sec^{-1}\, pix^{-1}}$<br>H: 0.130 $\mathrm{e^- \, sec^{-1}\, pix^{-1}}$ |
| **Detector Properties** | | |
| Quantum Efficiency* | $\eta$ | 0.7 |
| Dark Current | $D$ | 0.1 $\mathrm{e^- \, sec^{-1}\, pix^{-1}}$ |
| Readout Noise | $\beta$ | 7 $\mathrm{e^-}$ rms |
| Pixel Scale | $\Omega$ | 0.3 arcsec $\mathrm{pix^{-1}}$ |
| **Extraction Parameters** | | |
| Number of Pixels in Aperture | $n$ | $4\,(2\times 2)$ |
| Fraction of Source Flux within Aperture | $\alpha$ | Y: 0.677<br>J: 0.644<br>H: 0.579 |
| **General Parameters** | | |
| Scattered Light Requirement | $\gamma$ | 0.2 |
| Number of Dithers | $d$ | 3 |
| Single Dither Exposure Time | $t$ | - |

Table 2.2: The quantities used in the analytical radiometric performance calculations for the NISP Photometric Channel. The formulation of the source signal and the different noise contributors are detailed, with the corresponding parameters and their fiducial values listed below. The signals (electron fluxes in the detectors) are calculated with the photon-to-electron conversion efficiency shown in Figure 2.2 and assuming that Euclid will have a 1.2 m diameter main mirror. *The quantum efficiency is included already in the photon-to-electron conversion efficiency.

| Photometric Band | Required Exposure Time (sec) | |
|---|---|---|
| | Nominal | With Margin |
| Y | 78.2 | 88 |
| J | 80.6 | 90 |
| H | 47.7 | 54 |

Table 2.3: The *single dither* exposure times required to reach the 24 $\mathrm{mag_{AB}}$ point source detection limit with the current configuration of the NISP Photometric Channel. Performance margins are not taken at subcomponent level, instead they are applied at system level as an increase in exposure time.

This method is used to calculate the $5\sigma$ and $10\sigma$ point source detection limits presented in Figure 2.3 (top), which are shown for varying single dither exposure times $t$. The total noise $\sigma_i$ in a single dither exposure is also plotted as a function of exposure time (below), along with the two dominant noise contributions: the readout noise $\sigma_{i,\mathrm{RN}}$ and the sky background noise $\sigma_{i,\mathrm{sky}}$. For completeness, the other noise contributors are combined and also plotted as $\sigma_{i,\mathrm{oth}}$. The exposure times required, per dither, to reach a 24 $\mathrm{mag_{AB}}$ point source detection limit can be seen in Figure 2.3 and are summarized in Table 2.3. With the reference sky background brightnesses used in this calculation, the noise contribution from the sky background is slightly higher than the readout noise at the required exposure times. It should be noted that these sky background brightnesses correspond to the average across the Euclid Wide Survey; exposures of areas with a fainter sky background, such as the ecliptic poles, will be dominated by the read noise. This average sky background case calculation is sufficient for this stage of the mission and survey planning; ultimately the exposure times will have to be scaled with different sky backgrounds to allow for a uniform depth within the survey.

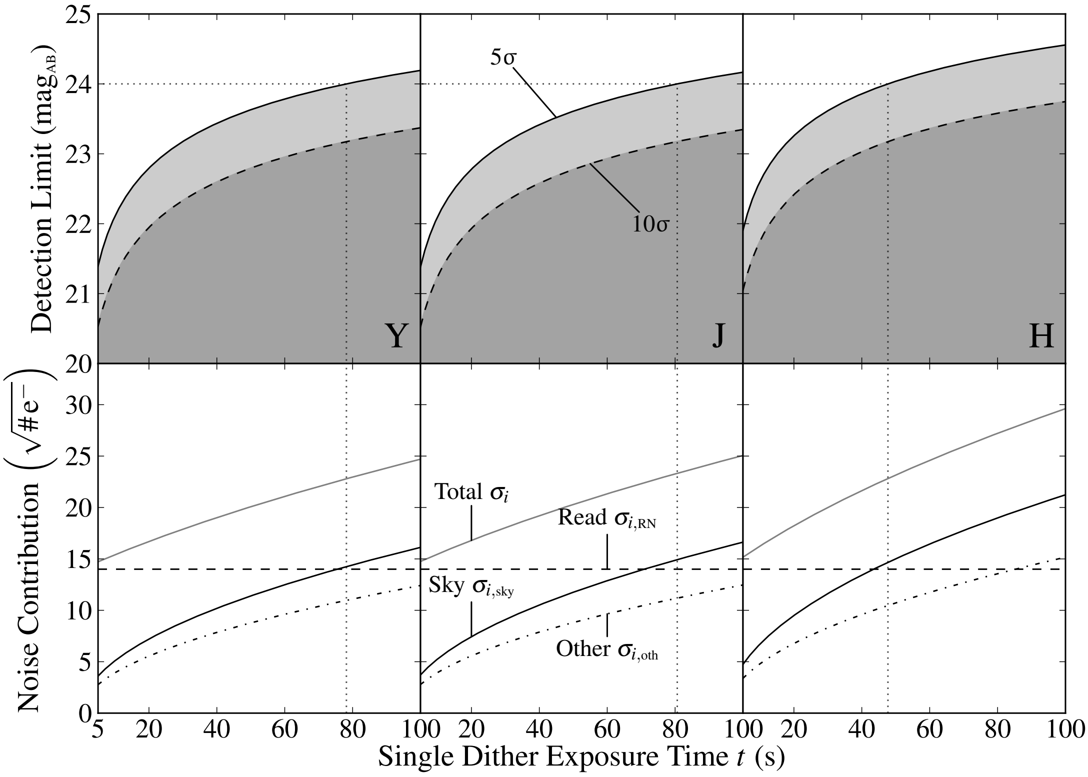


Figure 2.3: Top: The $5\sigma$ (solid line) and $10\sigma$ (dashed line) detection limits for the three photometry bands [Y: 0.920 – 1.146 μm (left), J: 1.146 – 1.372 μm (middle) and H: (1.372 – 2.000 μm (right)] as a function of single dither exposure time. The shaded regions correspond to point source magnitudes that will be detected above these limits. The exposure times required to reach the 24 mag$_{\mathrm{AB}}$ ($5\sigma$) detection limit are indicated with the vertical dotted guide line. Bottom: The corresponding single dither measurement noise contributions for the above plots: the total noise $\sigma_i$ (gray line), the read noise $\sigma_{i,\mathrm{RN}}$ (dashed line), the sky background noise $\sigma_{i,\mathrm{sky}}$ (solid line) and a combination of the remaining contributions $\sigma_{i,\mathrm{oth}}$ (dot-dash line).

The similarity between the required Y- and J-band exposure times can be attributed to: (i) the low transmission at the shorter wavelength edge of the Y band (due to the dichroic element) and (ii) the similarity between the PSF sizes in these bands, as the optics at these wavelengths are dominated by aberrations and not diffraction effects. The H-band exposure time is lower than the other two due to its wider band pass (see Figure 2.2) and the lower sky background at these wavelengths.

In accordance with the Euclid margin philosophy, performance margins are not taken at instrument subcomponent level. The margin is applied at a system level as an increase in the exposure time. The exposure times with the system margin applied are also shown in Table 2.3. This margin roughly corresponds to a reduction in the photon-to-electron conversion efficiency of 10% and a further blurring of the PSF, modeled as a convolution with a Gaussian function that has a FWHM = 0.17 arcsec.

### 2.3.2 Baseline Observing Mode

I have used the exposure times (with margin) calculated in Subsection 2.3.1 to define the NISP Photometry Channel's observing mode shown in Figure 2.4. I conclude that the current configuration of the channel is able to meet the point source detection limit requirement within 272 s, including house keeping activities. This is a $\sim 10$ % reduction compared to the originally alloted time. This reference observing mode has been used by the Euclid System Lead[14] and the Euclid Survey Scientist[15] to define the reference survey strategy for the mission. They conclude that a 15,000 deg$^2$ survey can be performed with a 6 year scientific mission [15].

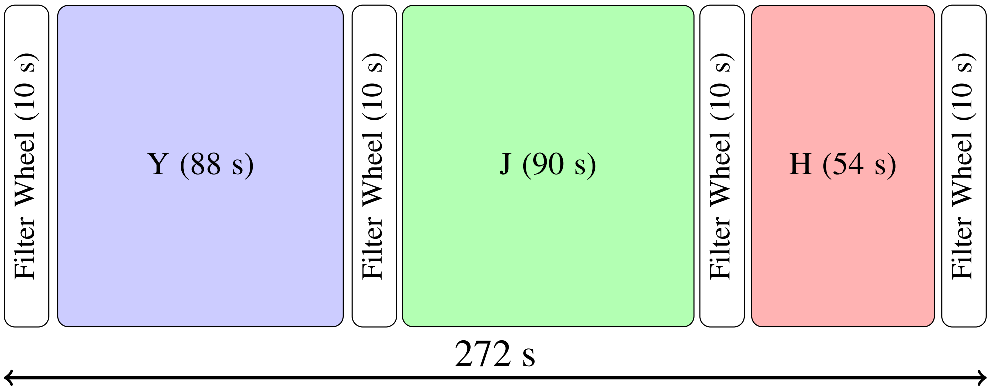


Figure 2.4: The NISP Photometric Channel's reference observing strategy. Four filter wheel operations are required per dither, as the observing sequence must start and finish with the open position required for the NISP Spectroscopic Channel's observations (Open Position $\rightarrow$ Y-Filter $\rightarrow$ J-Filter $\rightarrow$ H-Filter $\rightarrow$ Open Position). The 10 sec filter wheel rotation (and subsequent satellite settling) time is the baseline assumed by the Euclid Consortium, although this has not been verified.

### 2.3.3 Requirement Breakdown

An important activity for the development of the Euclid Mission is the flow-down of science requirements into instrument and telescope requirements. As NISP Photometry Scientist, the flow-down of the photometric science requirements was my responsibility. In this subsection, the flow-down of the NISP Photometric Channel's detection limit requirement ($Y_{AB}$, $J_{AB}$, $H_{AB}$ = 24 mag ($5\sigma$) – [12], WS.2.2-3) is detailed. This flow-down is based on the best available knowledge of instrument and telescope performances[16]. These performance parameters were used to fix the channel's scientific exposure times presented in Subsection 2.3.1. If the channel meets these performances, then it will be able to meet the detection limit requirement within

[14] J. Amiaux (Commissariat à l'Energie Atomique et aux Energies Alternatives – France)

[15] R. Scaramella (Istituto Nazionale di Astrofisica – Italy)

[16] data provided by A. Ealet (Centre de Physique des Particules de Marseille – France), E. Prieto (Centre de Physique des Particules de Marseille – France), F. Grupp (Max-Planck-Institut für extraterrestrische Physik – Germany), J. Amiaux (Commissariat à l'Energie Atomique et aux Energies Alternatives – France), F. Bortoletto (Istituto Nazionale di Astrofisica – Italy) and C. Bonoli (Istituto Nazionale di Astrofisica – Italy).

the defined exposure times. These assumed performance parameters are therefore subsequently applied as requirements on the mission's subcomponents.

The requirement flow-downs, which must be performed separately for each band, are presented schematically in Figures 2.5, 2.6 and 2.7 for the Y-, J- and H-bands respectively. In these diagrams, the higher level science requirement is shown in orange, the requirements that have been flow-down to instrument level are shown in blue and the assumptions made during the flow-down are shown in white. It would not, for example, be appropriate to define a requirement on the sky background as this is beyond the responsibility of the instrument team! In these flow-downs, the detector dark current noise and the readout noise are combined into a slightly more conservative total detector noise requirement. The requirement breakdown presented here has been included in *NISP Requirement Flow Down Report* [11], which provides the basis for the instrument subcomponent requirements.

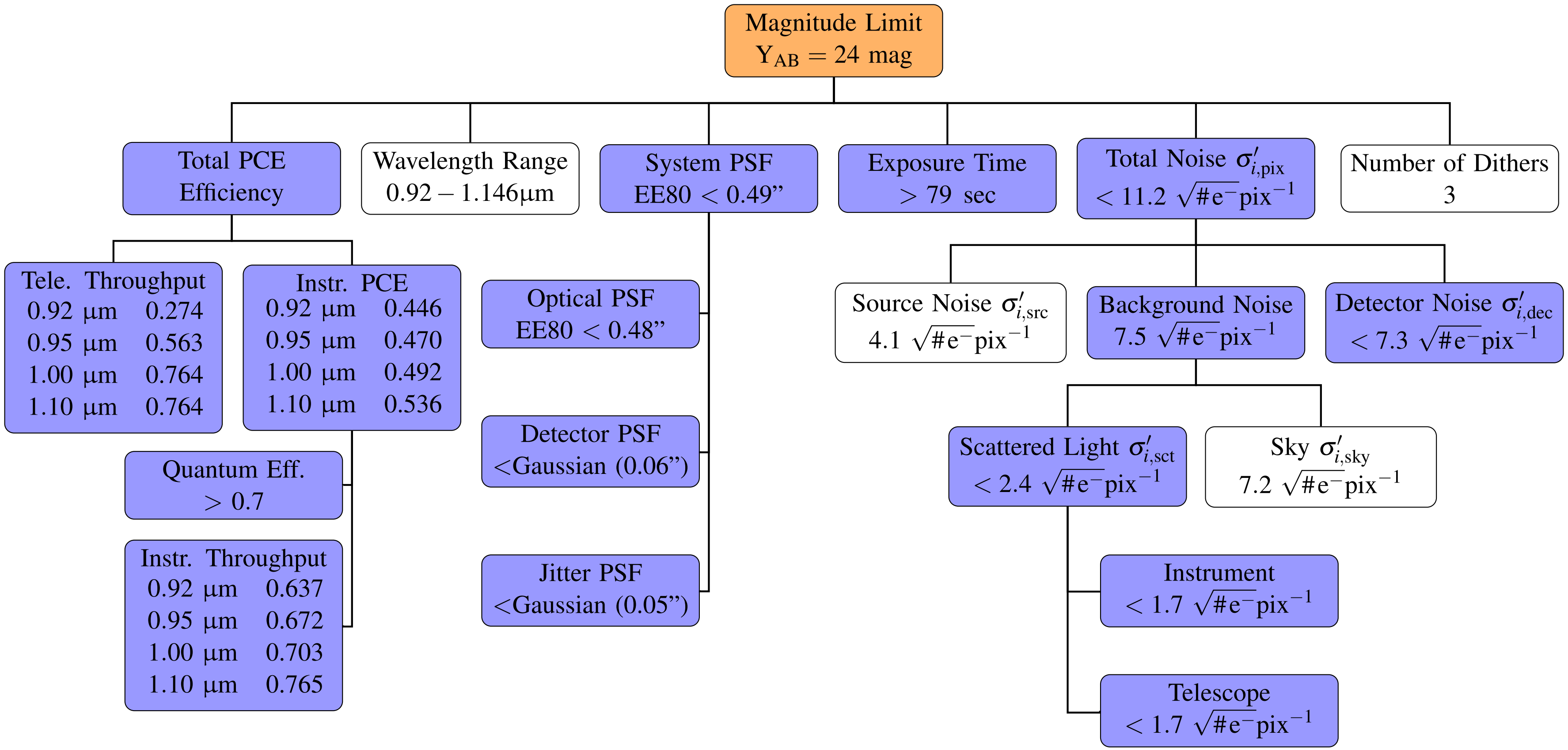


Figure 2.5: The flow-down of Y-band detection limit requirement ([12] WS.2.2-3) into instrument and telescope requirements. This flow-down is based on the unmargined exposure time calculation presented in Section 2.3.1. The blue boxes show the requirements applied to the instrument and telescope and the white boxes detail the assumptions made during this flow-down. In this flow-down the single dither $i$ noise contributions $\sigma'_{i,j}$ are defined per pixel (dash added to notation), not for the total aperture as in Table 2.2. The scattered light budget has been split equally between the telescope and the instrument by the European Space Agency; here I make the same split for the scattered light noise contributions. Notation: PCE = photon-to-electron conversion efficiency, Tele. = Telescope, Instr. = Instrument, Eff. = Efficiency, < Gaussian (nn”) = the resulting PSF must be enclosed within a Gaussian function with a FWHM = nn arcsec, $\#e^{-}$ = Number of electrons.

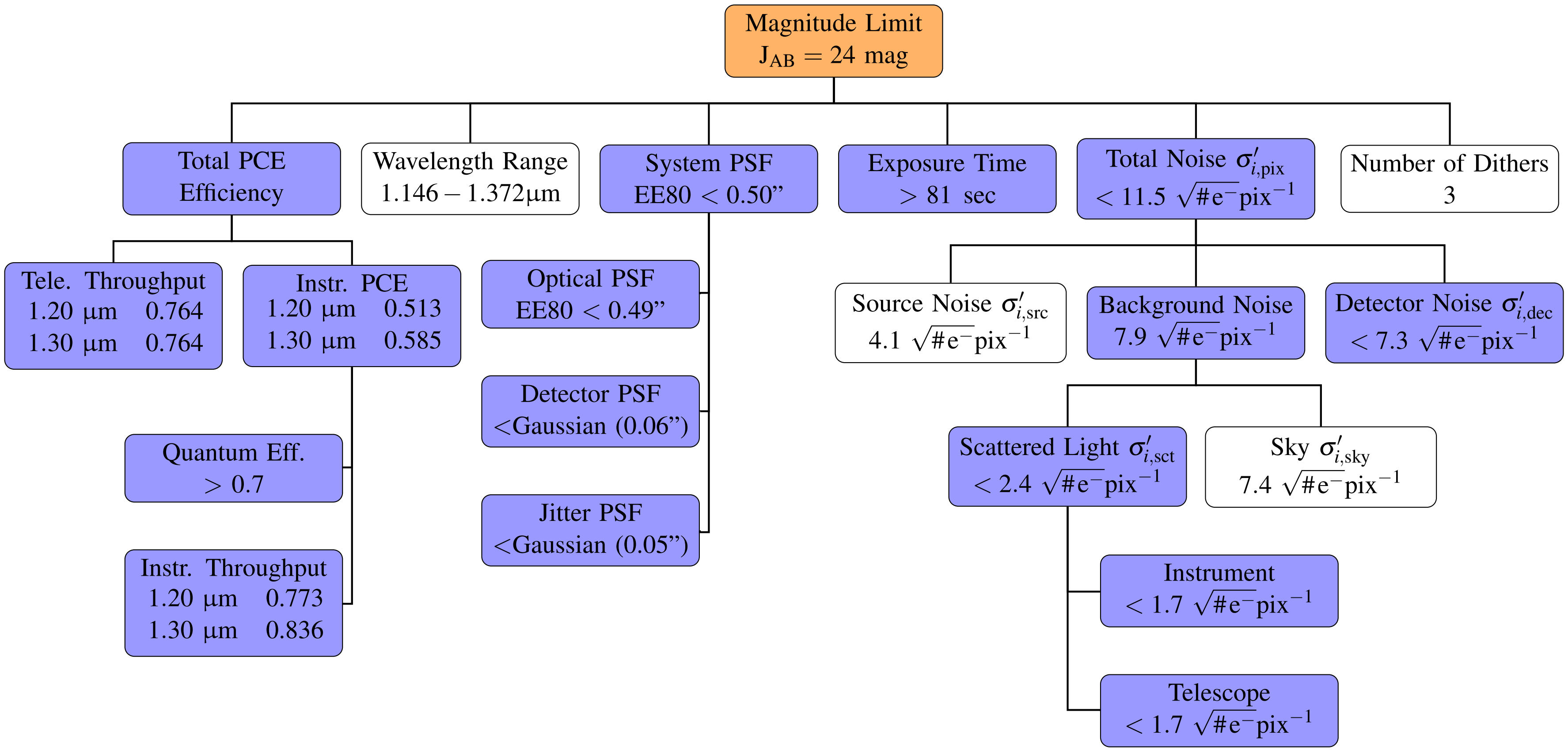


Figure 2.6: The flow-down of J-band detection limit requirement ([12] WS.2.2-3) into instrument and telescope requirements (see Figure 2.5 caption for details).

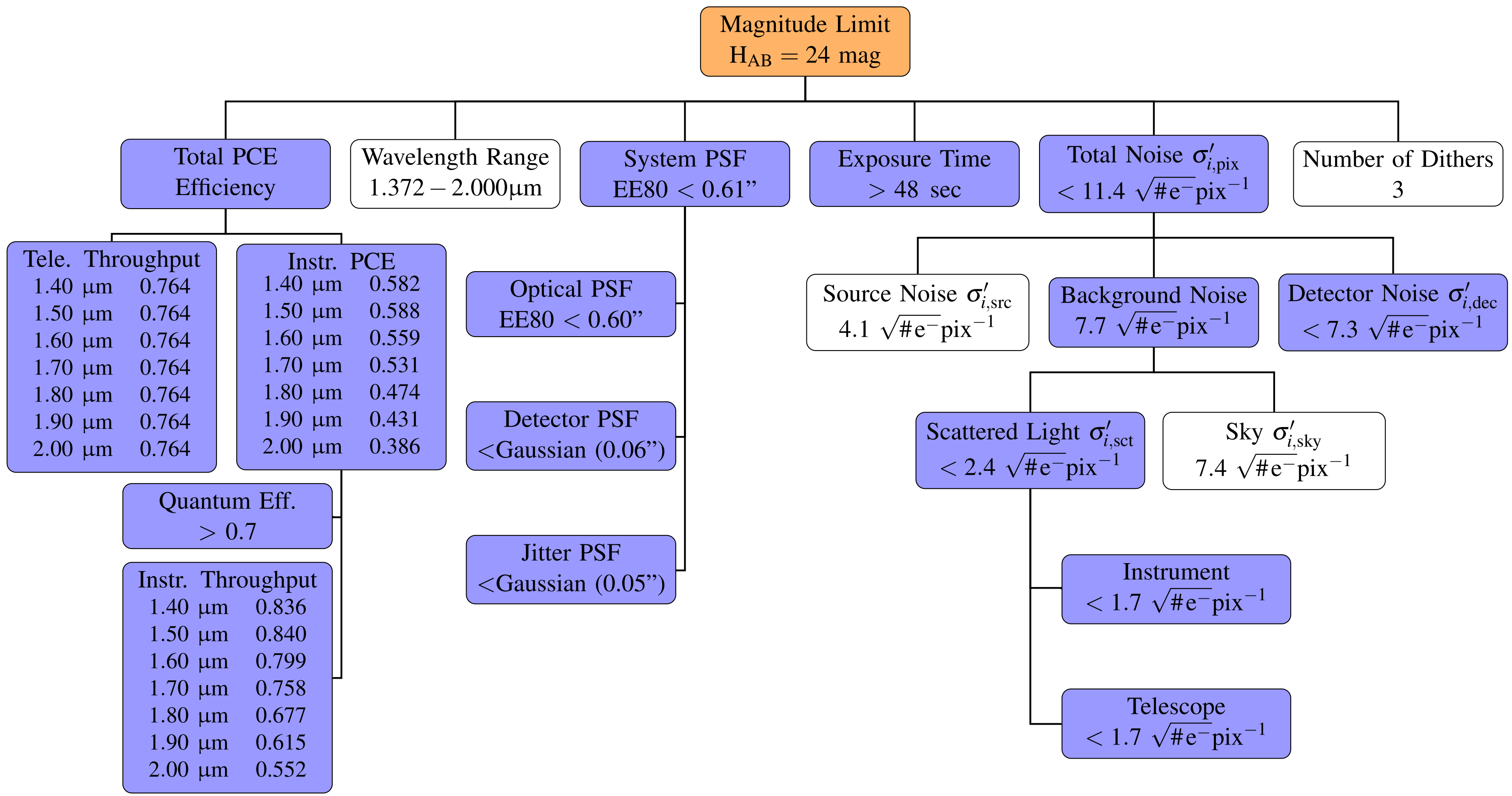


Figure 2.7: The flow-down of H-band detection limit requirement ([12] WS.2.2-3) into instrument and telescope requirements (see Figure 2.5 caption for details).

### 2.3.4 Detector Functioning Space

After initially specifying the detector performance in terms of quantum efficiency, readout noise and dark currents separately, it was requested to define a functioning space for the detectors in which the photometric performance requirements would be met. This function space should be bound by the total pixel noise tolerable for a range of quantum efficiencies. It would, for example, be possible to accept a detector with a higher total noise if the quantum efficiency was also higher. A requirement specified in this form gives the detector vendor more flexibility, but still ensures that the scientific performances can be met.

This functioning space is identified by finding the maximum total pixel noise permissible to still reach the detection limit requirement with different detector quantum efficiencies. A change in the detector quantum efficiency will result in a different source signals $Rt$, sky background signals $\Omega^2 R_{\text{sky}}\, t$ and scattered light signals $\gamma\Omega^2 R_{\text{sky}}\, t$ being recorded in the detectors. The total detector noise $\sigma_{i,\text{dec}}$, per pixel, includes contributions from the dark current $D$ and the readout noise $\beta$:

$$\begin{aligned} \sigma^2_{i,\text{dec}} &= \sigma^2_{i,\text{DC}} + \sigma^2_{i,\text{RN}} \\ &= Dt + \beta^2 \quad , \end{aligned}$$

for a single dither exposure of time $t$. Equation 2.5 can be re-expressed in terms of detector quantum efficiency $\eta$ and total pixel noise $\sigma^2_{i,\text{dec}}$ as

$$\phi = \frac{\dfrac{\eta}{\eta_0} R\,\alpha\, t\, d}{\sqrt{\left[R\,\alpha + n\Omega^2\left(R_{\text{sky}} + \gamma R_{\text{pole}}\right)\right]\dfrac{\eta}{\eta_0}\, t\, d + n\, d\, \sigma^2_{i,\text{dec}}}} \quad , \tag{2.6}$$

where $\eta_0 = 0.7$ is the detector quantum efficiency incorporated in the photon-to-electron conversion efficiencies used to translate the fluxes entering the telescope into signals in the detector (Figure 2.2). Equation 2.6 can then be arranged to find the permissible total pixel noise $\sigma^2_{i,\text{dec}}$ for different values of detector quantum efficiencies $\eta$, which still allow the $5\sigma$ detection limit requirement ($\phi = 5$) to be met within the nominal exposure times (Table 2.3).

The calculated functioning spaces are shown in gray in Figure 2.8. If the detector performances fall within this region, then the channel's detection limit requirement would be met. The space is bounded with quantum efficiencies of 0.6 and 1.0: a value greater than 1.0 is unfeasible and a detector with a quantum efficiency below 0.6 would not be accepted as this would be indicative of a defective device. This functioning space was provided to the detector vendor.

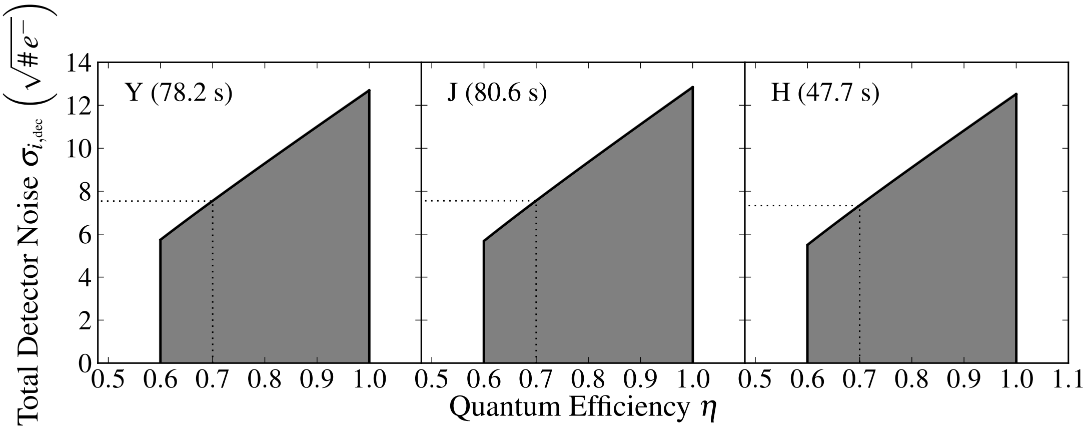


Figure 2.8: The functioning spaces (gray) identified for the NISP detectors coming from the photometry channel's $5\sigma$ detection limit ([12], WS.2.2-3). If the detector performances fall within this region, then the detection limit requirement would be met with the nominal exposure times. A dotted guide line is included at the previously considered detector parameters ($\eta = 0.7$, 0.1 e$^-$ sec$^{-1}$ pix$^{-1}$ and $\beta = 7$ e$^-$ RMS – see Table 2.2). The functioning spaces for the different bands are similar, but not identical.

### 2.3.5 Telescope Pointing Stability

In the previous subsections, the telescope's pointing instability (jitter) has been considered as a blurring of the system PSF, which was modeled as a convolution with a Gaussian function that had a FWHM = 0.05 arcsec. The NISP Instrument's three photometry filters are housed in a large filter wheel. When rotated, this mechanism will introduce significant torque perturbations to the satellite, which could cause the telescope's line-of-sight to drift sufficiently far that the satellite's fine guidance system could lose its star lock. The time required for the fine guidance system to regain its lock, and for the satellite to stabilize, could be much longer than the 10 s assumption made when defining the NISP Photometric Channel's operating mode (Figure 2.4). If so, this could drastically reduce the survey efficiency, especially considering that the NISP filter wheel must be operated four times per dither pointing (Open Position $\rightarrow$ Y-Filter $\rightarrow$ J-Filter $\rightarrow$ H-Filter $\rightarrow$ Open Position). It is therefore pertinent to investigate how the photometric performance of the channel would be deteriorated with a higher satellite instability. If the stability requirement could be relaxed then it would not be necessary to wait as long for the satellite to settle after a filter wheel motion, which could potentially significantly increase the survey efficiency.

To do this, the $5\sigma$ detection limit in each of the photometric bands was calculated with system PSFs that have an increasing telescope jitter contribution. The telescope jitter contribution is again modeled as a convolution with a Gaussian function, but the FWHM of which is varied in the range from 0 to 0.25 arcsec. A larger system PSF will spread the point source flux over more pixels and noise will therefore be more significant. Equation 2.5 is utilized again to estimate the channel's radiometric performance. In this calculation the exposure times are fixed to their nominal values (Table 2.3). System PSFs with different jitter contributions are constructed, and these are used to calculate the fraction of light from a point source $\alpha$ that would fall within a centered $2 \times 2$ pixel aperture. It is through this $\alpha$ parameter alone that the jitter contributions are included in this calculation. The resulting $5\sigma$ detection limits are shown in Figure 2.9 as a function of the jitter PSF FWHM.

From the results presented in Figure 2.9, I conclude that the currently defined satellite stability requirement (Jitter PSF < Gaussian (0.05") – see Figures 2.5, 2.6 and 2.7) is too stringent for the NISP photometric measurements; it cannot be justified from the photometric detection limit requirement. A relaxation of the telescope's stability requirement, up to a FWHM = 0.17 arcsec, would not have a significant impact on the point source detection limit. The same magnitude depths could be recovered by increasing the nominal exposure times by $\sim 3$ %. In addition, I also conclude that improving the satellite stability would not increase the NISP Photometric Channel's point source detection limit at all in the J- and H-bands, and only very slightly in the Y-band. In essence, a blurring from the satellite instability within this range has a very minor effect on the NISP Photometric Channel's system PSF. I therefore recommend that the satellite stability requirement is relaxed.

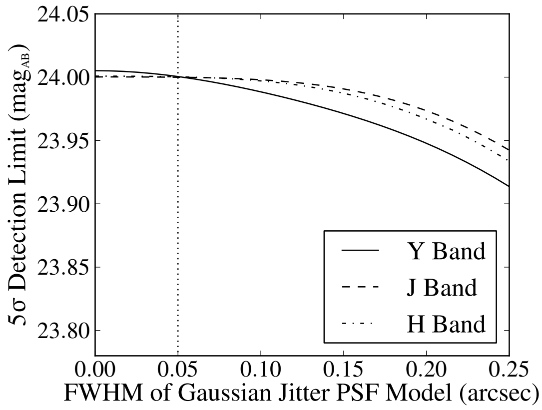


Figure 2.9: The variation in the $5\sigma$ detection limit of the NISP Photometric Channel with an increasing telescope jitter contribution. The currently defined telescope jitter requirement is shown with the vertical dotted guide line. The $5\sigma$ detection lines for the different band cross at this value, as this jitter PSF FWHM was used in the derivation of the exposure times.

## 2.4 Deep Field Revisits

In addition to the Wide Survey, the Euclid Mission will also perform a deeper survey for calibration and secondary science purposes. For the NISP Photometric Channel, the only requirement to change for the Deep Survey, compared to the Wide Survey, is the ($5\sigma$) point source detection limit of the resultant dataset. The Deep Survey is required to have a point source detection limit that is 2 $mag_{AB}$ deeper than the Wide Survey ([12], DS.2.2-2), so the final photometric measurements must reach a ($5\sigma$) detection limit of $Y_{AB}$, $J_{AB}$, $H_{AB}$ = 26 mag. For calibration reasons, the NISP Spectroscopic Channel requires that the Deep Field is covered with the same dithered observing strategy as the Wide Survey ([12], DS.2.2-14). The deeper measurements must therefore be formed by stacking multiple passes over the Deep Field. Initially 40 passes were planned [15], and in this section the calculation I performed to verify that this is sufficient to meet the Deep Field depth requirements is presented.

Each pass over the Deep Field is assumed to use the same four dither observing strategy as the Wide Survey (introduced in Subsection 2.3.1), with the nominal exposure times given in Table 2.3. A point source is again considered to be measured in three of the four dithered exposures per visit. If the revisits were exactly aligned, this would correspond to $\sim 92$ % of the Deep Field. A trivial modification to Equation 2.5 is made: the number of dithers $d$ is replaced with the total number of dithered measurements $kd$ taken during the $k$ revisits. All the other parameters in this calculation are kept constant (Table 2.2). The number of revisits is varied in the range $k = 1$ to $k = 40$, and the required source signal $R$ to reach a $5\sigma$ detection limit is found in each case. This is then translated into the required flux entering the telescope with the photon-to-electron conversion efficiency shown in Figure 2.2 and the Euclid main mirror diameter of 1.2 m, which can in turn be translated into point source magnitudes.

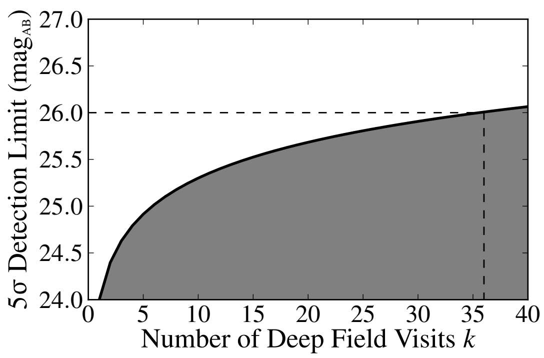


Figure 2.10: The increase in the $5\sigma$ detection limit of the Y-band's dataset with the increase in the number of revisits to the Euclid Deep Field. The gray area corresponds to point source magnitudes that will be detected above the detection limit. The $Y_{AB}$, $J_{AB}$, $H_{AB}$ = 26 mag detection limit requirement is identified with the dotted guide line.

The increase in the detection limit with the number of passes over the Deep Field is presented in Figure 2.10. The results are comparable for the different photometry bands, so only the Y-band result is presented. As can be seen in this figure, 36 passes over the Deep Field are required to meet the more stringent 5$\sigma$ detection limit requirement. Since the current mission strategy assigns 40 passes [15], I conclude that the Deep Field detection limit can be met with the current mission design and the baseline instrument configuration.

## 2.5 Instrument Saturation Limit

The NISP Instrument's near-infrared detectors have a finite well depth; with bright sources some pixels will saturate. This section details the calculation used to estimate the channel's point source saturation limit. To do so, a number of worst case assumptions are made, but these differ from those taken in the radiometric performance calculations (Section 2.3). In this case, small system PSFs, high throughputs and high detector quantum efficiencies are critical.

Here, the best performing optical system[17], identified in the same Monte Carlo run used to generate the near-worst case optical system for the radiometric performance calculation (Section 2.3), is used. This is representative of the best implementation of the optical system that can be manufactured. For each band, polychromatic optical PSFs were generated from this system on a $3 \times 3$ grid across the focal plane. The best performing focal plane position was identified, again using the EE50 and EE80 values (see Subsection 2.2.1), with the corresponding PSFs used to calculate the fraction of light from a point source that would fall within a centered $1 \times 1$ pixel aperture. It is the saturation of this pixel that is considered in this calculation. The following additional worst case assumptions were also made: (i) the satellite is perfectly stable, so that the optical PSF is not blurred due to telescope jittering, (ii) the detector effects that distribute signal to neighboring pixels – such as charge diffusion – are negligible, (iii) the channel's throughput is 10% higher than the current requirement and (iv) the best performing detectors will have a quantum efficiency of 0.9.

The above assumptions are used to calculate the source flux required to reach the pixel's minimum full well capacity, specified as $60,000$ electrons on the detector vendor [13], with different single dither exposure times. Signal contributions from the sky background, scattered light, dark currents and thermal contamination are all ignored in this calculation, as these are negligible in such a high source flux case. The results for the three bands are shown in Figure 2.11. I estimate the NISP Photometric Channel's saturation magnitudes, with the margin exposure times (Table 2.3), as: $Y_{AB} = 16.88$; $J_{AB} = 16.94$; $H_{AB} = 16.82$ mag. These saturation limits are used in the survey simulations presented in Chapter 4.

[17]Zemax File: 06_033_003_c_best_MC_TO091.ZMX – F. Grupp (Max-Planck-Institut für extraterrestrische Physik – Germany)

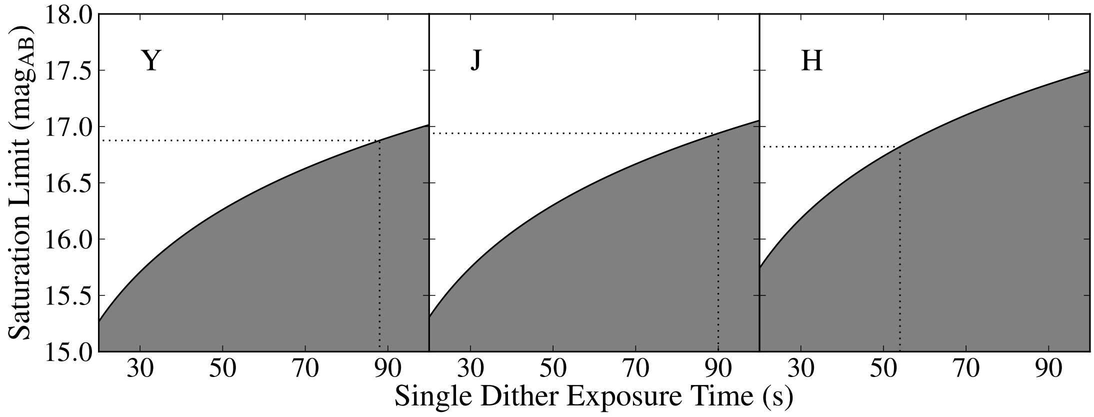


Figure 2.11: The saturation limit of the NISP Photometric Channel as a function of single dither exposure time. The margin exposure times and the corresponding saturation limit for each band are identified with the dotted guide line ($Y_{AB} = 16.88$, $J_{AB} = 16.94$, $H_{AB} = 16.82$ mag). Contributions to the pixel count from the sky background, scattered light, dark currents and thermal contamination are not considered, as these are negligible in such a high source flux case.

## 2.6 Sky Coverage

The active area of the NISP Instrument's focal plane, which is made up from a mosaic of 16 ($4 \times 4$) of Teledyne Hawaii 2RG detectors [9], does not completely cover the channel's field-of-view. In such a mosaic, mounting structures cause unavoidable gaps between active detector areas. In the current configuration of the $\sim$ 156 mm $\times$ 165 mm focal plane, there will be gaps of 3 and 6 mm between the 36.7 mm $\times$ 36.7 mm active detector areas in the x- and y-directions respectively (see Figure 2.12(a))[13]. The Euclid Mission will measure each patch of sky in four dithered exposures, the pointing of which will be offset slightly. In the NISP Photometric Channel, this dithering will not only provide a better PSF sampling in the the combined image, but will also reduce the impact of the gaps in the active focal plane coverage. Dithering is done at satellite level and is therefore common to all of Euclid's channels. As the NISP focal plane has the largest gaps between active detector areas, it is driving the magnitude of the dither offsets. In the baseline dithering strategy the first dither exposure is taken at a specific point on the sky, the telescope's line-of-sight is then shifted by a further $x, y = (50, 100)$ arcsecs for the second dither exposure, then shifted again by $x, y = (0, 100)$ arcsecs for the third and finally by $x, y = (0, 100)$ arcsecs for the fourth [15]. These dither shifts are shown with the red arrows in Figure 2.12(a). To meet the high level science goals, the NISP Photometric Channel is required to cover the $\sim 15,000$ deg$^2$ Wide Survey with a certain efficiency: (i) greater than 43 % of the survey must be imaged in all four of the four dithered exposures ([12], WS.2.2-6) and (ii) greater that 92 % of the survey must be imaged in three of the four dithered exposures ([12], WS.2.2-7). This section details the simulation performed to verify these requirements with the baseline NISP focal plane layout and the current dithering strategy.

To verify this requirement, a focal plane sized patch of sky within the survey is considered. An active focal plane footprint map is projected onto this patch and this is shifted according to the defined dithering strategy. This patch of sky is considered to be exposed in a maximum of four dithers, overlaps between the four dither observation sets are not considered. That is to say, the sky is assumed to be perfectly tiled. The first step in the simulation is the creation of a focal plane footprint map on the sky. For accuracy, a map with a $1 \times 1$ pixel resolution was created (see Figure 2.12a). This map is shifted over the patch of sky according to the dithering strategy. The sections of this patch of sky covered by each dithered exposure are recorded and this is used to calculate the coverage of the sky patch, and therefore the survey.

Figure 2.12 shows the sky coverage in three different cases: (b) corresponds to a focal plane with no dead pixels, (c) corresponds to a focal plane with 5 % randomly distributed dead pixels and (d) corresponds to a focal plane with 10 % randomly distributed dead pixels. The fraction of the survey covered with different numbers of dithers is tabulated in Table 2.4.

| Number of Dithered Exposures Observed In | Fraction of Survey (%) Without Dead Pixels | | | With Dead Pixels | |
|---|---|---|---|---|---|
| | Requirement | No Dithering | Dithering | +5 % | +10 % |
| $\geq 1$ | - | 83.88 | 99.33 | 99.06 | 98.75 |
| $\geq 2$ | - | 83.88 | 94.18 | 93.67 | 92.45 |
| $\geq 3$ | $> 92$ | 83.88 | 92.29 | 85.51 | 78.16 |
| $\geq 4$ | $> 43$ | 83.88 | 49.73 | 40.50 | 32.63 |

Table 2.4: The fraction of the Euclid Wide Survey that will be observed in more than one, two, three or four of the four dithered exposures. The survey efficiency requirements coming from the high level science requirements are shown along with the survey coverage that would be obtained without shifting the telescope's line-of-sight between the dithered exposures (and with no dead pixels in the focal plane). The survey coverage with the baseline dithering strategy is shown for three cases: (i) where the focal plane has no dead pixels, (ii) where the focal plane has 5 % randomly distributed dead pixels and (iii) where the focal plane has 10 % randomly distributed dead pixels.

The sky coverage lost due to dead pixels is not included in these requirements. A separate requirement ([12], WL.2.1-13) defines the maximum permissible number of pixels lost per photometry frame as $< 10$ % (end-of-life – EOL). This, I have budgeted as a 8 % for non-operable pixels (EOL) and 2 % for the pixels temporarily lost due to cosmic ray events in the focal plane or readout electronics. Nevertheless, simulations with dead pixels are also presented to show how the sky coverage is reduced. Note that this cannot trivially be transfered to the coverage of the resultant catalog, as a single dead pixel does not necessarily completely destroy a measurement; the signal in the surrounding pixels could still be used in a drizzling procedure.

From the results in Table 2.4, I conclude that the sky coverage requirements will be met with the baseline configuration of the NISP Instrument's focal plane and the current dithering strategy.

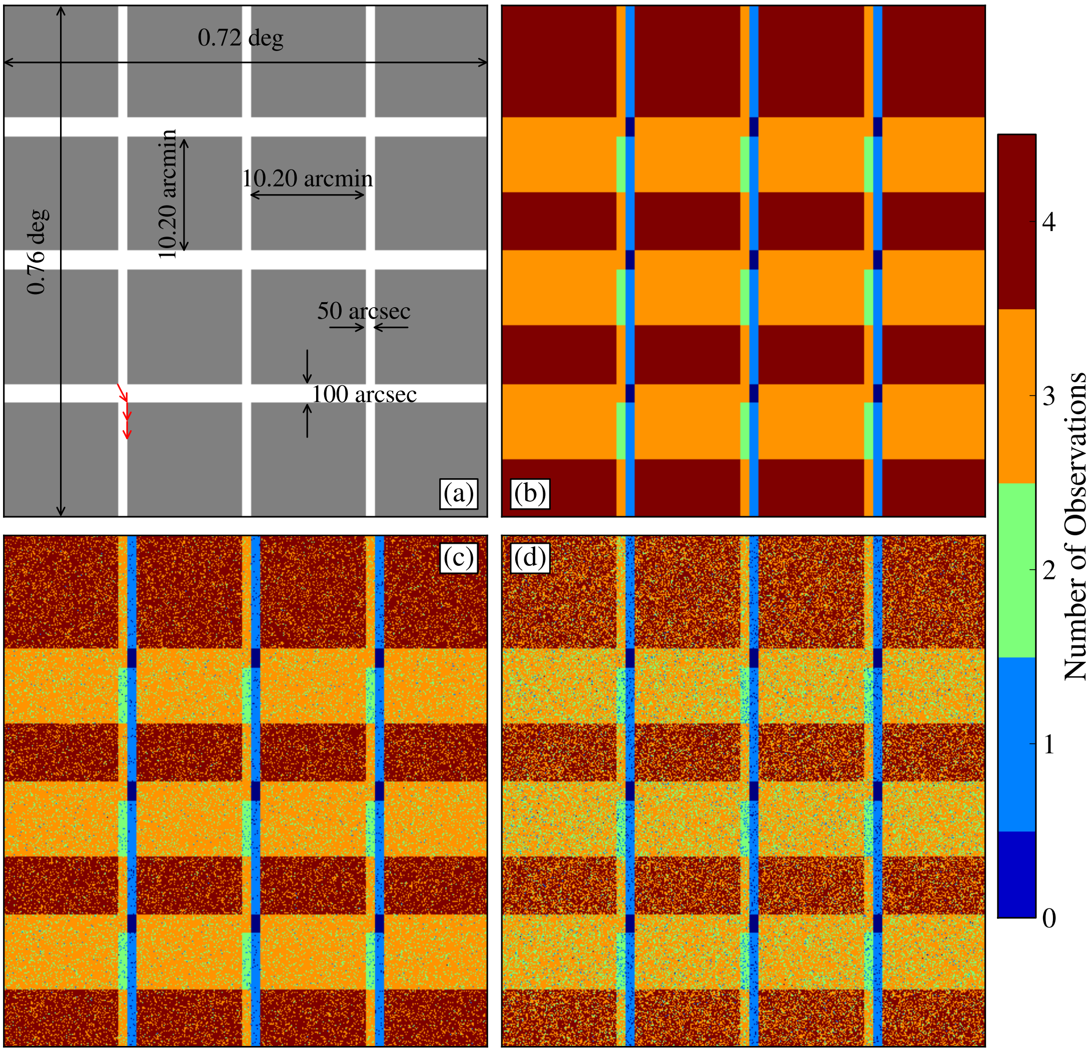


Figure 2.12: (a) The footprint of the NISP Photometric Channel's active focal plane area projected onto the sky. The red arrows show the magnitude and direction of the shifts between the four dithered exposures of the patch of sky. (b) – (d) The simulated coverage of the focal plane sized patch of sky with color coding to indicate the number of dithered exposures that the constituent areas are measured in: (b) corresponds to a focal plane with no detector dead pixels, (c) corresponds to a focal plane with 5% randomly distributed dead pixels and (d) corresponds to a focal plane with 10% randomly distributed dead pixels.

## 2.7 Wide Survey Depth Variation

In the final section of this chapter, the expected quality of the Euclid Wide Survey dataset from the NISP Photometric Channel is summarized. The results of the survey coverage simulation from Section 2.6 are presented, along with the corresponding $5\sigma$ detection limits, in Table 2.5. The $5\sigma$ detection limits are calculate from Equation 2.5 for the number of dithers $d = 1$ to $d = 4$. The nominal exposure times (Table 2.3) are included in this calculation.

| Number of Dithered Exposures Observed In | Fraction of Survey (%) | Detection Limit ($\text{mag}_{\text{AB}}$) |
|---|---|---|
| 0 | 0.67 | - |
| 1 | 5.15 | 23.35 |
| 2 | 1.89 | 23.76 |
| 3 | 42.56 | 24.00* |
| 4 | 49.73 | 24.17 |

Table 2.5: The NISP Photometric Channel's sky coverage of the Euclid Wide Survey. The detection limits are comparable in all bands. Only 0.67 % of the Wide Survey will never be observed. *By design.

## 2.8 Outlook

The baseline implementation of the NISP Photometric Channel was reviewed by the European Space Agency in the summer of 2011. The results of this review – along with those of the other Euclid channels and the spacecraft concepts – will be fed into the Cosmic Vision Program selection process, in which Euclid is in competition with two other missions (Plato [6] and Solar Orbiter [5]) for two launch slots. If the Euclid Mission is selected, then the current design of the NISP Instrument will be developed, prototyped and manufactured starting in early 2012. It is important to note that the baseline implementation of the NISP Photometric Channel, the performance of which was under my stewardship, meets all the high level science requirements [10].

# Chapter 3

# The NISP Instrument's Photometric Calibration Strategy[1]

**Chapter Abstract:** This chapter details the NISP Photometric Channel's calibration strategy, which I defined under my responsibilities as NISP Photometry Scientist. This calibration plan will be used to reach the stringent photometric error targets on the channel: better than 1.5 % for the post-calibration relative photometric error and better than 3 % for the post-calibration absolute photometric error. I have flown these values into high-level instrument error budgets by identifying the main error sources within the channel's measurements. These budgets will be now used by the NISP Instrument Team to define requirements on the channel's subcomponents. In this chapter I also define the calibration processing flow for the channel's science data. From this I am able to identify the required calibration data and the instrument operation modes needed to obtain them. This chapter gives an overview of the channel's calibration strategy, which also acts as an introduction to the more specific work I have performed on the self-calibration of the photometry dataset and the development of a flat-field calibration source concept presented in Chapters 4 and 5 respectively.

## 3.1 Introduction

During the Euclid Development Phase [2], the two NISP Instrument Scientists were responsible for developing the calibration procedure for the instrument. As Photometry Instrument Scientist, I focused on the calibration of the photometric channel, with the Spectroscopic Instrument Scientist[2] concentrating on the spectroscopic channel. This chapter details the calibration strategy I identified for the photometric channel, with Chapters 4 and 5 concentrating on specific

[1] This work has formed part of the *NISP Calibration Plan* [16].
[2] A. Ealet (Centre de Physique des Particules de Marseille – France).

aspects of this plan. For the photometric channel, the calibration is divided into two parts that are considered separately: the *relative* photometric calibration and the *absolute* photometric calibration. It is prudent to start with the definitions of these two quantities:

1. The *Relative* Photometric Calibration is the process of correcting for variations in the instrument response, both spatially and temporally. After calibration, measurements of identical sources – observed at different times in the survey and at different parts of the focal plane – must have a root-mean-square (RMS) error of less than the relative photometric error requirement (in the limit of negligible photon noise).

2. The *Absolute* Photometric Calibration is the process in which the measured signals are tied to the actual photon fluxes entering the telescope. After the absolute calibration, the measurement of the flux entering the telescope must be accurate to better than the absolute photometric error (again in the limit of negligible photon noise).

The NISP Photometric Channel is required to supplement the visible shape measurements of distant galaxies with multi-band, near-infrared photometry. These measurements will be used with multi-band, ground-based, visible photometry to estimate the galaxies' redshifts. The mission's high level photometric redshift accuracy requirement ([12], WL.1-5) propagates[3] to only a requirement on the relative photometric error of the NISP Photometric Channel. The photometry dataset is required to be highly uniform within the survey, with the post calibration relative photometric errors required to be lower than 1.5 %. The accuracy of the absolute photometry, and indeed the variation in zero points between bands, is not constrained from any of the mission's primary science cases, although a goal of $< 3$ % is specified from the secondary science cases. Table 3.1 summarizes the relative and absolute error specification. These apply to the final, calibrated dataset from the channel in the limit of negligible photon noise.

| Type | ID [12] | Description | Value |
|---|---|---|---|
| Requirement | WL.2.1-21 | Post Calibration Relative Photometric Error | $< 1.5\%$ |
| *Goal* | WS.2.2-16 | Post Calibration Absolute Photometric Error | $< 3\%$ |

Table 3.1: The maximum photometric errors specified for the NISP Photometric Channel. These values apply in the limit of negligible photon noise.

## 3.2 Error Budgets for the NISP Photometric Channel

As NISP Photometry Scientist, it was my responsibility to break the high level error specifications into error budgets for the instrument. These will be used by the NISP Instrument Team to

[3]H. Hoekstra (Leiden Observatory – The Netherlands) and T. Kitching (University of Edinburgh – United Kingdom)

define requirements on instrument subcomponents. To create the error budgets presented in this section, the main sources of errors within the channel's measurements are identified and the total error is distributed. The error budgets for the instruments on the James Webb Space Telescope (JWST) have been used as a guide for this breakdown [17], although the Euclid requirements are more stringent. These individual budget allocations apply to the final, post-calibration photometric results, which will be made up from the multiple measurements of each source. These budgets apply separately for each photometry band. The NISP Photometric Channel's raw data will require a number of calibration steps to get the errors below the specified values. These are detailed in Section 3.4.

### 3.2.1 Relative Photometric Calibration Budget

A high level breakdown of the relative photometric error requirement, introduced in Section 3.1, is shown in Table 3.2. The individual budget contributors are detailed in the following subsections.

| **Error Source** | **Budget Allocation** |
|---|---|
| Pixel-to-Pixel Flat Field | 0.5% |
| Large-Scale Flat Field | 0.5% |
| Detector and Readout Electronics Effects | 0.6% |
| Intrapixel Sensitivity Variation | 0.8% |
| Calibration Stability | 0.8% |
| Background Subtraction | 0.2% |
| Data Processing | 0.2% |
| *Margin* | *0.17 %* |
| **Total Relative Photometric Error** | **1.5 %** |

Table 3.2: A high level breakdown of the NISP Photometric Channel's post calibration relative photometric error requirement. This budget applies to the final photometric measurements, constructed from the multiple dithered observations, and to each band separately. The error contributions are assumed to be uncorrelated and therefore the individual error allocations are summed in quadrature.

#### Flat-Field Correction Errors

The errors associated with the flat-fielding procedure, that is the process of determining and accounting for the variations in the detector and system response to perfectly uniform illumination entering the telescope, is subdivided into two parts:

1. The small-scale ($< 50$ pixel) flat-fielding errors that apply on a pixel-to-pixel scale (i.e. the pixel-to-pixel flat-field errors), such as those coming from an imperfect correction

for the variations in quantum efficiencies between neighboring pixels. The above error budget allocates an error of 0.5% to these corrections.

2. The large-scale ($> 50$ pixel) flat-fielding errors that apply on a focal plane wide level, such as those coming from the imperfect corrections for the variations in sensitivity across and between detectors. The above error budget allocates an error of 0.5% to these corrections.

During the calibration procedure, corrections on both of these scales must be applied. The method for calibrating these two scales will be different: the small-scale flat-field correction will use an on-board calibration source (see Subsection 3.4.2) and the large-scale flat-field correction will be retrospectively calibrated with the large amount of redundant data within the Euclid surveys (see Subsection 3.4.3). Super-Sky Flats will supplement the flat-field calibration source exposures, but the sky is too faint at the photometric channel's wavelength range ($0.92 - 2.00\mu$m) to generate Super-Sky Flats at the required frequency. An on-board calibration source is therefore unavoidable (see Section 3.3).

**Background Subtraction Errors**

This 0.2 % budget allocation accounts for errors associated with the subtraction of the sky background, the thermal contamination and the scattered light contamination from the science exposures.

**Detector Effects**

The error of 0.6 % applies to the contributing effects from the detector and readout electronics. These effects include bias correction errors, dark current subtraction errors, interpixel effects, non-linearity correction errors, persistence and reference pixel correction errors. This budget does not include intrapixel sensitivity variation effects; these are considered in a separate budget allocation (see below).

**Intrapixel Sensitivity Variation**

The NISP Photometric Channel is undersampled, with the full-width-half-maximum (FWHM) of the point-spread-function (PSF) less than one pixel. Variations in the sensitivity within a pixel could therefore potentially introduce significant errors into the photometric measurements, particularly for point sources. Calibration corrections, such as flat-fielding, could not correct for these errors. There are no data available in the literature on the intrapixel sensitivity variations for the baseline Hawaii 2RG near-infrared detectors, so the form and magnitude of this variation is unfortunately unknown. The impact of this effect on the relative photometric accuracy of the NISP Photometric Channel has been modeled by G. Seidel (Max-Planck-Institut für Astronomie – Germany) and this has been used to validate that the 0.8 % allocation is realistic with the current estimations of the magnitude of this effect[4].

#### Calibration Stability

This budget of 0.8 % accounts for errors introduced into the measurements from drifts in calibratable parameters between calibration measurements. For example, this would include changes in the detectors' dark currents between dark exposures, or changes in pixels' sensitivity between flat-field exposures.

#### Data Processing Errors

The high level errors specified on the channel (Table 3.1) apply to the final photometric dataset obtained after all the data processing. It is therefore necessary to include an allocation for the data processing within this error budget. This 0.2 % allocation accounts for limitations in the algorithms used in the data processing. For example, the signal extraction algorithms will include a point-spread-function (PSF) model, not the true PSF, and this will introduce errors.

### 3.2.2 Absolute Photometric Calibration Budget

A high level breakdown of the absolute photometric error, specified in Section 3.1, is shown in Table 3.3. There is no science requirement on this error, but a goal of $< 3\%$ is specified from secondary science cases. The individual budget contributors are detailed in the following subsections.

| **Error Source** | **Budget Allocation** |
|---|---|
| Error in Flux Standards | 2.0% |
| Relative Photometric Error | 1.5% |
| Aperture Correction | 1.0% |
| Data Processing | 1.0% |
| *Margin* | *0.8 %* |
| **Total Absolute Photometric Error (goal)** | **3.0 %** |

Table 3.3: A high level breakdown of the NISP Photometric Channel's post calibration absolute photometric error *goal*. There is no requirement on this error. This budget applies to the final post-calibration dataset, and to each band separately. The error contributions are assumed to be uncorrelated and therefore the individual error allocations are summed in quadrature. The requirement applies in the limit of negligible photon noise.

[4]More details on this work are intentionally omitted here, as they have yet to be published.

#### Error in Flux Standards

This 2.0 % budget allocation accounts for both uncertainties in the knowledge of standard sources and the extrapolation to the NISP Photometric Channel's wavelength ranges.

#### Relative Photometric Error

The relative photometric error of 1.5 % must be included in this budget as the temporally and spatially localized observations of standard stars will be used to constrain the survey wide absolute photometric calibration. The relative photometric error of the NISP Photometric Channel is described in Subsection 3.2.1.

#### Aperture Correction

Due to the extended nature of the optical PSF, the flux in the outer regions will be lost, both in the measurement noise and the signals from other sources. The source extraction algorithms will only fit the PSF over the central region. This 1.0 % budget contribution accounts for the errors introduced during the correction for this limitation.

#### Data Processing

As the absolute photometric goal applies to the final dataset, it is necessary to include an allocation for data processing within this budget. The absolute photometric error goal is less stringent than the relative photometric error requirement, and as such it is possible to assign a more relaxed allocation of 1.0 % to the data processing in this budget.

## 3.3 Is an On-Board Calibration Source Required?[5]

This section considers whether the NISP Instrument requires an on-board calibration source to meet the budget allocation given in Table 3.2 for the small-scale flat-field correction. The dominant effect on small-scales that must be corrected is the variation in neighboring pixels' sensitivity. Larger scale variations will be constrained in the retrospective calibration of the dataset (see Subsection 3.4.3). In space missions, there are two options for creating flat-field maps that could be used to correct variations on these scales:

1. "Super-Sky Flats" can be produced from the science exposures themselves. Detectable sources are masked and the remaining pixel information from large numbers of different science exposures is combined. Under the assumption that each pixel has seen – on average – the same sky background, the resultant map can be used to correct for pixel sensitivity variations. At the NISP wavelengths (0.92 – 2.00 μm), the main background

[5] This work is detailed in the technical note *Justification of the NISP Instrument's Calibration Source* [18], although the calculation has been updated to reflect the latest configuration of the NISP Instrument.

contribution is from zodiacal light (Sun light reflected from dust in the solar system). Super-Sky Flats can be used to correct both small- and large-scale variations in the instrument response.

2. An internal calibration source can also be used to illuminate the NISP focal plane and generate flat-field maps. As we are only interested in a small-scale correction, large-scale structure in this illumination is permissible. Tungsten lamps produce broadband emission that can be optimized for the NISP wavelength range. By altering the filament temperature, it would be possible to illuminate the focal plane at different intensities and with different color temperatures. An internal calibration source has the potential to be much brighter than the sky background at these wavelengths.

The NISP Photometric Channel has two options for producing flat-field correction maps, they are: (i) Super-Sky Flats alone and (ii) Super-Sky Flats combined with exposures of an on-board calibration source. At the beginning of the mission, when the stability of the instrument is unknown, flat-field exposures will be required on a twice monthly timescale (see Subsection 3.5.1). To distinguish between these two options, it is pertinent to estimate the photon noise in a Super-Sky Flat created from half a month of science observations. To do so, the total signal from the zodical background accumulated during a $\sim 15$ day period is calculated. Here, a worst-case assumption is made: the satellite is assumed to be observing one of the ecliptic poles, where the zodiacal background is low, during this time. The background signal here will be Y $\sim 0.38$, J $\sim 0.40$ and H $\sim 0.65$ e$^{-}$s$^{-1}$pix$^{-1}$ (see Table 2.2). During the $4,000$ s single dither pointing [15], the NISP photometry bands will be integrating for Y = 78.2, J = 80.6, H = 47.7 s (nominal exposure times in Table 2.3). In 15 days there will be $\sim 324$ of these $4,000$ s pointings, and therefore the total signal received from the zodiacal background at the ecliptic pole during this time will be Y $\sim 6,928$, J $\sim 10,446$ and Y $\sim 10,046$ e$^{-}$pix$^{-1}$. The photon noise alone associated with these signals will be $\sim 1$ %, which is already above the small-scale flat-field correction error allocation of 0.5 % in Table 3.2. In this calculation, the inefficiency of creating these Super-Sky Maps – caused by masking detectable sources – is also not included. I therefore conclude that a dedicated on-board calibration source is required in the NISP Instrument to meet the calibration budget presented in Table 3.2. Essentially, the sky background is too faint in the NISP Photometric Channel's bands to allow Super-Sky Flats to be created at the required frequency. An internal calibration source will be significantly brighter than the sky background, which would allow high signal-to-noise flat-field exposures to be taken in a relatively short time. Flat-field exposures could therefore be taken regularly and the temporal variations in the small-scale flat-field can be well sampled. The NISP Instrument already includes a cold shutter (in the filter wheel), so a calibration source could be implemented without the need for an additional single-point-failure mechanism to block external sources during flat-field exposures. Option (ii), the combination of Super-Sky Flats and an on-board calibration source, is therefore the only viable solution for calibrating the pixel-to-pixel sensitivity variations in the NISP Instrument.

## 3.4 The NISP Photometric Channel's Calibration Strategy

In addition to identifying the main error sources in the science measurements, the NISP Instrument Scientists were also responsible for defining the scientific data's calibration flow and identifying the required input calibration data. This section details the main calibration steps required to transform the raw NISP frames into science grade data. This work focuses on the calibration flow of the NISP Photometric Channel's science data, although there are intentional overlaps with the spectroscopic processing where possible. The calibration flow can be split into three main steps: (i) the on-board preprocessing required during the detector readout, (ii) the ground based, single frame processing and (iii) the retrospective survey wide calibration. This section details these steps in turn.

### 3.4.1 In-flight Calibration Steps

The NISP Photometric Channel's detection limit ([12], WS.2.2-3) dictates a stringent $< 7\ e^-$ rms readout noise requirement on the detectors (see Subsection 2.3.3). Operating the channel's detectors[6] in a continuous, non-destructive read (NDR) mode can strongly reduce the readout noise in the final measurement. This type of readout mode is common with the baseline detectors in ground-based projects. To meet the detector performance requirements the channel will use a "Fowler 16" readout mode[7]. In such a Fowler readout mode, four pairs of NDR samples of the detectors are performed at the beginning and the end of the integration. The sets of reads at the beginning and end are averaged, and the difference in these averages gives the pixel signal. The current implementation of the Euclid mission will return a vast amount of data, and the predicted download rate is close to the maximum permitted 850 Gbits/day [2]. It is therefore not possible to download the individual NDR frame samples to ground. As such, the processing needed to combine these frames and produce the final image must be done on-board, which adds significant complexity to the instrument electronics. Before the combination of the individual NDR frames, a limited number of calibration steps must be performed on-board[8]; these are detailed in Figure 3.1. These NDR calibration steps have been kept intentionally common to both of the instrument modes, despite the fact that the NISP Spectroscopic Channel uses an up-the-ramp NDR sampling of the detectors and not a Fowler 16 NDR sampling. The calibration steps required on-board have been kept to a minimum to limit the complexity of the NISP Instrument's electronics. Loss-less compression is used to reduce the bandwidth required to transmit the final image to ground.

[6] Teledyne's Hawaii 2RG 2k×2k Near-Infrared Detectors [9].

[7] Defined by A. Ealet (Centre de Physique des Particules de Marseille – France), C. Bonoli (Istituto Nazionale di Astrofisica – Italy) and F. Bortoletto (Istituto Nazionale di Astrofisica – Italy)

[8] These were identified with A. Ealet (Centre de Physique des Particules de Marseille – France), G. Smadja (Institut de Physique Nucleaire de Lyon – France) and F. Bortoletto (Istituto Nazionale di Astrofisica – Italy). A more up-to-date version of the on-board processing steps can be found in [19].

#### Bias Correction

If uncorrected, variations in a detector's bias voltage will lead to a uniform signal variation between NDR frames. Uniform variations in the bias voltage across the detector can be corrected by using the reference channels on the detector.

#### Channel Correction

Variations in the bias level on small timescale can also be expected within a single detector, leading to variations in the signals recorded from the different video channels. An average of the light insensitive reference pixels around the detector can be used to correct for these instabilities between the individual channels.

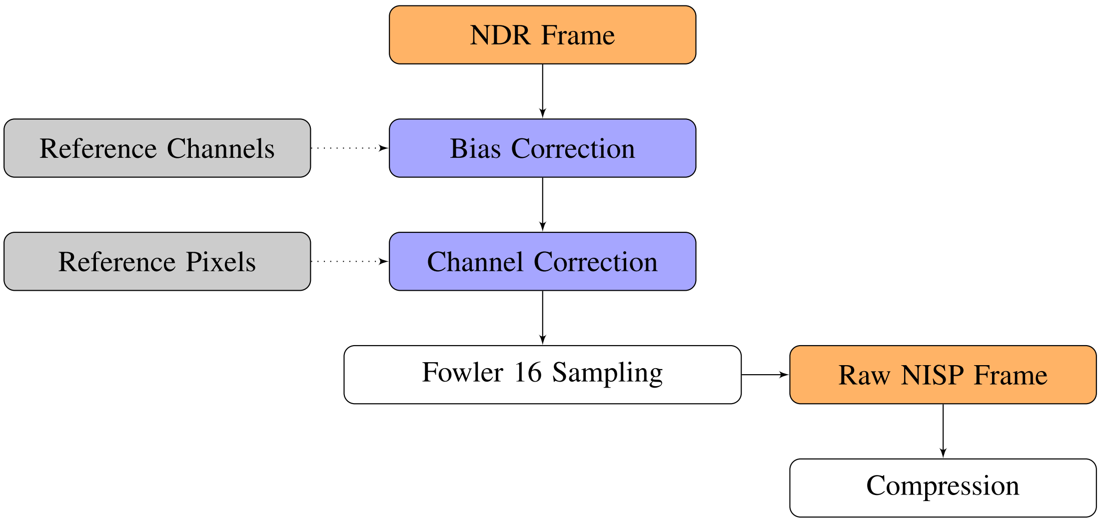


Figure 3.1: The proposed on-board calibration steps that must be performed on each of the NDR frames during the Fowler 16 reading of the NISP detectors.

### 3.4.2 Ground Calibration Steps

This subsection details the on-ground calibration steps that will be applied to the NISP Photometric Channel's raw science images downloaded from the satellite. The calibration flow is presented schematically in Figure 3.2, with the individual steps detailed in the following subsections. The final calibrated frame will then be added to the survey wide dataset, which will be calibrated further.

#### Bad Pixel Map

A map of bad pixels, both hot and dead, will be constructed from the flat-field and dark exposures (see following subsections). The first step in the ground calibration procedure will be to flag the unusable pixels within the frame, as these could contaminate the following calibration steps.

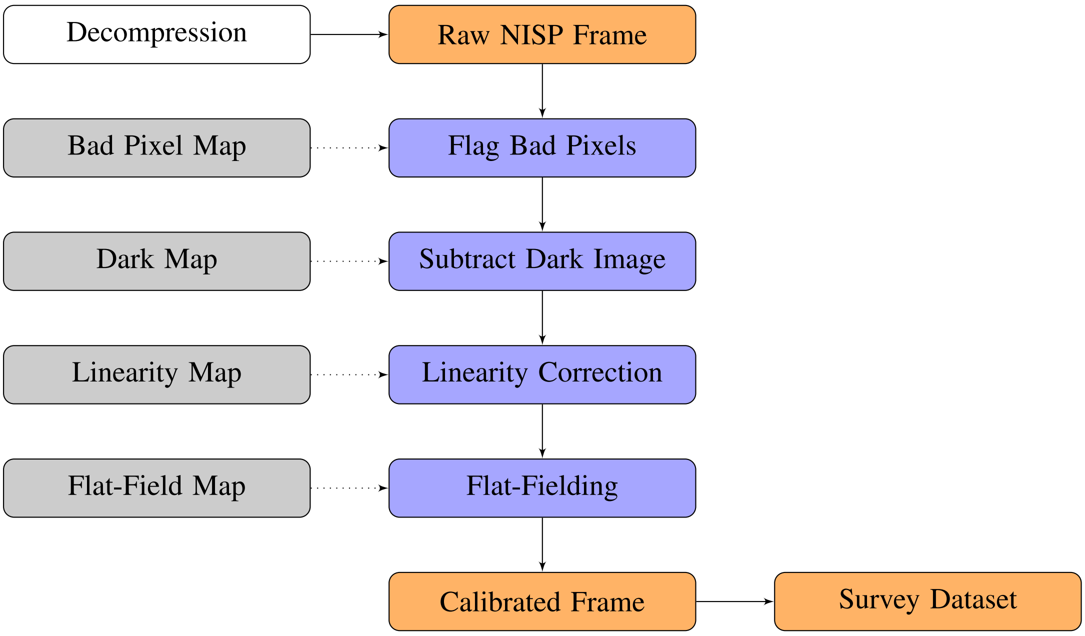


Figure 3.2: The proposed ground-based calibration steps, which will be applied to each of the NISP Photometric Channel's frames individually.

#### Dark Image Subtraction

Detector dark currents and thermal contamination from the instrument will add an unwanted background to the science frames. This background can be quantified by taking exposures with all external sources blocked from the instrument. The background can be removed from the science frames by subtracting dark maps created from these dark exposures. Dark maps will be created regularly during the mission to account for temporal variations (see Subsection 3.5.2).

#### Linearity Correction

The baseline detectors are not perfectly linear. That is to say, the sensitivity of their pixels vary as a function of the signal already accumulated within them. The linearity behavior of each of the focal plane's pixels will be measured during the ground testing campaign. These measurements will be used to correct for the non-linear sensitivity effects in the science frames by scaling the recorded counts accordingly. A. Ealet (Centre de Physique des Particules de Marseille – France) and G. Smadja (Institut de Physique Nucleaire de Lyon – France) have identified a method to monitor the pixels' non-linearities during the mission using the flat-field calibration source exposures (see Subsection 3.5.1).

#### Flat-Field Correction

The final step in the single frame calibration will be to correct for the pixel-to-pixel sensitivity variations. An on-board calibration source (see Section 3.3) will be used to illuminate the focal plane, exposures of which will be used to generate flat-field maps. The science frames can be divided by these maps to correct for the small-scale ($< 50$ pixel) sensitivity variations between pixels. The large-scale structure in these flat-field maps can be constrained during the self-calibration procedure detailed in Chapter 4. Exposures of the calibration source will be performed regularly during the mission to account for temporal variations in the pixel sensitivities. (see Subsection 3.5.1).

### 3.4.3 Survey Wide Calibration

The survey wide dataset will contain a lot of calibration information. The final stage of the NISP Photometric Channel's calibration procedure exploits this information, and provides the final absolute calibration. The survey wide calibration steps are shown schematically in Figure 3.3, with the individual steps discussed in the following subsections.

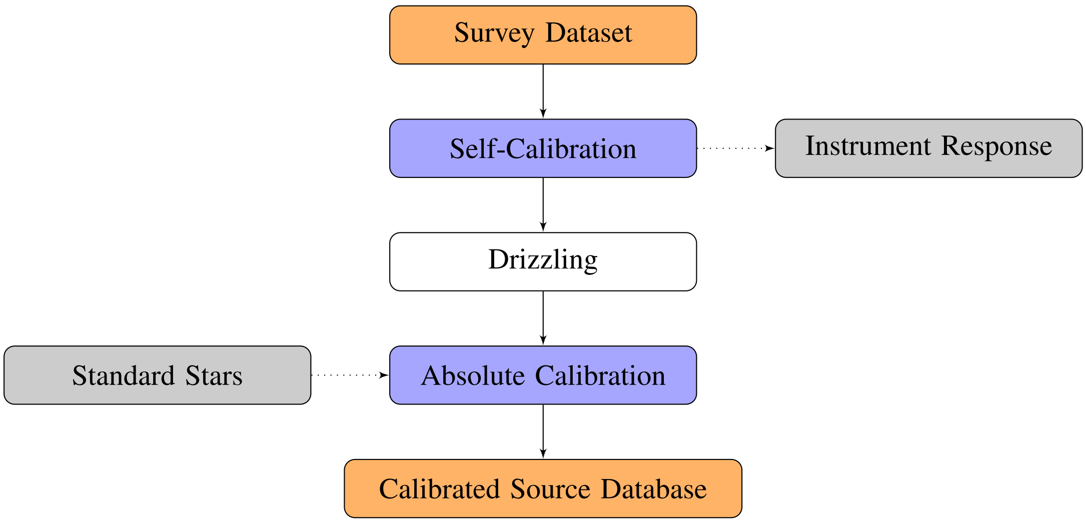


Figure 3.3: The proposed ground-based, full survey calibration of the NISP Photometric Channel's dataset.

#### Self-Calibration of the NISP Photometric Dataset

The survey nature of the Euclid mission will produce a vast amount of calibration information, which will be utilized to retrospectively improve the relative calibration of the NISP Photometric Channel's dataset. Once the survey is complete, copious numbers of sources – most of which can be presumed to be non-varying – will have been imaged at different times and in different parts of the focal plane. An improved *relative* photometric calibration is then obtained by requiring that the different measurements yield the same flux estimate. This method can not only improve the calibration of the dataset, but also help constrain the instrument response model. This procedure has been successfully applied to ground based surveys, such as the Sloan Digital Sky Survey [20]. The simulations presented in Chapter 4 show that this method is capable of accurately constraining the large-scale instrument response, such as (but not limited to) that arising from non-uniformities in the flat-field calibration source illumination. Chapter 4 presents the detailed simulations used to assess the performance of this self-calibration with the NISP Photometric dataset. These simulations have been used to optimize the Euclid Deep Field observing strategy for this kind of retrospective calibration. From this work, it is clear that this procedure will form an important part of the relative photometric calibration of the channel. After this step, the dataset will be drizzled to produce the deep images, on which the final source extraction can be performed.

#### Absolute Photometric Calibration

After the relative photometric accuracy has been retrospectively refined, the final step in the calibration procedure is to tie the measured counts to the physical photon fluxes entering the telescope. This *absolute* photometric calibration will be constrained through the observations of standard near-infrared objects. Figure 3.4 shows the location of the Hubble Space Telescope's (HTS's) four primary standard stars (squares) and a selection of the secondary standards (circles). Two of the HST primary calibrators fall within the Euclid Wide Survey ($|\text{galactic latitude}| \geq 30$), along with many of the secondary calibrators. I therefore propose that the absolute calibration of the photometric channel is constrained with these standard stars. If the instrument is able to meet the relative photometric error requirement, it will not be necessary to regularly observe the standard sources. It is therefore proposed that these sources are observed when they become available in the survey; no addition slews are therefore foreseen.

## 3.5 Required Instrument Calibration Modes[9]

To fulfill the calibration procedure introduced in the previous section, the NISP Photometric Channel requires three dedicated calibration operating modes from the instrument. They are summarized in Table 3.4 and detailed in the follow subsections.

### 3.5.1 Calibration Source Exposures

The NISP instrument requires an on-board calibration source for two purposes: (i) to produce flat-field maps and (ii) to monitor detector non-linearities[10]. High signal-to-noise calibration source exposures are required to generate flat-field maps that will be used to correct the small-scale ($< 50$ pixel) variation in pixel sensitivities. If a regular up-the-ramp sampling read mode is employed, with all the NDR frames returned to ground, then the detector non-linearities

[9] This work has been conducted in collaboration with L. Valenziano (Istituto Nazionale di Astrofisica – Italy), A. Ealet (Centre de Physique des Particules de Marseille – France) and J. Amiaux (Commissariat à l'Energie Atomique et aux Energies Alternatives – France) and has been incorporated into the *NISP Instrument Operation Concept Document* [21]

[10] This second purpose was identified by A. Ealet (Centre de Physique des Particules de Marseille – France) and G. Smadja (Institut de Physique Nucleaire de Lyon – France)

| Calibration Mode | Bands | Instrument State | Exposure Time | Frequency |
|---|---|---|---|---|
| **Flat-Field Exposure** | | | | |
| | – All | – Shutter Closed<br>– Calibration Source On<br>– Read Mode: regular up-the-ramp sampling | – 100 s | – $1^{st}$ 6 months: 2× month<br>– Subsequent months: 1× month |
| **Dark Exposure** | | | | |
| | – All | – Closed Shutter<br>– Read Mode: same as science exposures (Fowler 16) | – Same as Science Exposures | – $1^{st}$ 6 months: 2× month<br>– Subsequent months: 1× month |
| **Absolute Sources** | | | | |
| | – All | – Read Mode: fewer non-destructive samples (due to shorter exposure times) | – Source Dependent | – When available in Survey |

Table 3.4: A summary of the calibration modes that the instrument must be able to perform during the *nominal scientific operation* period of the mission. This does not include calibration modes required during the Calibration and Performance Verification (CPV) phase of the mission.

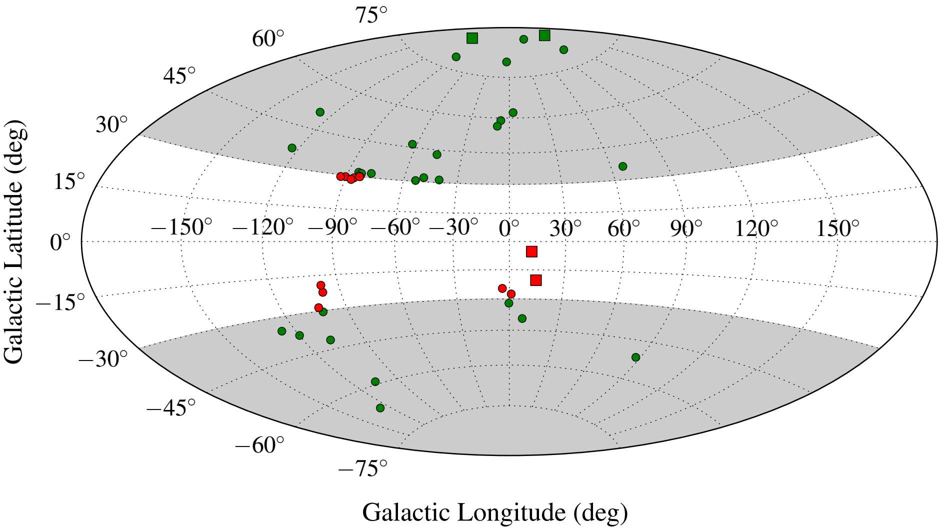


Figure 3.4: A plot showing the position of the Hubble Space Telescope (HST) primary standard stars (squares) and a subsample of the secondary standards (circles). The approximate sky area that will be covered with the Euclid Wide Survey (|galactic latitude| $\geq$ 30) is shown in gray. It is proposed that the standards within the survey area (green) are used as absolute calibrators for the NISP Photometric Channel.

could also be monitored with this exposure. For this monitoring, the calibration source would need to be temporarily stable. The baseline exposure time for the flat-field calibration source measurements is 100 s. The pixels should approach saturation (60,000 $e^-$) during this time, so that the linearity of the pixels over their full dynamic range can be quantified. These two properties allowed me to define a requirement on the calibration source: "*The calibration unit must provide an irradiance of between 550 to 750 $e^- s^{-1} pix^{-1}$ for all pixels*" [16]. The range of values in this requirement permits the calibration source illumination to have structure on large-scales. Since the pixel sensitivities are wavelength dependent, flat-field exposures are required in all photometry bands. To reduce the noise and remove cosmic ray events, a single flat-field map will be made up from multiple exposures of the calibration source. Individual exposures could be taken during the satellite slewing, and therefore the survey efficiency would not be reduced by performing these calibration exposures. During the first 6 months of observations, flat-field maps will be required twice a month. If the instrument proves to be sufficiently stable, this frequency could be reduced in subsequent months.

### 3.5.2 Dark Exposures

Dark exposures are required to subtract the detector dark current and the instrument's thermal contamination, which will be indistinguishable, from the science exposures. The NISP Instrument has a cold shutter in the filter wheel mechanism. Multiple images of this shutter, with the same exposure times as the science images, will be used to create dark frames that can be subtracted from the science frames. These exposures could also be potentially taken during the telescope slewing, and therefore they would not impinge on the scientific observations. The dark exposures will use the same readout mode as the science exposures. Multiple dark exposures are required to produce a dark map with sufficiently low noise and to remove cosmic ray events. During the first 6 months of observations, dark maps will be required twice a month. If the instrument proves to be sufficiently stable, this frequency could be reduced in subsequent months.

### 3.5.3 Exposures of Standard Stars

The absolute photometric calibration of the NISP Photometric Channel will be constrained with standard near-infrared sources (see Subsection 3.4.3). These sources are brighter than the channel's saturation limit (see Subsection 2.5) when observing in the nominal scientific mode. Therefore these standards will be observed with shorter exposure times and as a consequence the readout mode must be modified, as fewer Fowler samples can be taken. If the instrument is able to meet the relative photometric error requirement, it will not be necessary to regularly observe the standard stars. It is therefore proposed that these sources are observed when they become available in the survey; no addition slews are therefore foreseen. If a higher absolute photometric accuracy is required, then these standards could be regularly stepped across the focal plane.

## 3.6 Outlook

The calibration strategy defined in this chapter was included in the *NISP Calibration Plan* [16]. This document defines the baseline calibration procedure for the NISP Instrument and as such it is dictating the instrument design and operation. The high level calibration budget presented in Tables 3.2 and 3.3 must now be broken down by the NISP Instrument Team into requirements on individual subcomponents. The next two chapters concentrate on specific aspects of this calibration strategy, namely the self-calibration procedure (Chapter 4) and hardware development relating to an on-board flat-field calibration source (Chapter 5).

# Chapter 4

# Self-Calibration of the Near-Infrared Photometric Dataset

**Chapter Abstract:** This chapter presents results from an investigation into the potential retrospective self-calibration of the NISP Photometric Channel's dataset and, in particular, the effect of the survey strategy on the performance of this calibration. This technique fits an instrument response model that best explains the survey dataset, based on the multiple observations of (non-varying) sources at different focal plane positions. Four simple survey strategies are considered and I find that, with a correct redundancy built into the survey strategy, it will be possible to accurately constrain the relative instrument response of the NISP Photometric Channel, and therefore the relative calibration of the photometric dataset. The majority of the remaining post self-calibration errors are due to the limitations in the basis used to model the relative instrument response. I find that returning the same sources to very different focal plane positions is the key property of a survey strategy that is required for an accurate calibration. From the results of this study, I was able to define calibration requirements on the Euclid Deep Field survey strategy; it was optimized – subject also to other constraints – for this kind of retrospective self-calibration. Finally, I assess the performance of self-calibration with the resultant survey strategy and I conclude that this procedure will permit a precise relative calibration ($< 1.5$ %) of the NISP Photometric Channel.

With the latest generation of large-scale imaging surveys, the historic distinction between science data, which is used purely for science, and calibration data, which is used to constrain instrument parameters, is beginning to blur. With appropriate survey constraints, the Euclid science exposures will themselves contain a large amount of valuable calibration information. As introduced in Section 3.4.3, the retrospective self-calibration of the redundant data within the NISP Photometric Channel's dataset is envisaged as an important step in meeting the instrument's stringent relative photometric calibration requirement ([12], WL.2.1-20), which is dictated by the high level photometric redshift accuracy requirement ([12], WL.1-5). This method uses the multiple observations of (non-varying) sources at different focal plane positions to fit an instrument response model that best explains the dataset. As the mission's survey strategies are currently being defined, we are now in a unique position to optimize the mission for this kind of self-calibration.

The Euclid Mission will perform two surveys: (i) the main Wide Survey that will cover $\sim 15,000$ deg$^2$ and will be used for the primary science and (ii) a Deep Survey that will cover a $\sim 40$ deg$^2$ patch of sky many times for calibration and legacy science purposes [12]. The Wide Survey strategy is already defined: the sky will be tiled with small overlaps between adjacent pointings and with each pointing made up of four slightly offsetted dithers [15]. The Deep Field survey strategy, and even its position, is currently less constrained and it is here where requirements coming from calibration can – and will – be included in the observing strategy. A successful implementation of the self-calibration procedure could allow a calibration obtained from the Deep Survey observations to be transferred to the Wide Survey dataset.

This chapter details the end-to-end simulations constructed to compare the performance of this kind of self-calibration with different survey strategies. A complex position dependent instrument response model is constructed; the self-calibration procedure is then used to reconstruct this instrument response from the dataset obtained from mock observations performed according to a defined survey strategy. The simulations start with a realistic representation of the sky. A survey strategy is then implemented on this synthetic sky and measured count rates are recorded based on the complex instrument response model and appropriate measurement uncertainties. The resulting dataset is self-calibrated to recover the instrument response model and the sky source magnitudes, which can then be compared to the originals. The survey simulations and the self-calibration procedure are introduced in Sections 4.1 and 4.2 respectively. The metrics used to analyze the success of the self-calibration process are detailed in Section 4.3. Section 4.4 presents the performance of this procedure with four simple survey strategies. This analysis was used to define photometric calibration requirements on the Euclid Deep Field survey strategy; these are summarized in Section 4.4.3. In Section 4.5 the performance of the resulting Deep Survey strategy is assessed, which has been optimized by the Euclid Mission Survey Scientist[1] – subject also to other constraints – for this kind of self-calibration. The final part of this chapter deals with the sensitivity of the self-calibration procedure to different simulation parameters. Even though this work focuses on the NISP Photometric Channel's dataset, the conclusions are equally applicable to the Visible Imaging Channel.

## 4.1 Simulating the Imaging Dataset

An end-to-end simulation framework has been constructed that takes an observing strategy as an input, generates a realistic sky, performs the survey – with appropriate measurement uncer-

[1] R. Scaramella (Istituto Nazionale di Astrofisica – Italy)

tainties – and outputs a representative NISP Photometric dataset. The instrument's response is represented with a complex, position dependent model with both large- and small-scale variations; the purpose of the self-calibration procedure is to reconstruct this instrument response based on multiple observations of the same (non-varying) sources at different focal plane positions. The following sections detail the main methods and assumptions used in the end-to-end simulation of a NISP Photometric Channel's survey. Note that complex effects are included in the simulations that will not be precisely modeled at the analysis stage, in order to simulate the effects of unknown systematic errors.

### 4.1.1 Sky Simulation

The first step in the simulations is the generation of a representative sky, based on realistic object densities within the AB magnitude range $m_{\mathrm{min}} < m < m_{\mathrm{max}}$. The magnitude limits are chosen based on the NISP Photometric Channel's saturation limit and $10\sigma$ detection limit, $m_{\mathrm{min}} = 17$ mag (Section 2.5) and $m_{\mathrm{max}} = 22$ mag (Subsection 2.3.1) respectively . Sources are generated with random coordinates (uniformly distributed within the sky region being investigated) and with random magnitudes $m$ distributed according to

$$\log_{10} \frac{\mathrm{d}N}{\mathrm{d}m\,\mathrm{d}\Omega} = a + b\,m + c\,m^2 \quad , \tag{4.1}$$

where $\frac{\mathrm{d}N}{\mathrm{d}m\,\mathrm{d}\Omega}$ is the density of sources $N$ per unit magnitude $m$ and per unit solid angle $\Omega$, and $a$, $b$ and $c$ are model parameters. Even though the simulations make no distinction between galaxies and stars, the values of the parameters are found from fitting the Y-band galaxy populations reported in Windhorst et al. (2011) [22] only. These parameters were $a = -13.05$, $b = 1.25$ and $c = -0.02$, with similar values found for the J- and H-bands. The form of this distribution and the fitted parameters well reproduce the reported data. The source densities generated are therefore an underestimate of those available within the Euclid survey. The stellar densities have been intentionally excluded as these will vary across the Euclid survey, and the results from these simulations should be independent of the final position of the Deep Field. In contrast, the galaxy densities will be constant across the survey area. To reduce the computational load, only a fraction of the brightest sources are selected for the self-calibration procedure. In reality, all of the sources available within the dataset with multiple observations would be used. The source magnitude densities are summarized in Figure 4.1 and the simulated sky is shown in Figure 4.2. The source magnitudes $m$ are related to the source fluxes $s$ simply by: $m = 22.5 - 2.5\log_{10}(s)$, where the 22.5 puts the fluxes in units of nanomaggies (nmgy).

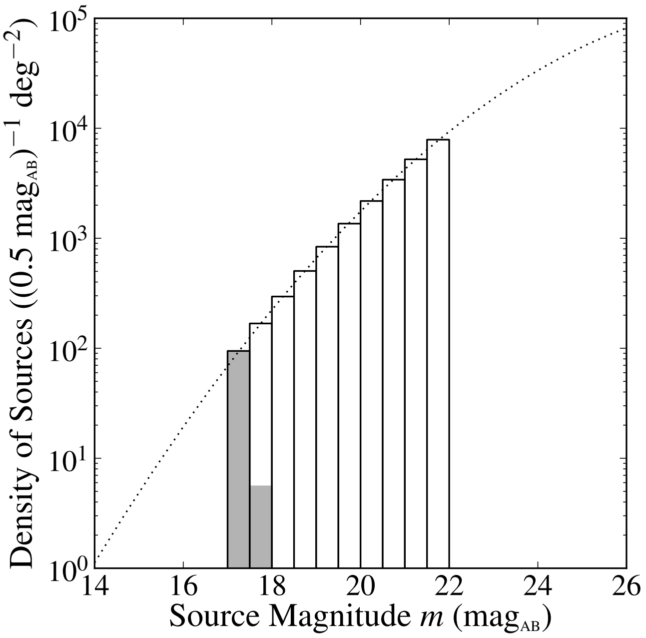


Figure 4.1: The density of sources used in the survey simulations. Dotted Line: a fit to the galaxy Y-band densities from Windhorst et al (2011) [22]. Histogram: the density of the simulated sources generated within the synthetic sky, with the filled area showing the bright sources selected for the self-calibration procedure.

### 4.1.2 Single Exposure

With a camera pointing $(\alpha, \beta)$ and camera orientation $\theta$ the sky is transformed into focal plane coordinates and all the sources falling within the instrument's field-of-view are found. The current size of the NISP Photometric Channel's field-of-view is used in the simulations: $0.76 \times 0.72$ deg$^2$ [23]. A typical exposure is depicted in Figure 4.2.

#### Measured Count Rates

In these simulations pixelated images are not produced; instead the true source fluxes $s_{\text{true}}$ are converted into measured count rates $c$ with an instrument response model $f_{\text{true}}$ and a measurement noise model.

For a measurement $i$ the count rate $c_i$ recorded from a source $k$ depends on the *true* instrument response $f_{\text{true}}(\vec{x}_i|\vec{q}_{\text{true}})$, which is a function of focal plane position $\vec{x}_i$, and the source's true flux $s_{k,\text{true}}$

$$c_i = f_{\text{true}}(\vec{x}_i|\vec{q}_{\text{true}})\, s_{k,\text{true}} + e_i \quad ,$$

where $\vec{q}_{\text{true}}$ are the parameters defining the *true* instrument response, and $e_i$ is a noise contribution drawn from the Normal Distribution $N(e|0, \sigma_{\text{true}}{}^2)$.

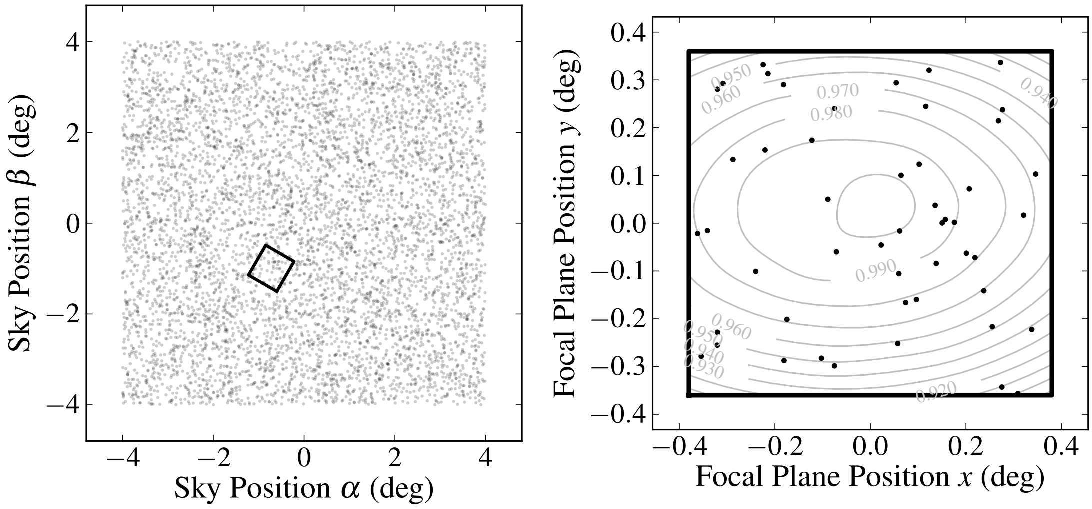


Figure 4.2: A single exposure of the synthetic sky. Left: A plot of the bright sources within the synthetic sky used in the self-calibration procedure. Right: The resultant distribution of the sources on the instrument's focal plane. The *true* instrument model $f_{\text{true}}(\vec{x}_i|\vec{q}_{\text{true}})$ is shown as contours.

### Noise Model

To construct the noise model, the NISP exposures are assumed to be background limited and that, for systematic reasons, there is an upper limit on the signal-to-noise ratio of 500 for bright sources. The noise model is complicated further by applying an extra term $\varepsilon_i$ to the count rates' uncertainty variance, which is intentionally not taken into account in the analysis in order to simulate systematic problems with the instrument noise model. The *true* noise model is therefore

$$\sigma_{i,\text{true}}^2 = (1+\varepsilon_i)\,\alpha^2 + \eta^2\,[f_{\text{true}}(\vec{x}_i|\vec{q}_{\text{true}})\,s_{k,\text{true}}]^2 \quad , \tag{4.2}$$

where $\alpha$ and $\eta$ are both constants and $\varepsilon_i$ is a random number, in the range [0.0, $\varepsilon_{max}$), generated for each measurement $i$. The NISP Photometric Channel's 10$\sigma$ detection limit ($m = 22$ mag) and the 500 limit on the signal-to-noise ratio are used to set $\alpha = 0.1585$ and $\eta = 0.0017$. The $\varepsilon_i$ contribution is not taken into account in the self-calibration procedure and therefore the uncertainty variances on the count rates are assumed to be

$$\sigma_i^2 = \alpha^2 + \eta^2\,c_i^2$$

during the analysis stage. An example of the assumed uncertainty variances compared to the true uncertainty variances is shown in Figure 4.3.

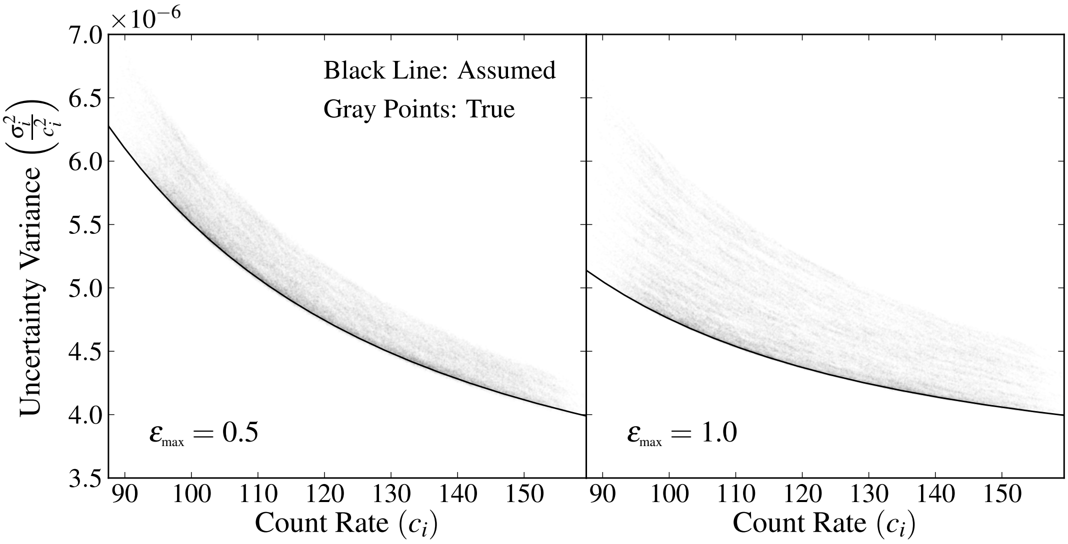


Figure 4.3: A comparison of the *true* and *assumed* measurement uncertainty variances for the sources included in the self-calibration procedure. As can be seen in Figure 4.1, only the brightest sources within the synthetic sky are used in the self-calibration procedure and as a result the uncertainty variances in the simulation are small. In the simulations the assumed and actual values differ to simulate systematic problems with the instrument noise model. In both panels, the assumed measurement uncertainty variances are shown in black and the true measurement uncertainty variances, with the additional $\varepsilon_{max}$ contribution, are shown as gray points. The left panel corresponds to a $\varepsilon_{max} = 0.5$ and the right to a $\varepsilon_{max} = 1.0$. Since the additional contribution is formed with a random number in the range [0.0, $\varepsilon_{max}$), an increase in $\varepsilon_{max}$ results in a greater spread of measurement uncertainty variances above the assumed line.

### True Instrument Response Model

A complex instrument response model $f_{\text{true}}(\vec{x}_i|\vec{q}_{\text{true}})$ has been constructed from a superposition of large and small-scale variations:

$$f_{\text{true}}(\vec{x}_i|\vec{q}_{\text{true},1...260}) = f_{\text{large}}(\vec{x}_i|\vec{q}_{\text{true},1...6}) + f_{\text{small}}(\vec{x}_i|\vec{q}_{\text{true},7...260}) \quad ,$$

where $\vec{x}_i = (x_i, y_i)$ is the focal plane position that the $k$th source falls at during the $i^{\text{th}}$ measurement and $\vec{q}_{\text{true}}$ are the parameters defining the instrument response model. The large-scale instrument response $f_{\text{large}}(\vec{x}_i|\vec{q}_{\text{true},1...6})$, such as the residual from a flat-field calibration source correction, is modeled as a second order polynomial:

$$f_{\text{large}}(\vec{x}_i|\vec{q}_{\text{true},1...6}) = q_{\text{true},1} + q_{\text{true},2}\,x_i + q_{\text{true},3}\,y_i + q_{\text{true},4}\,x_i^2 + q_{\text{true},5}\,x_i\,y_i + q_{\text{true},6}\,y_i^2 \quad .$$

The small-scale instrument response, which is constructed from sine and cosine contributions, is superimposed on this large-scale instrument response. The small-scale instrument response

$f_{\text{small}}(\vec{x}_i|\vec{q}_{\text{true},7\ldots260})$ is modeled as

$$\begin{aligned} f_{\text{small}}(\vec{x}_i|\vec{q}_{\text{true},7\ldots260}) &= \sum_{a=0}^{6}\sum_{b=0}^{a}\left[q_{\text{true},7+4b}\cos(k_x x_i) + q_{\text{true},8+4b}\sin(k_x x_i)\right] \\ &\qquad \times \left[q_{\text{true},9+4b}\cos(k_y y_i) + q_{\text{true},10+4b}\sin(k_y y_i)\right] \quad , \end{aligned}$$

where

$$\begin{aligned} k_x &= \frac{a\,\pi}{X} \quad , \\ k_y &= \frac{b\,\pi}{Y} \quad , \end{aligned}$$

with the physical focal plane dimensions $X$ and $Y$. In total, the instrument response model is parameterized with 260 parameters; an example can be seen earlier in Figure 4.3. As discussed in Subsection 3.2.1, I defined a (very) small-scale ($< 50$ pixel) smoothness requirement on the illumination from the NISP Instrument's Flat-Field Calibration Source. Therefore, in these simulations it is assumed that the NISP Flat-Field Calibration Source accounts for the truly tiny, pixel-to-pixel sensitivity variations in the instrument response. As a result of this I do not need to consider pixelized images; instead I work on catalogs with realistic measurement uncertainties. My final assumption in these simulations is that the instrument response is temporally stable.

### 4.1.3 Full Survey Simulation

The single exposure procedure is applied for every pointing specified in the survey strategy being investigated. The resultant source measurement dataset is then self-calibrated to fit for the *true* instrument response and the *true* source fluxes. The tunable parameters in these simulations are summarized in Table 4.1.

| Parameter | Fiducial Value |
|---|---|
| **Sky Parameters** | |
| Source Density – Eqn. 4.1 ($\deg^{-2}$) | $a = -13.05, b = 1.25, c = -0.02$ |
| Survey Area ($\deg^2$) | $8 \times 8$ |
| **Survey Parameters** | |
| Source Density ($\deg^{-2}$) | $d = 100$ |
| **Instrument Parameters** | |
| Saturation Limit (mag) | $m_{\mathrm{min}} = 17$ |
| $10\sigma$ Detection Limit (mag) | $m_{\mathrm{max}} = 22$ |
| Field-of-View ($\deg^2$) | $0.76 \times 0.72$ |
| Noise Model – Eqn. 4.2 | $\alpha = 0.1585$, $\eta = 0.0017$, $\varepsilon_{\mathrm{max}} = 1.0$ |
| **Self-Calibration Parameters** | |
| Fitted Instrument Response Model | $8^{\mathrm{th}}$ order polynomial |

Table 4.1: A summary of the tuneable parameters in the self-calibration simulations and their fiducial values.

## 4.2 Calibrating the Dataset

The dataset generated in the survey simulation is self-calibrated in order to recover the instrument response model and the source fluxes. This self-calibration procedure has been successfully applied to ground based imaging surveys, such as the Sloan Digital Sky Survey [24]. This iterative procedure comprises two steps: (1) a refinement of the source flux estimates based on the latest instrument response model and (2) a refinement of the instrument response model based on the updated source flux estimates. These steps are iterated until the system converges, or until it is clear that the system will not converge. There is a degeneracy in the problem, as both the true instrument response and the true source magnitudes are unknown. It is therefore only possible to calibrate the *relative* instrument response and the *relative* source fluxes. It is not possible to know, for example, if the sources are all fainter or if the instrument response is uniformly lower. As detailed in the calibration strategy (Subsection 3.4.3), the absolute instrument response will be constrained with well characterized standard stars and therefore this degeneracy will be broken. To account for this degeneracy in the simulations, the fitted instrument response is normalized with respect to the true instrument response at each iteration step.

### 4.2.1 Fitted Measurement Model

To complicate the simulations, the self-calibration procedure is used to fit a model that is *incomplete* in two ways. Firstly, the *fitted* instrument response is modeled as an eighth order polynomial, and not the second order polynomial superimposed with sine and cosine contributions used to model the *true* instrument response. Secondly, the assumed measurement uncertainty variances do not include the additional random measurement error $\varepsilon_i$ introduced in Subsection 4.1.2. The incomplete measurement model is

$$c_i = f(\vec{x}_i|\vec{q})\, s_k + e_i \quad ,$$

where $c_i$ is the recorded count rate, $f(\vec{x}_i|\vec{q})$ is the fitted instrument response model at a focal plane position $\vec{x}_i$, $\vec{q}$ is a vector parameterizing the eighth order polynomial instrument response model, $s_k$ is the model source flux estimate and the error $e_i$ is drawn from the Normal Distribution $N(e|0, {\sigma_i}^2)$, such that

$$\sigma_i^2 = \alpha^2 + \eta^2\, c_i^2 \quad ,$$

where $\alpha$ and $\eta$ are the parameters set by the instruments $10\sigma$ and saturation limits. The $\varepsilon_i$ error contribution defined in Subsection 4.1.2 is intentionally not included in order to simulate systematic problems with the instrument noise model.

### 4.2.2 Step 1: Source Flux Refinement

The sources are considered individually in the first step of the self-calibration procedure; their flux estimates are refined based on the latest fitted instrument response parameters $\vec{q}$. An error function $\chi_k^2$ for all the measurements $i$ of a source $k$ ($i \in \mathscr{O}(k)$) is constructed:

$$\chi_k^2 = \sum_{i \in \mathscr{O}(k)} \frac{(c_i - f_i(\vec{x}_i|\vec{q})\, s_k)^2}{{\sigma_i}^2} \quad ,$$

where $c_i$ are the measured count rates, $f(\vec{x}_i|\vec{q})$ is the fitted instrument response model at a focal plane position $\vec{x}_i$ and $\sigma_i$ is the assumed noise model. A new estimate of the model source flux $s'_k$ is then found by minimizing the error function with respect to the old model source flux $s_k$:

$$\frac{d\chi_k^2}{ds_k} = \sum_{i \in \mathscr{O}(k)} \frac{-2 f_i(\vec{x}_i|\vec{q})\, (c_i - f_i(\vec{x}_i|\vec{q})\, s'_k)}{{\sigma_i}^2} = 0 \quad ,$$

$$s'_k \leftarrow \left[\sum_{i \in \mathscr{O}(k)} \frac{f_i(\vec{x}_i|\vec{q})^2}{{\sigma_i}^2}\right]^{-1} \left[\sum_{i \in \mathscr{O}(k)} \frac{f_i(\vec{x}_i|\vec{q})\, c_i}{{\sigma_i}^2}\right] \quad .$$

The standard uncertainty variance on the new source flux estimate $s'_k$ is given by

$$\sigma_k'^2 = \left[\sum_{i \in \mathscr{O}(k)} \frac{f_i(\vec{x}_i|\vec{q})^2}{{\sigma_i}^2}\right] \quad .$$

### 4.2.3 Step 2: Instrument Response Refinement

The instrument response parameters can now be refined with the latest source flux estimates. A error function for all the measurements of all the sources is constructed

$$\chi^2 = \sum_k \chi_k'^2 \quad ,$$

where

$$\chi_k'^2 = \sum_{i \in \mathscr{O}(k)} \frac{(c_i - f_i(\vec{x}_i|\vec{q})\, s_k')^2}{{\sigma_i}^2} \quad .$$

Recall that the fitted instrument response $f_i(\vec{x}_i|\vec{q})$ is modeled as an eight order polynomial. This can be expressed as

$$f_i(\vec{x}_i|\vec{q}) = \sum_{l=1}^{L} q_l\, g_l(\vec{x}_i) \quad ,$$

where $L = 45$ in this case. The total error function $\chi^2$ can be rewritten as

$$\chi^2 = \sum_k \sum_{i \in \mathscr{O}(k)} \frac{(c_i - s_k' \sum_{l=1}^{L} q_l g_l(\vec{x}_i))^2}{{\sigma_i}^2} \quad .$$

To refine the instrument response model fit, this error function is minimized with respect to the instrument response model parameters $q_l$

$$\frac{d\chi^2}{dq_l} = \sum_k \sum_{i \in \mathscr{O}(k)} \frac{-2 g_l(\vec{x}_i) s_k' (c_i - s_k' \sum_{l'=1}^{L'} q_{l'}' g_{l'}(\vec{x}_i))}{{\sigma_i}^2} = 0 \quad ,$$

$$\sum_k \sum_{i \in \mathscr{O}(k)} \frac{g_l(\vec{x}_i) s_k' c_i}{{\sigma_i}^2} = \sum_k \sum_{i \in \mathscr{O}(k)} \frac{g_l(\vec{x}_i) s_k'^2 \sum_{l'=1}^{L'} q_{l'}' g_{l'}(\vec{x}_i)}{{\sigma_i}^2} \quad .$$

It is now simpler to proceed in matrix notation. The following substitutions can be made

$$b_l = \sum_k \sum_{i \in \mathscr{O}(k)} \frac{g_l(\vec{x}_i) s_k' c_i}{\sigma_i^2} \quad , \tag{4.3}$$

$$G_{ll'} = \sum_k \sum_{i \in \mathscr{O}(k)} \frac{{s'}_k^2}{\sigma_i^2} g_l(x_i) g_{l'}(x_i) \quad . \tag{4.4}$$

The matrix equation is then

$$\vec{b} = G \cdot \vec{q}' \quad .$$

The refined instrument response parameters are then found by

$$\vec{q}' \leftarrow G^{-1} \cdot \vec{b} \quad .$$

These two steps are iterated until the solution converges to a final fit of the instrument response $f_{\mathrm{fit}}(\vec{x}|\vec{q_{\mathrm{fit}}})$ and the source fluxes $s_{k,\mathrm{fit}}$, or until it is clear that a solution will not be found.

## 4.3 Metrics

To assess the performance of the self-calibration procedure with different survey strategies, it is necessary to quantify the quality of the final fitted solution. To do this three quantities are defined. The first is the root-mean-squared (RMS) error $S_{\mathrm{RMS}}$ in the final fitted source fluxes $s_{k,\mathrm{fit}}$ compared to the true source fluxes $s_{k,\mathrm{true}}$ for all the $K$ sources:

$$S_{\mathrm{RMS}} = \sqrt{\frac{1}{K}\sum_{k}^{K}\left(\frac{s_{k,\mathrm{fit}} - s_{k,\mathrm{true}}}{s_{k,\mathrm{true}}}\right)^2} \quad . \tag{4.5}$$

The other two metrics, called "badnesses", are defined as the RMS error between the final fitted instrument response and a reference instrument response sampled on a regular $500 \times 500$ grid across the focal plane. For the "True Badness" $B_{\mathrm{true}}$, the *fitted* instrument response $f_{\mathrm{fit}}(\vec{x}|\vec{q_{\mathrm{fit}}})$ is compared to the *true* instrument response $f_{\mathrm{true}}(\vec{x}|\vec{q_{\mathrm{true}}})$ at the $J$ sample points

$$B_{\mathrm{true}} = \sqrt{\frac{1}{J}\sum_{j}^{J}\left(\frac{f_{\mathrm{fit}}(\vec{x}_j|\vec{q_{\mathrm{fit}}}) - f_{\mathrm{true}}(\vec{x}_j|\vec{q_{\mathrm{true}}})}{f_{\mathrm{true}}(\vec{x}_j|\vec{q_{\mathrm{true}}})}\right)^2} \quad . \tag{4.6}$$

The "Best-in-Basis Badness" $B_{\mathrm{best}}$ compares the *fitted* instrument response $f_{\mathrm{fit}}(\vec{x}_j|\vec{q_{\mathrm{fit}}})$ to the *best instrument response fit possible* $f_{\mathrm{best}}(\vec{x}_j|\vec{q_{\mathrm{best}}})$ with the basis used to describe the fitted model (in this case an eight order polynomial) at the $J$ sample points

$$B_{\mathrm{best}} = \sqrt{\frac{1}{J}\sum_{j}^{J}\left(\frac{f_{\mathrm{fit}}(\vec{x}_j|\vec{q_{\mathrm{fit}}}) - f_{\mathrm{best}}(\vec{x}_j|\vec{q_{\mathrm{best}}})}{f_{\mathrm{best}}(\vec{x}_j|\vec{q_{\mathrm{best}}})}\right)^2} \quad . \tag{4.7}$$

The badnesses provide a more complete description of the self-calibration performance than the RMS error on the fitted sources' fluxes, especially in the case – such as Euclid – in which repeat observations of a deep field will be used to calibrate a wide survey. The RMS source error applies only to the bright sources within the synthetic sky selected for the self-calibration procedure.

| Survey Name | Pointing Center | Orientation | Total Pointings |
|---|---|---|---|
| A | Uniform Grid ($12 \times 12$) | $0°$ | 1728 |
| B | Uniform Grid ($12 \times 12$) | Each Pass: $\theta + 30°$ | 1728 |
| C | Pass 1: Uniform Grid ($12 \times 12$) | | 1720 |
| | Pass 2: Uniform Grid ($13 \times 11$) | $0°$ | |
| | Pass 3: Uniform Grid ($11 \times 13$) | | |
| D | Quasi-Random | Random | 1728 |

Table 4.2: A summary of the four simple survey strategies investigated.

## 4.4 Simple Survey Strategies

In this section four simple but very different survey strategies are considered. The end-to-end simulation chain introduced in Sections 4.1 and 4.2 has been used to assess the performance of the self-calibration procedure with these surveys.

### 4.4.1 Survey Description

The four survey strategies, which all cover the same patch of sky, are labeled A to D. They are summarized in Table 4.2 and are shown in Figure 4.4 (at the end of the chapter). Strategy A is the simplest strategy; the field is regularly tiled with small overlaps between adjacent pointings ($\sim 5$ % and $\sim 8$ % in the camera pointing directions $\alpha$ and $\beta$ respectively). The pointings in the 12 passes over the same field are exactly aligned. Survey B is the same as A, but with each pass over the field the orientation of the telescope is rotated by 30°. Survey C is more complex. The first pass over the field is the same as in Survey A, with $12 \times 12$ pointings. In the next pass, one of the pointings in the $\alpha$ direction is removed and one is added in the $\beta$, so the resultant pointing grid is $13 \times 11$. In the third pass over the field this change is reversed and the field is measured on a $11 \times 13$ grid. These three passes are then repeated four times. The pointing positions in Survey D are quasi-random: the pointings are the same as with Survey A, but each has a random offset within [-0.35,0.35) deg applied in both the $\alpha$ and $\beta$ directions. By fixing the pointings within these 0.7 deg $\times$ 0.7 deg boxes, I ensure that the quasi random strategy has a uniform coverage of the field. The orientations of the pointings in Survey D are completely random.

### 4.4.2 Self-Calibration Performance

These four simple survey strategies were ran through the survey simulation chain presented in Section 4.1 to produce representative photometry datasets. These were then self-calibrated using the method introduced in Section 4.2. The iterative self-calibration procedure converges to a final fitted solution for the Survey B, C and D datasets. With the Survey A dataset it does not converge, even when the system is started close to the optimum fit. The fitted instrument response solutions for the Survey D, B and A datasets are shown in Figures 4.5, 4.6 and 4.7

respectively. The corresponding plot for the Survey C dataset has been omitted, due to its similarity to the Survey D dataset result. In these plots the final fitted instrument response $f_{\text{fit}}(\vec{x}_j|\vec{q_{\text{fit}}})$ is compared to the true instrument response $f_{\text{true}}(\vec{x}|\vec{q_{\text{true}}})$ and to the best possible instrument response fit with the basis used $f_{\text{best}}(\vec{x}_j|\vec{q_{\text{best}}})$ ("best-in-basis"). The accuracy of the final fitted solutions are summarized, with the metrics introduced in Section 4.3, for each of the Survey strategies in Table 4.3.

The difference between the success of the self-calibration procedure with these four survey strategies is clear: with Surveys A no solution can be obtained, but with the Surveys B, C and D datasets the self-calibration procedure converges close to the correct solution. With the Survey C and D datasets the instrument response can be accurately fitted, close to the best fit possible with the basis used. The majority of the remaining errors in the fit come from the limitations of the basis used in the instrument response model. The calibration procedure with the Survey B dataset requires more iteration steps (4270) to converge to a final solution, and is less accurate than those found with the Survey C and D datasets, which require 28 and 10 iteration steps respectively.

The results from this investigation into simple survey strategies can be used to draw conclusions about the properties of surveys that make them good, or bad, for retrospective self-calibration. From these examples, I conclude that regular survey strategies with little overlap between adjacent pointings (Survey A) – such as the Euclid Wide Survey – do not allow for the resulting dataset to be self-calibrated effectively. It is therefore necessary to depart from the standard, regularly tiled observing strategies in the Euclid Deep Field. The two best survey strategies (C, D) both return the same sources to very different focal plane positions, and this is the key property which makes their datasets good for self-calibration. By doing so, many different focal plane positions are connected to each other with observations of the same source. This result must be considered when the Deep Field survey strategy is defined and as such I have applied calibration requirements that capture this on the strategy (see Subsection 4.4.3). In addition, I also conclude that if the correct redundancy is built into the survey strategy, the self-calibration procedure will be able to accurately constrain the relative instrument response, and therefore the Deep Field relative photometric calibration could be transfered effectively to the Wide Survey. The majority of the remaining errors will come from the limitations of the basis used to fit the instrument response model.

| Survey Name | Iterations | Source Error $S_{\mathrm{RMS}}$ (%) | True Badness $B_{\mathrm{true}}$ (%) | Best-in-Basis Badness $B_{\mathrm{best}}$ (%) |
|---|---|---|---|---|
| A | 22188* | 2.1721 | 2.2681 | 2.2674 |
| B | 4070 | 0.0777 | 0.0657 | 0.0254 |
| C | 23 | 0.0753 | 0.0613 | 0.0074 |
| D | 10 | 0.0707 | 0.0611 | 0.0049 |

Table 4.3: A summary of the quality of the final fit from the self-calibration procedure with the four simple survey strategies summarized in Table 4.2. The self-calibration procedure was run with only the brightest sources within the survey area (see Figure 4.1); the source error $S_{\mathrm{RMS}}$ corresponds to the measurements of these sources only and not all those within the survey. *Did not converge.

### 4.4.3 Calibration Requirements on the Deep Field

Based on the results from these simulations, I was able to define calibration requirements on the Euclid Deep Field survey strategy, which was optimized – subject also to other constraints – for self-calibration. As discussed in Subsection 4.4.2, the key element of a survey strategy that is required for effective self-calibration is to return the same sources to very different focal plane positions. Ideally, the Euclid Deep Field survey strategy would be quasi random, like Survey D. Unfortunately this is not possible, as there are a number of constraints coming from other aspects of the mission. The high precision visible imager demands a very strict thermal control of the satellite and, as such, the telescope's angle to the Sun (its Solar Aspect Angle – SAA) is required to depart only slightly from 90°. The Deep Field will also be used by the NISP Spectroscopic Channel to calibrate the Wide Survey and to do so the same dithering and observation mode must be employed. In addition, to minimize the time lost to slewing the satellite, the Deep Field will be completely covered per visit. Taking these restrictions into account, I defined the three calibration requirements shown in Table 4.4 on the Deep Field observing strategy. These requirements apply to a whole Deep Field visit and not to the individual observations. Requirements R-NP-CAL-F-004(b) and R-NP-CAL-F-004(c) ensure that the same sources are returned to very different focal plane positions. Requirement R-NP-CAL-F-004(a) deals with the temporal variability of the instrument response. This has not been considered in this analysis, although the instrument's response should be temporarily stable. For example, the near-infrared channel of the Wide Field Camera 3 (WFC3/IR) on the Hubble Space Telescope, which occupies a less stable thermal environment around the Earth than Euclid will at the second Lagrange point, was found to be highly temporally stable ($>$ 99.5 %) over 320 days in the first year of science operations [25]. Nevertheless, a requirement on the cadence of the Deep Field observations is applied so that long term drifts in the instrument response can be monitored and self-calibrated out. Temporal variations in the instrument response can be accommodated in the self-calibration procedure by simply changing $f(\vec{x}_i|\vec{q}) \rightarrow f(\vec{x}_i, t|\vec{q})$ (see Section 4.2). The rest of the derivation remains identical, although the parameterization of the

| ID [15] | Description | Requirement |
|---|---|---|
| R-NP-CAL-F-004(a) | Cadence | $<1$ month |
| R-NP-CAL-F-004(b) | Number of Equally Spaced Rotation Angles | $\geq 6$ |
| R-NP-CAL-F-004(c) | Offset between Field Centers | Random Shift in $[0.25, 0.75)$ $\times$ Focal Plane Width |

Table 4.4: The requirements applied to the Euclid Deep Field observing strategy coming from the self-calibration simulations. These requirements apply to the Deep Field visits, and not the individual exposures.

model instrument response must be modified to account for temporal changes.

## 4.5 The Euclid Deep Field

A possible implementation of the Deep Field survey strategy, defined by the Euclid Survey Scientist[2], is shown in Figure 4.8. Per Deep Field visit, the survey area is tiled into 41 pointings, each consisting of the four slightly shifted dithered exposures. The pointings are all shifted according to requirement R-NP-CAL-F-004(c) and the telescope orientation is rotated by 30° per visit. It is also possible to meet the cadence requirement R-NP-CAL-F-004(a), if the Deep Fields are positioned at the north or south ecliptic pole (the only places on the sky that can be regularly observed with a $\sim 90^\circ$ solar aspect angle).

This Deep Field survey strategy has been run through the end-to-end simulations and the resultant dataset has been self-calibrated. The instrument response fit is shown in Figure 4.9. With this survey, the self-calibration procedure performs well and converges after 34 iterations to a solution with a true badness $B_{\text{true}} = 0.0611$ %, a best-in-basis badness $B_{\text{best}} = 0.0048$ % and source error $S_{\text{RMS}} = 0.0539$ %. I therefore conclude that a Deep Field survey strategy of this type will allow the resultant dataset to be well self-calibrated. The instrument response model is accurately fitted and, again, the majority of the remaining errors are due to the limitation in the basis used to model the instrument response. I therefore also conclude that with an observing strategy of this type the Deep Field calibration could be effectively transferred to the Wide Survey.

## 4.6 The Impact of Source Density Variations

In the simulations present in the previous sections, the self-calibration procedure has been performed with only a small subset of the brightest sources available within the synthetic sky. In this section, the impact of increasing the source density on the quality of the final fitted solution is investigated. To do this, the self-calibration procedure is run – with the Deep Field survey

[2] R. Scaramella (Istituto Nazionale di Astrofisica – Italy)

strategy presented in Section 4.5 – with an increasing fraction of the available sources within the synthetic sky, for the range of source densities from $d = 1$ to $d = 1000\ \mathrm{deg}^{-2}$. Figure 4.10 shows the quality of the final fitted solution in this range, with the three performance metrics (see Section 4.3): the true badness $B_{\mathrm{true}}$, the best-in-basis badness $B_{\mathrm{best}}$ and the RMS source error $S_{\mathrm{RMS}}$. These results are plotted for two different values of $\varepsilon_{\mathrm{max}}$, the quantity that dictates the difference between the assumed and the true measurement uncertainties (see Subsection 4.1.2): $\varepsilon_{\mathrm{max}} = 1.0$ and $\varepsilon_{\mathrm{max}} = 10.0$.

Even though the true badness $B_{\mathrm{true}}$ is higher in the $\varepsilon_{\mathrm{max}} = 10.0$ case than in the $\varepsilon_{\mathrm{max}} = 1.0$ case at lower source densities, they both quickly tend to a constant value of $B_{\mathrm{true}} \sim 0.06$ %. That said, in both cases increasing the source density $d$ above $\sim 10\ \mathrm{deg}^{-2}$ does not significantly increase the accuracy of the instrument response model fit. This is in contrast to the best-in-basis badness $B_{\mathrm{best}}$, which continues to fall in both cases at a rate of $d^{-2}$, before beginning to plateau at a source density of $d \sim 100\ \mathrm{deg}^{-2}$. From the difference in the behavior of the true and best-in-basis badnesses – in both cases – I conclude that with a sufficient source density, the self-calibration procedure's accuracy is limited by the basis used to fit the instrument response model. Increasing the source density further, and therefore the amount of calibration information within the dataset, does not significantly increase the quality of the final fit, even though the system tends closer to the best fit possible with the basis used to model the instrument response.

From Figure 4.10 (right), it can be seen that the $\varepsilon_{\mathrm{max}} = 10.0$ case has higher RMS source errors $S_{\mathrm{RMS}}$ than the $\varepsilon_{\mathrm{max}} = 1.0$ for all values of the source density. This is to be expected as the $\varepsilon_{\mathrm{max}}$ quantity defines the level of additional noise introduced to the measurements. At the lower source densities the RMS source error $S_{\mathrm{RMS}}$ in both cases remains roughly constant. Towards the higher densities, both of the trends turn up. This, at first, seems rather counter intuitive as the quality of the instrument response remains constant in this regime. This feature is due to the way sources are selected for the self-calibration procedure. In the simulations, only the brightest sources – with the highest signal-to-noise measurements – are selected in the synthetic sky for the self-calibration procedure. At the higher source densities, it is necessary to select fainter sources, with lower signal-to-noise measurements, from the synthetic sky for the self-calibration procedure. Since the quality of the final instrument response is not improved significantly with these sources, the resultant RMS source error $S_{\mathrm{RMS}}$ is therefore increased. This is confirmed with Figure 4.11. Here the self-calibration performance is again plotted against source density for two cases: (i) where the number of bright sources within the synthetic sky is based on values reported in the literature (Subsection 4.1.1) and (ii) where the number of bright sources within the synthetic sky is increased ten-fold. Case (i) is the same as the previous simulations presented in this chapter. By artificially increasing the number of bright sources available for the self-calibration procedure in case (ii), the system can fit the solution with more brighter, higher signal-to-noise source measurements. In the RMS source error plot shown in Figure 4.11 (right), this can be seen as a difference in the behavior at higher source densities. Again the upward turn can be seen for case (i) as fainter sources must be included in the self-calibration procedure to achieve the specified density. This is not the case with (ii), where there are still sufficient bright sources within the sky. For both of these cases the badnesses – and therefore the instrument response fit – improve comparably at low source densities. In case (ii), there is no plateauing of the best-in-basis badness $B_{\text{best}}$, suggesting that this plateauing with case (i) is a result of the inclusion of further low signal-to-noise sources. In short, the inclusion of additional faint sources in the self-calibration procedure does not significantly improve the quality of the self-calibration procedure, even though the multiple measurements of these do contain information about the relative instrument response.

In all of the plots, the random nature of the sky survey generation can be seen as a scatter in the results, particularly in the low source density regime, where the system is more sensitive to the position and magnitude of the fewer sources.

## 4.7 Discussion

This work has shown that – as long a certain survey constraints are met – the retrospective self-calibration of the Euclid Deep Survey dataset could accurately constrain NISP Photometric Channel's relative photometric response. For the self-calibration procedure to accurately fit the true solution, the dataset must not only have redundancy, but a specific type of redundancy: I find that the key requirement on the survey strategy coming from this self-calibration procedure is to return the same sources to very different focal plane positions. This is a property that the Euclid Wide Survey does not have. Based on the results of this work, I have been able to define calibration requirements on the Euclid Deep Field survey. I conclude that the resultant survey strategy would allow effective self-calibration, with the majority of the remaining errors coming from limitations in the basis used to model the relative instrument response. Based on the results of the simulations with the proposed Deep Field survey strategy, I conclude that – as long as it can be accurately parameterized – the self-calibration procedure coupled with a very small-scale correction with the on-board calibration source could constrain the relative instrument response sufficiently to allow the $< 1.5$ % relative photometric error requirement to be met (see Section 3.1). The final (and rather unexpected) conclusion from this work is that the inclusion of fainter, lower signal-to-noise sources does not significantly improve the quality of the instrument response fit, despite the fact that the multiple observations of these at different focal plane positions do contain information about the relative instrument response.

In this work, I have used the self-calibration procedure to fit for a *scalar* quantity: the relative instrument response. An additional interesting topic to investigate would be using this procedure to fit for *vector* or *tensor* quantities, such as the instrument's optical distortion. I suspect that the survey properties that are advantageous for the instrument response fit will not be the same as those for fitting an optical distortion model. More specifically, I expect rotations to be more significant in this case.

I finally note, that these simulations have been performed solely on catalogs and not real images. Although the main conclusions will be unaffected – as I use a realistic measurement uncertainty model – this work will need to be reproduced with realistic images and source extraction in the full end-to-end Euclid simulations.

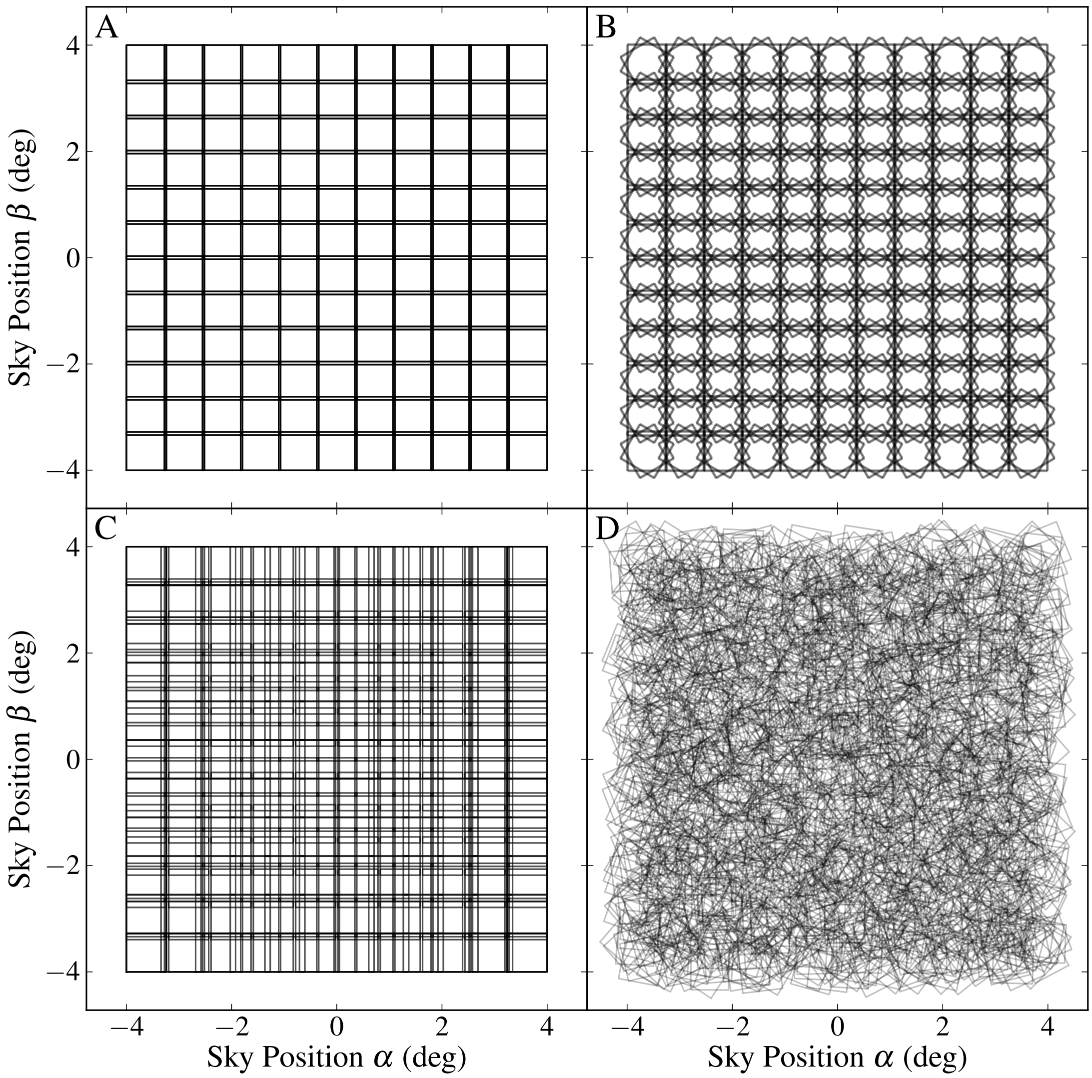


Figure 4.4: Focal plane footprints projected onto the sky according to the four simple survey strategies described in Section 4.4 and summarized in Table 4.2. Surveys A, B and D have 1728 pointings and survey C has 1720 pointings.

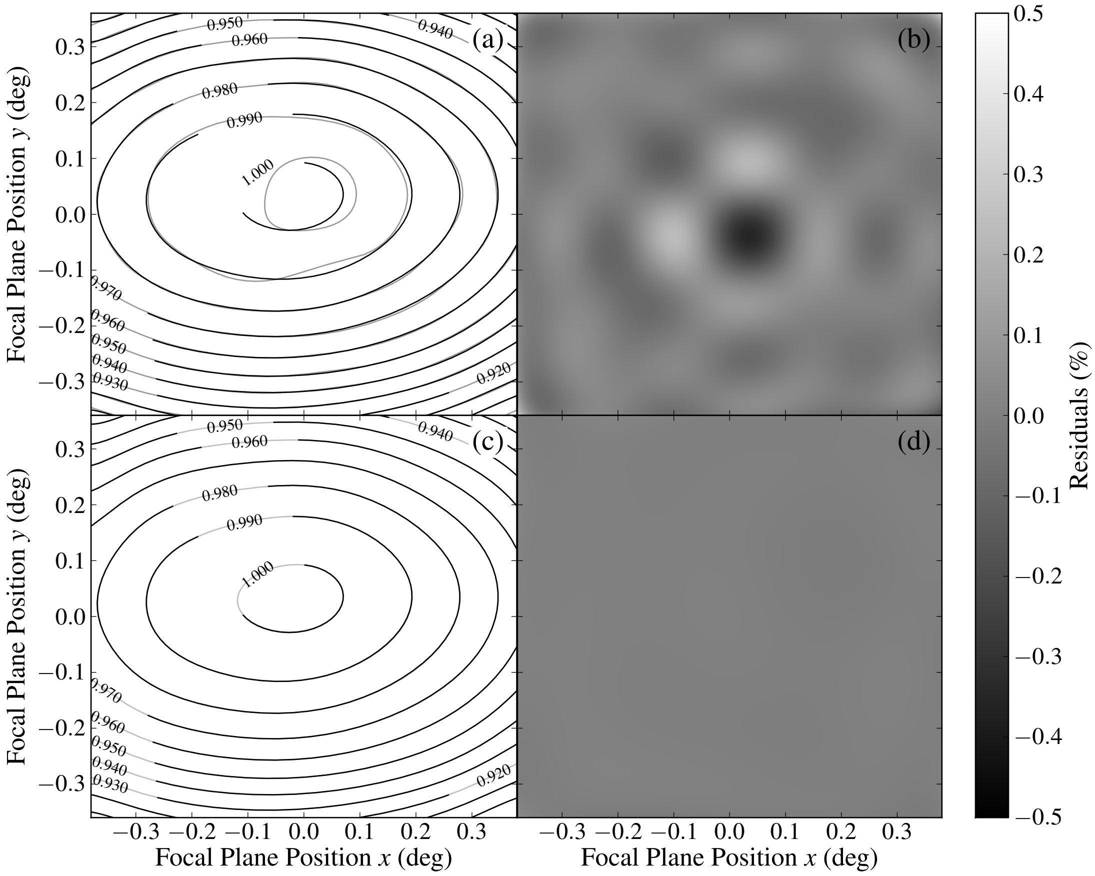


Figure 4.5: A comparison of the fitted instrument response model $f_{\rm fit}(\vec{x}_j|\vec{q}_{\rm fit})$ obtained from self-calibrating the Survey D dataset compared to the true $f_{\rm true}(\vec{x}|\vec{q}_{\rm true})$ and best-in-basis $f_{\rm best}(\vec{x}_j|\vec{q}_{\rm best})$ instrument response models. (a) Contour plot of the fitted (black) compared to the *true* (gray) instrument response. (c) Contour plot of the fitted (black) compared to the *best-in-basis* (gray) instrument response model. The best-in-basis instrument response is the best fit to the true instrument response possible with the basis used to model the instrument response in the self-calibration procedure (in this case an eighth order polynomial). The plots (b) and (d) show the residuals between the two instrument response models plotted in (a) and (c) respectively.

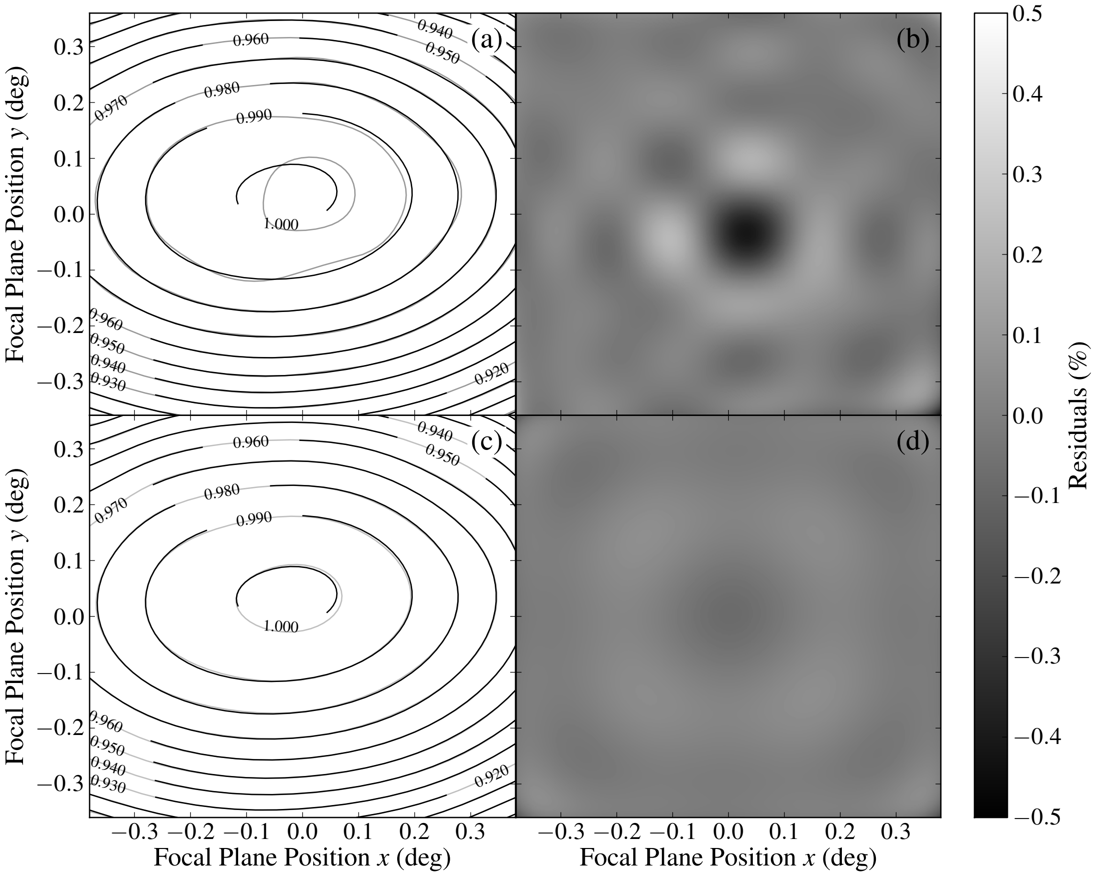


Figure 4.6: Same as Figure 4.5 for the Survey B dataset after 4270 iterations of the self-calibration procedure. The quality of the final fit is worse than for Survey D, with residuals still visible in the comparison with the best-in-basis fit $f_{\text{best}}(\vec{x}_j|\vec{q_{\text{best}}})$ (d).

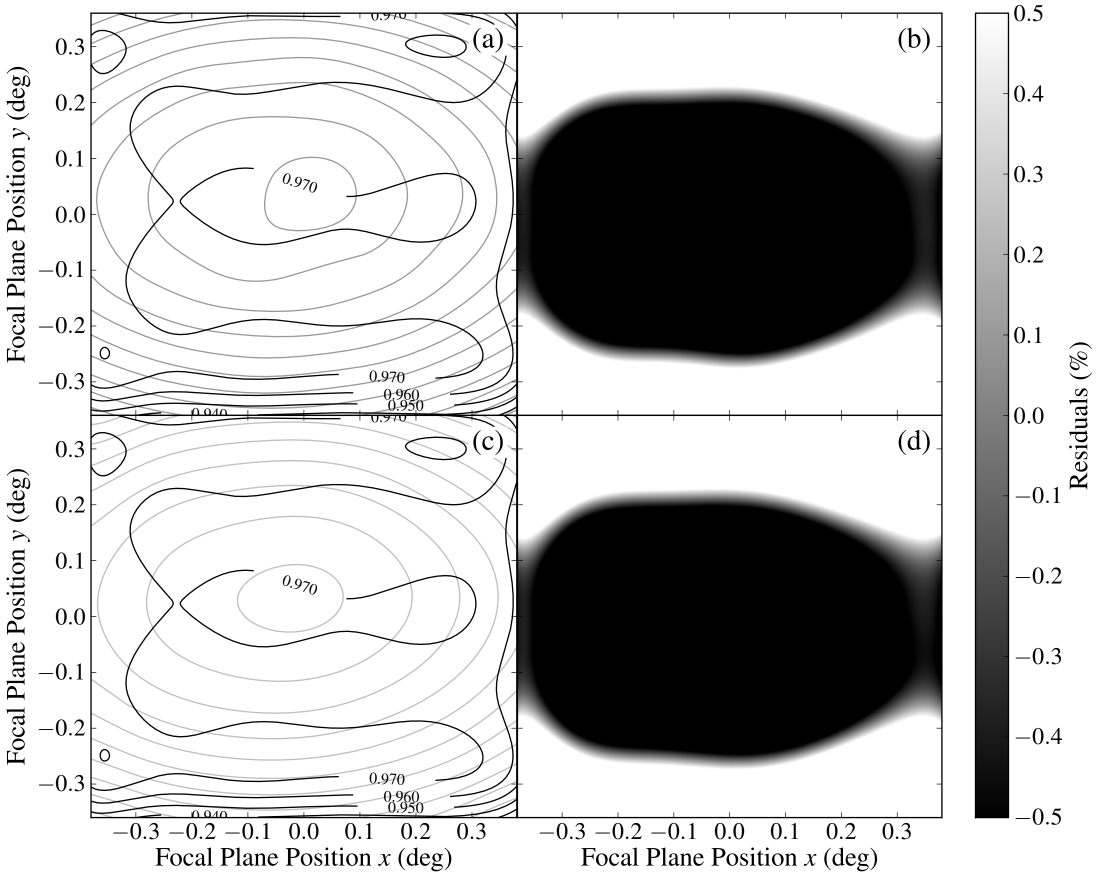


Figure 4.7: Same as Figure 4.5 for the Survey A dataset after 16,384 iterations of the self-calibration procedure. The system did not converge to a solution.

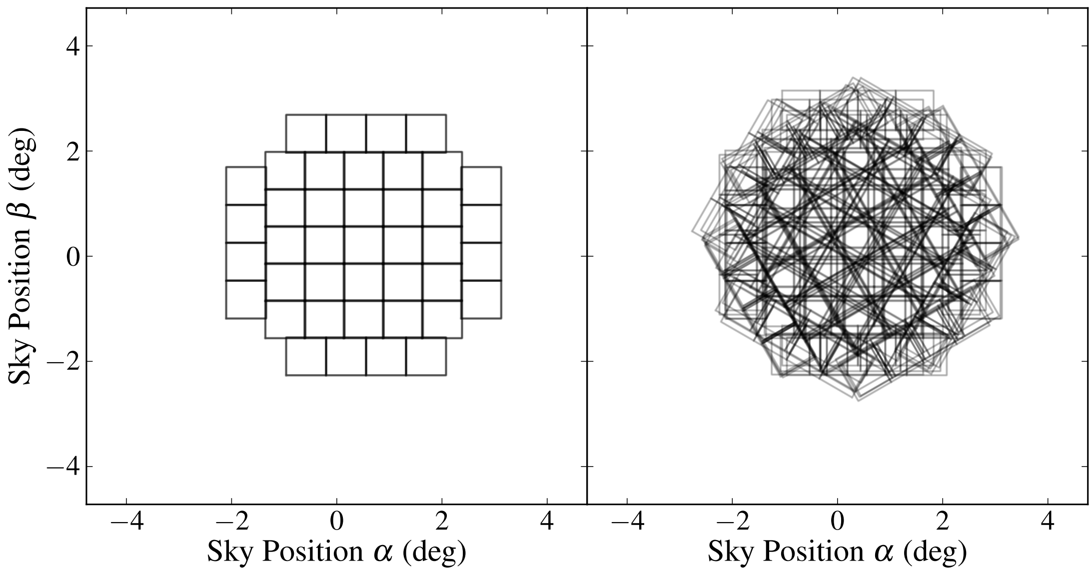


Figure 4.8: A possible implementation of the Deep Field observing strategy. Left: Focal plane footprints projected onto the sky from a single pass over the Deep Field, Right: the total 12 passes over the Deep Field. This survey was defined based on requirements set from the performance analysis of the self-calibration procedure with the simple survey strategies A to D.

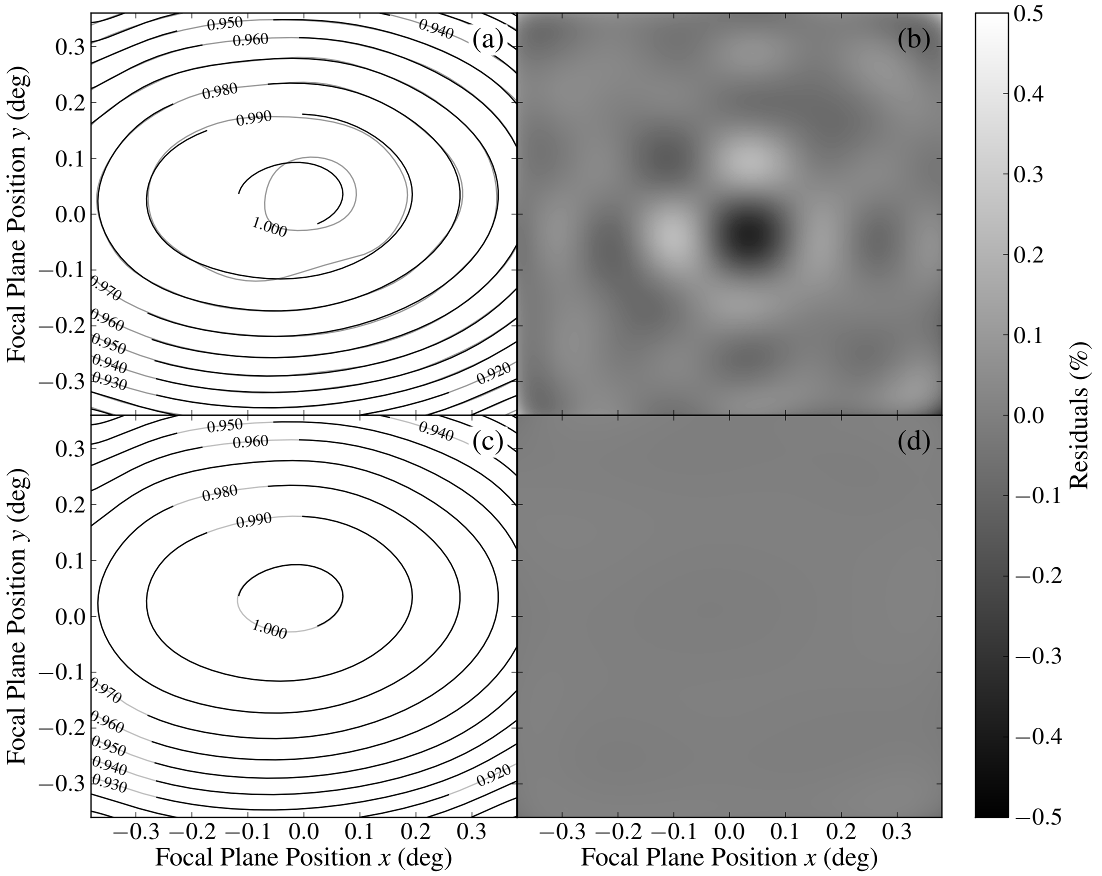


Figure 4.9: Same as Figure 4.5 for the Deep Field Survey dataset. As can be seen in Figure (c) and (d), the final instrument response fit is close to the best that can be achieved with the eighth order polynomial basis used to model the instrument response in the self-calibration procedure.

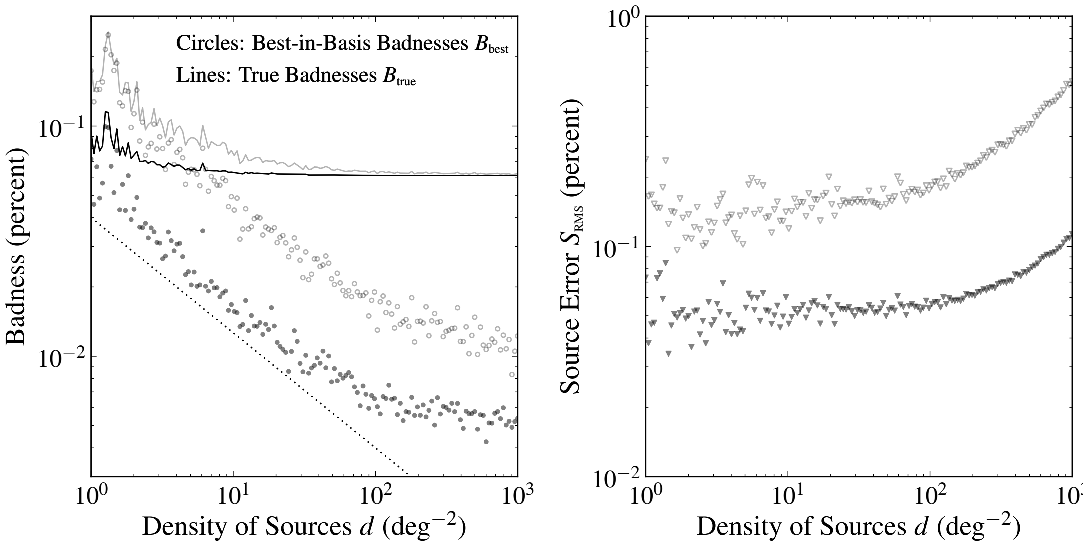


Figure 4.10: The variation in the quality of the final fitted solution with an increase of the source densities used in the self-calibration procedure for two values of $\varepsilon_{max}$, the quantity that sets the difference between the true and assumed uncertainty variance (see Subsection 4.1.2): $\varepsilon_{max} = 1.0$ (black line and black symbols) and $\varepsilon_{max} = 10.0$ (gray line and open symbols). Left: The *true* badness $B_{true}$ (lines) and the best-in-basis badness $B_{best}$ (circles) of the final fit with different source densities $d$. A guide line (dotted) with a gradient of $d^{-2}$ is also shown. Right: The RMS source error $S_{RMS}$ in the final fitted solutions.

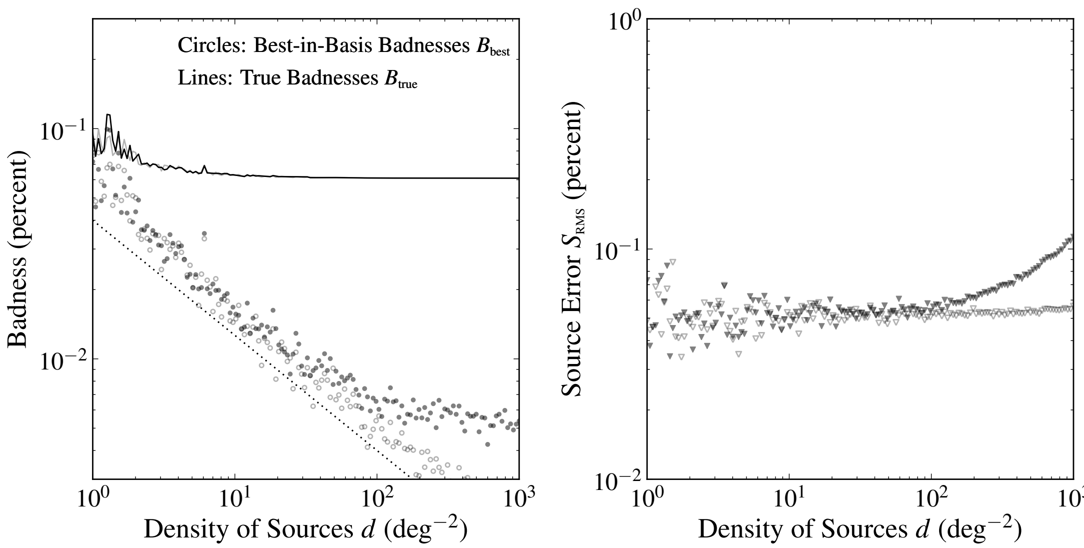


Figure 4.11: The variation in the quality of the final fitted solution with an increase of the source densities used in the self-calibration procedure. Two cases are presented: (i) black line and black symbols: corresponds to a simulation run with the representative synthetic sky (same as $\varepsilon_{\mathrm{max}} = 1.0$ case in Figure 4.10). (ii) gray line and open symbols: correspond to a simulation run in which the number of bright sources within the sky is artificially increased ten-fold, therefore the defined source densities are made up from brighter sources than in case (i). Left: The *true* badness $B_{\mathrm{true}}$ (lines) and the *best-in-basis* badness $B_{\mathrm{best}}$ (circles) of the final fit with different source densities $d$. A guide line (dotted) with a gradient of $d^{-2}$ is also shown. Right: The RMS source error $S_{\mathrm{RMS}}$ in the final fitted solutions.

# Chapter 5

# A Concept for the Euclid Near-Infrared Calibration Source[1]

**Chapter Abstract:** In this chapter I present a concept for the Euclid Mission's near-infrared flat-field calibration source that I devised during the Euclid Assessment Study. This source was required to correct for small-scale variations in pixel sensitivities by illuminating the focal plane with a high photon flux, with a wavelength distribution similar to that of the three photometry bands. I proposed that a near-infrared diffuser plate be mounted to a shutter mechanism positioned at the exit pupil of the telescope, and that this could be used as a calibration target when illuminated with a ring of low power tungsten lamps. I validated this concept with both optical simulations and environmental tests of the baseline lamps: I found that the illumination from the source will vary by less than 25 % over the channel's large focal plane, that stray light contamination is at a low level and that the baseline lamps are suitable candidates for this source concept.

## 5.1 Introduction

This chapter presents work I completed during the Euclid Assessment Study [1]. This work was not based on the current mission design (see Section 1.2), but instead on an older version. This implementation had the near-infrared photometric channel joined within the Visible Imaging Channel (VIS) in the "Imaging Instrument", and the near-infrared spectroscopic channel as a standalone instrument separated after the telescope's secondary mirror. This mission configuration is shown in Figure 5.1, with the mission's optical design on the left and the mechanical implementation of the Imaging Instrument on the right. The near-infrared photometric channel has some differences between the current and the older mission designs; those relevant to this work are: (1) a plane mirror is included in the older version to fold the light path (due to

[1] This work is reported in the publication *The Euclid Near-Infrared Calibration Source* [26].

spacecraft volume constraints) and (2) the number of near-infrared detectors has changed from 18 ($3 \times 6$) in the old design to 16 ($4 \times 4$) in the new design.

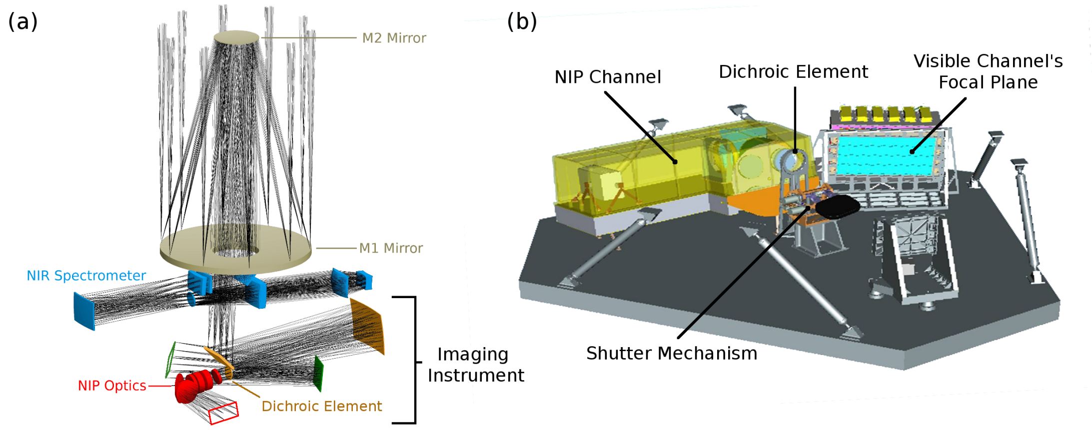


Figure 5.1: The configuration of the mission during the Euclid Assessment Study [1] for which I identified the flat-field calibration source concept presented in this chapter. In this configuration the Visible Imaging Channel (VIS) and the Near-Infrared Photometric Channel (NIP) are combined into a single instrument, and the Near-Infrared Spectrometer (NIS) is a stand-alone instrument separated after the telescope's secondary mirror. (a) The optical design of the mission with the distinction between the different parts highlighted: telescope – beige/orange, NIS – blue, NIP – red and VIS – green. (b) The mechanical implementation of the Imaging Instrument. The critical components for this work are identified: the NIP Channel (also see Figure 6.1), the dichroic element and its mounting structure and the VIS shutter (in its open position) [27].

As introduced in Subsection 3.5.1, the current baseline of the NISP Instrument requires a flat-field calibration source for two reasons: (i) to calibrate the small-scale, pixel-to-pixel sensitivity variations in the focal plane and (ii) to monitor the detector linearity. At the time of this work, the linearity monitoring was not required from the calibration source; it was required purely for the sensitivity variation correction. I therefore present a design of a flat-field calibration source that provides irradiance of the focal plane that is smooth on small-scales, which can be used to correct for the local variations in pixel sensitivities. Nevertheless, with the appropriate detector read mode, this concept could also be used for linearity monitoring. The large-scale structure in this irradiance could be constrained with the self-calibration procedure introduced in Chapter 4. Since the pixel sensitivities are wavelength dependent, the calibration source should ideally provide focal plane illumination with the same wavelength distributions as the photometry bands.

When designing space hardware, it is important to consider the heritage of the individual components. Using parts that have previously flown in space can significantly reduce the qualification efforts, which can result in lower development times and, importantly, costs. This preference for space proven components drives the design of the calibration source. Space hardware must also survive exposure to hostile environments: the calibration source will be subjected to high vibration loads during launch, a low operating temperature of 150 K and a significant radiation dose during its lifetime.

## 5.2 Calibration Source Design

### 5.2.1 Concept

The Visible Imaging Channel (VIS) requires a shutter mechanism to prevent external light from reaching its focal plane during the readout of its CCDs. The baseline shutter design is described by Glauser et al. [28]. The shutter will be inserted into the optical beam close to the telescope's exit pupil, which is located at the common dichroic element (see Figure 5.1). At this position, the shutter blocks external sources from reaching both the visible imager and the near-infrared photometric channel. To avoid additional hardware, I proposed that the back side of this shutter is used as a flat-field calibration target, thus negating the need for an additional mechanism. This location, close to the pupil plane, is favorable for a flat-field calibration source. The VIS shutter must operate quickly, and with a minimum impact on satellite stability, so the additional mass required for the calibration source should be kept to a minimum. Due to the mechanical motion, it would be difficult to provide electrical power to light sources on the shutter itself. I therefore proposed that the back surface of the shutter be illuminated with multiple light sources mounted on separate structures. This concept requires that the back surface of the shutter is diffuse in the channel's wavelength range ($0.92 - 2.0$ μm), and therefore I proposed that a near-infrared diffuser plate is attached to this mechanism.

This calibration concept has a number of advantages: (i) all of the photometric channel's optical elements – and the dichroic element – are included in the calibration path, (ii) the flat-field calibration can be done in all photometry bands (as the filters are included in the calibration path), (iii) the calibration path will be a reasonable representation of the telescope beam and (iv) the concept requires no additional single-point-failure mechanisms. With this concept, the on-board source will only provide a relative photometric calibration, but as discussed in Subsection 3.4.3, the absolute photometric calibration of a near-infrared photometric channel can be constrained with standard stars.

### 5.2.2 Design Specifics

This subsection details the main design considerations for the calibration source concept introduced in Subsection 5.2.1. The broadband emission from tungsten lamps, with a filament temperature of $\sim 2000 - 2500$ K, will easily cover the photometric channel's wavelength range. Such lamps have a large heritage in space based, infrared science instruments. In the baseline calibration source design, the diffuser plate will be illuminated by a ring of low power tungsten lamps. The 4047-00 series of tungsten lamps produced by Micro-Glühlampen-Gesellschaft

Menzel GmbH, Germany have been selected for the calibration source. Their long reported lifetime (2 000 hours[2]), low power and small physical size makes them ideal for this purpose. The lamps' glass envelopes also have a high transmission over the channel's wavelength range.

This calibration concept requires a highly Lambertian reflective diffuser to scatter the light from the tungsten lamps to the channel's focal plane. Labsphere's space-grade Spectralon is a diffuse material with a high reflectance (> 95 %) over the channel's wavelength range [30]. Spectralon has been incorporated into a number of space based scientific instruments as a calibration target[3] and hence, provides a sufficient heritage for space applications. Its resistance to radiation damage, low outgassing rate and its low density are also attractive properties for space missions [30]. In the baseline design, a (dia) 170 mm Spectralon sheet will be mounted to the back side of the shutter mechanism presented by Glauser et al. [28]. The mounting concept has not been considered as this mechanism is not under the responsibility of the Max-Planck-Institut für Astronomie.

## 5.3 Optical Simulations

The optical performance of this calibration source concept has been analyzed using the non-sequential mode of the *ZEMAX* Optical Design Software Package. In this mode, *ZEMAX* utilizes a brute force approach to assess optical performance, with millions of random rays traced from source objects to detector objects. The rays' interactions with intermediate surfaces – either by reflection, refraction or scattering – can be modeled. The optical performance of a system can be assessed when a sufficiently large number of rays have been traced to ensure that sampling effects are no longer significant.

The optical simulations for the calibration source concept were divided into four parts: (i) reflector elements surrounding the tungsten lamps were optimized with the aim of producing a uniform illumination of the diffuser plate, (ii) an accurate scattering model for the Spectralon plate was produced from measurements reported in the literature, (iii) the entire calibration path was simulated and (iv) further analysis on the contamination of the focal plane illumination from stray light was performed. In the next subsections, the main components in the optical simulation are summarized.

### 5.3.1 Individual Component Considerations

#### Lamp Model

Only the tungsten lamps' filaments were included in the optical simulations; the filament length, number of turns and radius were all modeled based on information supplied by the manufacturer. Physical inspections of these lamps performed at the Max-Planck-Institut für Astronomie

[2]Lifetime is defined by when half of the units in a sample fail [29].

[3]For example the MODIS instrument on the Terra satellite [31] and the MERIS instrument on the ENVISAT satellite [32].

have shown that there is some variation between the filaments of different lamps, which is not surprising due to the very small size of these elements. Other lamp structures, such as the supporting wires and the glass envelope, were not considered in this analysis.

### Reflector Elements

Housing the tungsten lamps in reflecting elements offers two advantages: (i) it concentrates the light on the diffuser plate, thereby increasing the efficiency of the system, reducing stray light and preventing spurious reflections from other structures and (ii) it increases the uniformity of the illumination across the Spectralon diffuser plate. Since the lamp and reflector pairs will illuminate the diffuser plate from the side, a non-rotationally symmetric reflector shape has superior optical performance than a rotationally symmetric one. An elliptical paraboloidal shape was chosen for the reflector elements, as it provides good optical performance and has a relatively simple form. The reflector surface can therefore take different shapes in the two directions perpendicular to its central axis. A diffuse surface finish on these elements was found to be optically superior than a pure reflecting one. During the optical simulations, these reflector elements were considered to be perfect Lambertian diffusers.

In the baseline design, twelve lamp and reflector pairs – equally spaced around its circumference – will illuminate the Spectralon diffuser plate. The single lamp and reflector pairs were optimized with the goal of producing as uniform as possible illumination across the entire diffuser plate. The rationale behind this optimization was to limit the impact of a lamp failure on the total diffuser illumination. The position, orientation, curvature constants and aperture size of the paraboloidal reflecting elements were all optimized within appropriate physical restrictions. In the optimized design the lamp and reflector pairs were positioned 90 mm above the diffuser plate and at a radius of 130 mm from its center, close to the dichroic mounting structure shown in Figure 5.1b.

### Spectralon Diffuser Scattering Model

Since the Spectralon [30] diffuser plate will be inserted close to the pupil plane, the quality of the optical simulations depends critically on the accuracy of its scattering profile. The distribution of scattered light in angle space from the diffuser plate will correspond to the spatial distribution on the focal plane.

Early et al. (2000) [33] reported the measured bidirectional reflectance distribution function (BRDF) for Spectralon. The BRDF of a surface relates the scattered radiance at a viewing angle to the incident irradiance. It is defined as

$$\mathrm{BRDF}(\theta_i, \phi_i, \theta_s, \phi_s, \lambda) = \frac{dL_s(\theta_s, \phi_s, \theta_i, \phi_i, \lambda)}{dE_i(\theta_i, \phi_i)} \quad , \tag{5.1}$$

where $L_s$ and $E_i$ are the scattered radiance and the incident irradiance, respectively. The quantities $\theta_i, \phi_i, \theta_s$ and $\phi_s$ are the spherical polar coordinates for the incident and scattered rays, respectively, relative to the surface normal. The scattering from a surface is generally wavelength dependent.

In certain cases, a simplified representation of the BRDF can accurately portray the scattering profile from a surface. One such simplification is the ABg scattering model, the name of which is derived from the standard letters assigned to the three parameters it depends on. In this model, the BRDF is considered as a function of only one variable $\vec{x}$. The variable $\vec{x}$ is the vector between the scattered ray's unit vector and the specular ray's unit vector, both projected onto the scattering surface. In this model the BRDF is given by:

$$\mathrm{BRDF}(\vec{x}) = \frac{A}{B + |\vec{x}|^g}\,, \tag{5.2}$$

where $A, B$ and $g$ are constants to be found.

Early et al. (2000) [33] measured the BRDF for Spectralon at viewing angles sampled every $10^\circ$ between $-60 \rightarrow 60^\circ$ for incident angles of 0, 30, 45, $60^\circ$. Only scattering angles in the same plane as the incident rays were sampled. I fitted the reported data, measured at 940 nm, to the ABg scattering model and I included the corresponding $A$, $B$ and $g$ values in the calibration source's optical simulations. Note that 940 nm is at the low end of the channel's spectral range ($920-2000$ nm). When the diffuser is in its nominal position (see Subsection 5.3.2), only rays scattered at angles below $21^\circ$ to the surface normal will strike the channel's focal plane. The optical simulations must therefore accurately reproduce the scattering profile of the Spectralon diffuser below this angle.

The measured data from Early et al. (2000) [33] are reproduced in Figure 5.2 for incident angles of $\theta_i = 0^\circ$ and $\theta_i = 45^\circ$. In the coordinate system used, the incident angle $\theta_i$ and the scattering angle $\theta_s$ are both defined from the surface normal such that the specular ray is at $-\theta_i$. The excellent diffusive properties of Spectralon can be seen, as for both incident angles the BRDF is close to the theoretical Lambertian value of $1/\pi = 0.318$ for all scattering angles. The simulated scatter from the Spectralon diffuser plate, based on the ABg model fit to the measured data, is overlaid. In Figure 5.2a, the ABg fit of the measured data at this incident angle was directly included in the simulations. At this incident angle of $\theta_i = 0^\circ$, and also for $\theta_i = 30, 45$ and $60^\circ$, the simulated BRDF can reproduce the input data to better than 2% for scattering angles of less than $21^\circ$. To test how well the optical simulations reproduce the measured BRDF between the available incident angles the data for $\theta_i = 45^\circ$ were temporarily omitted. The simulated scatter at this intermediate angle, which is interpolated from the ABg model data at $\theta_i = 30$ and $60^\circ$, is shown in Figure 5.2b. For scattering angles of less than $21^\circ$ the simulated BRDF, based on this interpolation, reproduces the measured data to within 3%. I therefore conclude that the simulated scattering profile from the Spectralon diffuser plate reproduces the actual scatter for not only the incident angles where input data are available, but also for those in-between.

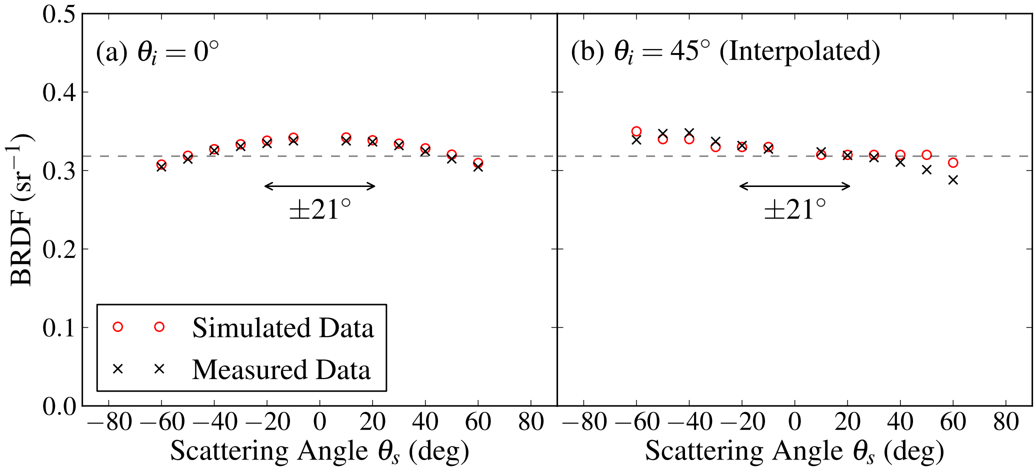


Figure 5.2: The simulated BRDF for the Spectralon diffuser plate compared to the measured values from the literature [33] that they were based on. In (a) the reported data were used as an input for the simulations but in (b) the simulated scattering profile has been generated with data interpolated from measurements with $\theta_i = 30$ and $60°$. A guide line is included at $1/\pi$, the BRDF value of a perfectly Lambertian diffuser. Only rays that leave the diffuser plate at an angle below $21°$ to the surface normal will strike the focal plane, this region is identified in the plots.

### 5.3.2 Full Calibration Path Simulations

The Spectralon diffuser plate was considered to be illuminated with twelve identical lamp and reflector pairs. The final design will incorporate twenty four pairs, offering complete redundancy. Light rays were then traced through the entire calibration path from the lamps to the focal plane. Baffles were included to ensure that only representative rays reached the focal plane. The contamination from stray light was therefore not considered, but further analysis was conducted to assess this issue and the results are presented in Subsection 5.3.4. The optical simulations of this calibration source were only performed at $\lambda = 940$ nm, as this is the only wavelength for which the BRDF of Spectralon was reported [33].

Initial optical simulations identified an optimum position and orientation of the Spectralon diffuser plate: a position $\sim 104$ mm back along the optical axis from the dichroic element, a vertical offset of 10 mm from the optical axis and an orientation parallel to the channel's focal reducing optics was found to give good optical performance. I therefore suggest that the VIS shutter is positioned so that the diffuser plate can be inserted into the optical path at this position. The optical simulations presented assume this position and orientation of the Spectralon diffuser plate.

### 5.3.3 Focal Plane Illumination

The focal plane illumination from the end-to-end optical simulations of the channel's calibration path is shown in Figure 5.3. The detector pattern proposed by Schweitzer et al. [34] is overlaid. The focal plane consists of 18 (3×6) Teledyne Hawaii -2RG 2k×2k near infrared detectors [9]. The active areas of these detectors do not extend to their edges, and therefore gaps in the focal plane coverage are unavoidable when creating a mosaic of multiple detectors. From Figure 5.3 it can be seen that the simulated focal plane illumination varies by less that 25 % over the entire active focal plane, with lower variations across the individual detectors. The simulations show that there is a higher irradiance at the center of the focal plane, with it falling off towards the edges. The focal plane illumination is similar to that produced by an over-sized perfect Lambertian source at the shutter position. The channel's optical design, an accurate scattering model from the Spectralon diffuser and the twelve optimized reflector and lamp pairs have all been included in this simulation. These data have been smoothed to reduce the sampling effects caused by the random nature of the ray tracing procedure.

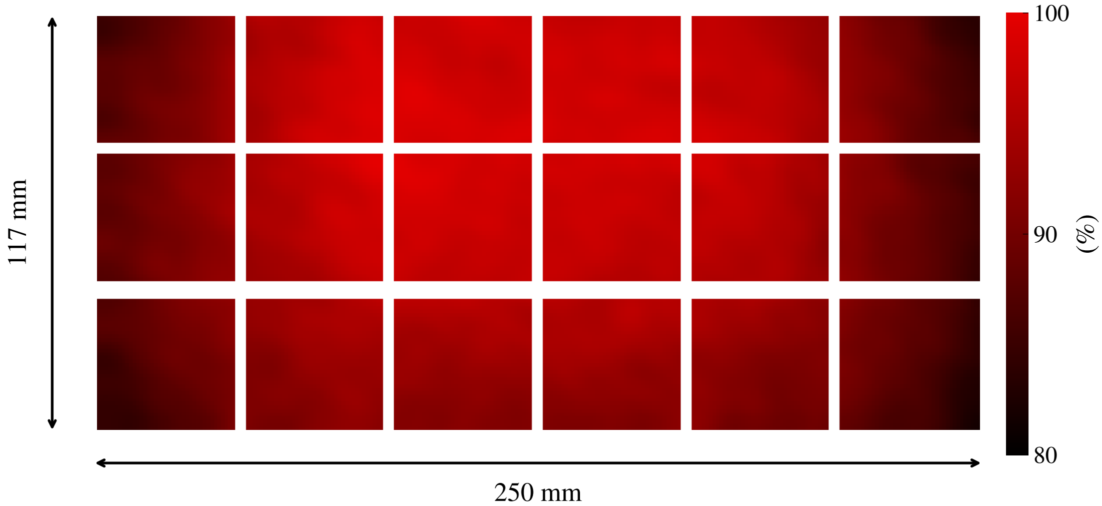


Figure 5.3: The relative focal plane irradiance from the end-to-end optical simulations of the flat-field calibration source at a wavelength of 0.94 μm. The active area of the 3 × 6 detector mosaic is overlaid. Note that this focal plane design is outdated and is not consistent with the current NISP Instrument baseline presented in Figure 2.12.

### 5.3.4 Stray Light Analysis

The results from the optical simulations of the calibration source have shown that it provides suitably uniform focal plane irradiance. It is now pertinent to investigate if scattered light will contaminate this illumination. Does some light, for example, still make its way to the focal plane along unintended paths? This issue has been investigated by including the channel's main mechanical components in the optical simulations. The channel's covering structure, the filter wheel disk, the mirror support, the final lens support and simplified lens mounts have all been considered (see Figure 5.4a). The effects of scattering from these elements were simulated. The lens mounts were considered as perfect absorbers, but the surfaces of the other elements were assumed to have an optically black coating. These surfaces were modeled as perfect Lambertian diffusers with a high absorption of 96 %. This a good approximation for potential black coatings, such as Acktar's Fractal Black, which has a reflectance of less than 4 % in the channel's wavelength regime [35]. In these simulations the Spectralon diffuser plate was considered as a perfect Lambertian source in the nominal position, as defined in Subsection 5.3.2.

Figure 5.4b shows the focal plane irradiance from rays that have scattered from the channel's mechanical components only. Rays that followed the calibration path have been excluded. These data are more noisy than those presented previously, as less simulated rays have intersected the focal plane. This is because: (i) there is a lower probability of rays following a stray light path than the calibration path and (ii) this stray light simulation is computationally demanding due to the multiple scattering surfaces and complicated object shapes. The simulations show that scattered light does contaminate the focal plane irradiance, but it is at a much lower level than the light that follows the calibration path. This contamination has a magnitude of less than 0.1 % relative to the calibration path illumination discussed in Subsection 5.3.3. Since the source will only be used for relative photometric calibration, a uniform background illumination of the focal plane will not degrade its performance. Due to the low level of the structures in the scattered light's focal plane irradiance, compared with the $\sim 25$ % variation present in the calibration path illumination, I concluded that this calibration concept can be included in the baseline mechanical implementation of the channel without the need for additional light baffles. The magnitude of the small-scale structure in the stray light contamination of the focal plane irradiance is consistent with the level of the small-scale structure modeled in the instrument response considered for the self-calibration simulations (see Subsection 4.1.2).

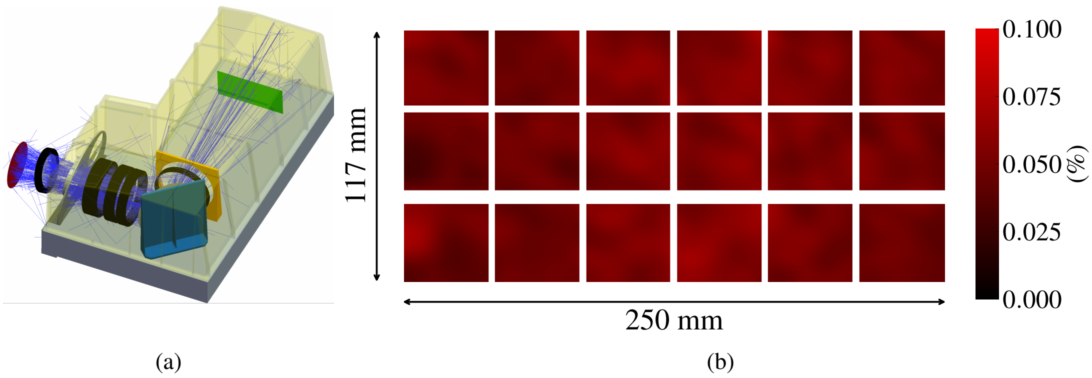


Figure 5.4: Stray light analysis of the proposed calibration source design. (a) The elements of the channel included in this analysis. The simplified lens mounts (black) were considered as perfect absorbers. The other mechanical elements were assumed to have an optical black coating that acts as a perfect Lambertian diffuser with a 4 % reflectance. A small set of traced rays is shown in blue. The diffuser plate is shown in red. (b) The focal plane irradiance from stray light rays that do not follow the calibration path. The stray light power reaching the focal plane is less than 0.1 % of that received from the intended calibration path.

## 5.4 Mechanical Implementation

The optical performance of the proposed calibration source has been verified in the previous sections. Here, I will detail the mechanical implementation conceived for this concept. Due to the proximity of the lamp and reflector pairs to the common dichroic element, I proposed that they are housed on its mounting structure. Amiaux et al. (2010) [27] have detailed the baseline design of this structure. Modifications to this structure to incorporate the calibration source elements were not considered, as this was beyond the scope of the Max-Planck-Institut für Astronomie's responsibility. Nevertheless, the mechanical implementation of the lamps and reflectors in a generic aluminium structure was considered. The proposed mounting strategy is shown in Figure 5.5. To produce such a mounting the reflector elements could be milled out of a solid piece of aluminium. The reflector surface could then be roughened to produce a diffuse surface finish. In this concept the MGG 4047-00 tungsten lamps are directly attached to the reflectors. The lamp wires, insulated with polytetrafluoroethylene (PTFE) tubing, would be inserted into two small holes (dia. 1 mm) in the back of the reflector. The cryogenic glue Stycast 1266 could then be used to firmly secure the lamp in place.

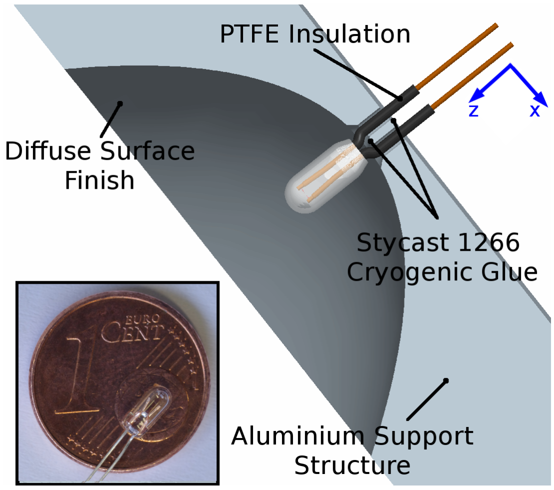


Figure 5.5: The mechanical implementation of the MGG 4047-00 tungsten lamps within the aluminium reflecting elements I proposed for this calibration source concept. The inset shows the small baseline tungsten lamps in front of a 1 Euro cent coin. The axes tested during the vibration verification tests are shown in blue.

## 5.5 Initial Component Verification

Four critical requirements apply to the channel's subcomponents: (i) they must survive high vibration loads induced during launch, (ii) they must be operable in a vacuum, (iii) they must be operable at the final instrument temperature of 150 K and (iv) they must be radiation hard (not tested). Initial performance tests have been conducted on the baseline tungsten lamps to validate their selection for the channel's calibration source. The proposed diffuser material (Labsphere's space-grade Spectralon [30]) has already been flown on a number of space missions and therefore no further testing is required in the early stage of this project. I have tested the baseline tungsten lamps at cryogenic temperatures, in a vacuum and also under vibration loads. These tests show that the MGG 4047-00 tungsten lamps and the proposed mounting strategy are suitable candidates for the calibration source.

### 5.5.1 Vibration Tests[4]

Vibration tests were performed on a sample of the baseline tungsten lamps mounted in a representative way. Three lamps were mounted to an aluminium element as described in Section 5.4, although the reflector shapes were not reproduced in this aluminium element. The whole assembly was vibrated both with sinusoidal and random excitation in the x- and z-axes indicated in Figure 5.5. Sinusoidal load sweeps were performed in the frequency range 21.25 – 100 Hz, at a sweep rate of 1 octave per minute and with an amplitude stepped up to 40 g. For the random vibration tests, two minute tests were performed with acceleration levels of 20, 30, 40 and 50 g

[4] I would like to thank N. Wittekind at Carl Zeiss Optronics GmbH for his support with this test.

rms. The lamps and their mounts both survived these strong vibration loads.

### 5.5.2 Cryogenic Tests[5]

The baseline MGG 4740-00 tungsten lamps have been successfully operated in a vacuum at less than 90 K, which is below the channel's operating temperature of 150 K. Two lamps, without a representative mounting, were operated continuously at this temperature for over 40 hours with no drop in performance observed. To test the mounting concept at cryogenic temperatures, a sample of three representatively mounted lamps was thermally shock tested by dipping them into liquid nitrogen. The assembly was cycled between ambient and liquid nitrogen temperature five times. The tungsten lamps and the mounting concept both withstood this cryogenic cycling.

## 5.6 Outlook

In this chapter, I have presented a concept for the Euclid Mission's near-infrared flat-field calibration source, which would provide an irradiance that varies by less than 25 % over the photometric channel's large focal plane. This design has been validated with optical simulations and with tests of the baseline tungsten lamps. Further investigations have confirmed that stray light contamination of the focal plane illumination is at a low level and would not introduce significant small-scale structure to the flat-field exposures. To mature the design further, the optical properties of the lamps and the Spectralon diffuser plate would need to be better constrained. For the lamps, this would involve spectral measurements to confirm that they are suitably bright in the channel's wavelength range. Although the Spectralon diffuser is known to be highly diffusive across the required wavelength range, spectral measurements would also be required here to obtain BRDF measurements at higher wavelengths, which could then trivially be incorporated into future simulations. The interfaces to the shutter mechanism and the dichroic holder would also need to be defined.

At the end of the Euclid Assessment Study the Euclid Mission was redesigned and the two infrared channels were combined into a single instrument (see Subsection 1.2.3). Unfortunately this calibration concept is not suitable for this redesigned implementation, as the VIS shutter mechanism is no longer at the telescope's exit pupil. There is therefore no mechanism at the pupil plane able to hold the diffuser plate. Unfortunately, this calibration source concept will therefore not be developed further.

[5] I would like to thank U. Grözinger (MPIA – Germany) for his support with this test.

# Chapter 6

# An Assessment of the Euclid Filter Wheel Mechanism[1]

**Chapter Abstract:** This chapter details my assessment of the near-infrared photometric channel's filter wheel mechanism. The work on this critical, single-point-failure mechanism was performed during the Euclid Assessment Phase. I present a design overview, followed by specific discussions of the critical components: the wheel disk, the drive and the positioning system and the bearing system. As this work was performed during an assessment phase, the aim was not to produce the final design of the wheel mechanism – this would require an in-depth prototyping campaign – but to prove feasibility by identifying suitable concepts. In the second part of this chapter, I turn to a detailed investigation of the mounting of the large and fragile filter elements to the wheel mechanism. I present two designs for these structures, both of which have been analyzed with finite element analysis. These structures have been subjected to a prototyping campaign, the results of which have allowed me to select the most appropriate candidate for the near-infrared photometric channel.

## 6.1 Introduction

The primary purpose of the Euclid Mission's near-infrared photometric channel is to supplement the visible shape measurements of galaxies within the survey with multi-band, near-infrared photometric data. These will be used with ground-based, multi-band, visible photometry to photometrically estimate the redshifts of the galaxies imaged. Providing multi-band, deep, near-infrared photometry over a large portion of the extragalactic sky will also provide a vast dataset for legacy science.

[1]This work has been published in two technical articles: *A Filter Wheel Mechanism for the Euclid Near-Infrared Imaging Photometer* [36] and *A Filter Mount for the Euclid Mission* [37].

Multi-band photometry can be implemented in the channel in two ways: (i) filters can be placed directly on the focal plane, thus segmenting it into different areas for different bands, or (ii) a filter wheel mechanism can be used to insert different near-infrared filters into the channel's optical path. Mechanisms in space mission are always critical: they can act as single-point-failure components and they are time consuming and expensive to design, test and qualify. Where possible, mechanisms should be avoided. Placing filters on the focal plane can also cause problems, particularly relating to multiple internal reflections causing ghost images in the science data. From these two options, the Euclid Consortium opted for a filter wheel mechanism for this channel, the responsibility for which was assigned to the Max-Planck-Institut für Astronomie during the Euclid Assessment Study (September 2008 – November 2009 [1]).

As introduced in Chapter 5, the design of the mission was different during this study phase: the near-infrared spectrometer and photometer were not amalgamated into a single instrument, they were separated into two distinct instruments after the telescope's secondary mirror. The mission concept during this time is shown in Figure 5.1, with the near-infrared photometric channel (the "Near-Infrared Imaging Photometer" – NIP) shown in Figure 6.1. For this work, the most significant difference compared to the current baseline is that this older version of the channel had four photometric bands, and therefore the filter wheel must house four near-infrared filters instead of three.

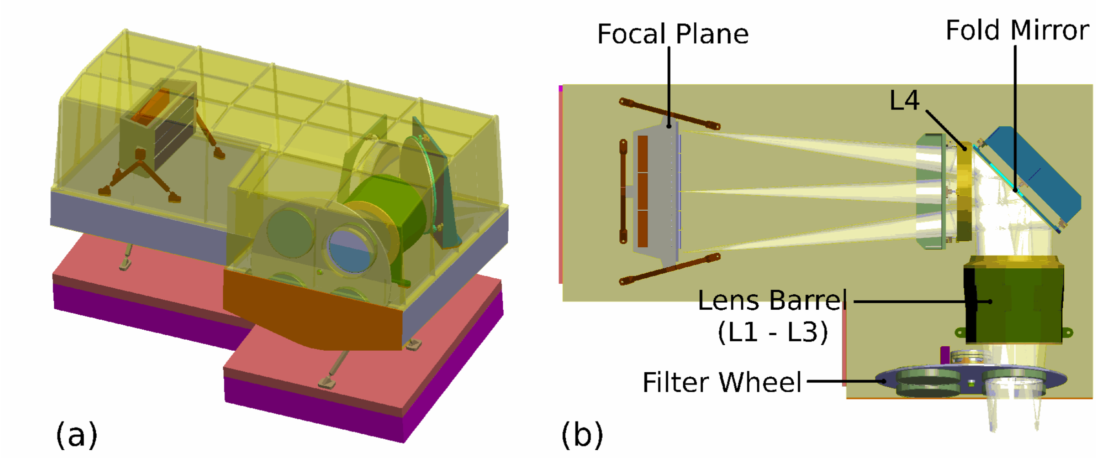


Figure 6.1: The implementation of the photometric channel, called the Near-Infrared Imaging Photometer (NIP), considered during the Euclid Assessment Phase [1] [34]. The work presented in this chapter corresponds to this design of the channel. The filter wheel mechanism shown here is an early design model and is not representative of the work presented in this chapter. The NIP channel is enclosed in a dedicated box to limit thermal background and stray light. The channel will be passively cooled to $\sim$ 150 K, with the focal plane module cooled further to $\sim$ 120 K.

There are a number of specific challenges relating to the design of space hardware. The first is that components must survive the violent transition to space, in which the satellite and its subcomponents will experience strong vibration loads. This leads to two design considerations, the components must not only survive these loads, but they must also be stiff so that their lowest resonant frequency is above the high amplitude, low frequency vibrations from the launcher. The near-infrared photometric channel is passively cooled to 150 K to prevent thermal emission from the instrument dwarfing the scientific observations. Components must not only be operable at this temperature, but they must also survive the transition from ambient. Due to the channel's low temperature and wavelength sensitivity, low power dissipation is required in the mechanism actuator and supply lines. Using components that have been successfully flown in space can significantly reduce the qualification times and costs. Therefore components and concepts that have been "space proven" are favored in the design of this mechanism.

This chapter first addresses the channel's filter wheel mechanism. The requirements on this mechanism are introduced in Subsection 6.2.1. I present a design overview in Subsection 6.2.2, followed by a deeper analysis of the critical components: (i) the filter wheel disk, (ii) the drive and positioning system and (iii) the bearing system. As introduced in Section 2.3.5, a large mechanism could introduce a significant perturbation to the satellite stability; this is quantified in Section 6.3. The second half of this chapter deals with the mounting of the large, fragile optical elements to the wheel disk. The requirements on this structure are detailed in Subsection 6.4.1. I present two designs in Subsection 6.4.2, with the corresponding finite element analysis summarized in Subsection 6.4.3. These two designs have been prototyped (Subsection 6.4.4), the results from which have allowed me to identify the most promising candidate for the near-infrared photometric channel's filter mounting structure.

## 6.2 The Filter Wheel Mechanism

### 6.2.1 Requirements

In this older configuration of the mission, the photometric channel included four near-infrared filters positioned close to the pupil plane. The mission's optical design dictated the fused silica substrate and the required optical aperture of (dia) 120 mm for these elements. The elements were oversized to (dia) 127 mm for mounting and to account for mechanism misalignment errors. The thickness of the filters was optimized to reduce the mass of the elements. From finite element analysis, I found that a thickness of $\sim 12$ mm was easily sufficient to survive conservative (50 g) launch loads. The individual optical elements therefore had a mass of $\sim 0.33$ kg and in total the filter wheel had to support $\sim 1.3$ kg of fused silica. At the time of this work, the baseline mission concept required a $20,000$ deg$^2$ extragalactic sky survey in the four photometry bands. From the channel's field-of-view of $\sim 0.5$ deg$^2$, it was possible to estimate the number of 90 deg filter wheel operations required over the lifetime of the mission:

$$\frac{20,000 \text{ deg}^2}{0.5 \text{ deg}^2} \times 4 \text{ dithers} \times 4 \text{ bands} = 640,000 \text{ operations} \quad .$$

Since the spectroscopic channel was implemented as a separate instrument, unlike in the current baseline, it was not necessary to rotate the filter wheel to and from an open position at the beginning and the end of the observation cycle. The number of wheel operations can therefore be reduced by 25 % by using the last filter in one dither exposure as the first in the next. In this case, the number of operations reduces to $\sim 480,000$, which equates to $\sim 120,000$ full rotations. Note that it is not necessary to always have a fixed rotation direction; the lifetime of the mechanism may be found to be different with other rotation strategies. The observing strategy, at the time of this work, required that the filter wheel mechanism inserts the next filter within 15 seconds, with all the settling effects damped in this time. The planar filters did not have any optical power and were positioned close to the pupil plane, so the positioning accuracy of these elements would have been relatively relaxed. Although there was no formal requirement on this, I assumed that the filter wheel mechanism was required to have a repeatability of $< 1$ arcmin. That is to say, the mechanism would need to return the filters to the same position they occupied during calibration exposures – such as flat fields – with a rotational error of less than 1 arcmin. This value is also sufficient to prevent vignetting of the optical beam by misplaced filters.

### 6.2.2 Design Overview

In this subsection I detail a design overview of a potential filter wheel mechanism for the Euclid Mission. This was not intended to be a final design, but by identifying promising concepts I hoped to show that such a mechanism was feasible. One of the most promising designs for the near-infrared photometric channel's filter change mechanism included a centrally driven wheel disk that housed the four optical elements. More exotic mechanisms, such as sliders, were discounted early in the assessment in favor of this more traditional and simpler concept. To mount the four large optical elements, the mechanism needed a wheel disk with an outer diameter of $\sim 400$ mm. This large disk would need to be supported on a dedicated bearing system. The following subsections discuss the three critical components in this wheel design: (i) the filter wheel disk, (ii) the drive and positioning system and (iii) the bearing system. Potential structures for mounting the filters to the wheel disk are detailed in Section 6.4. An example of a filter wheel concept of this type is shown in Figure 6.2.

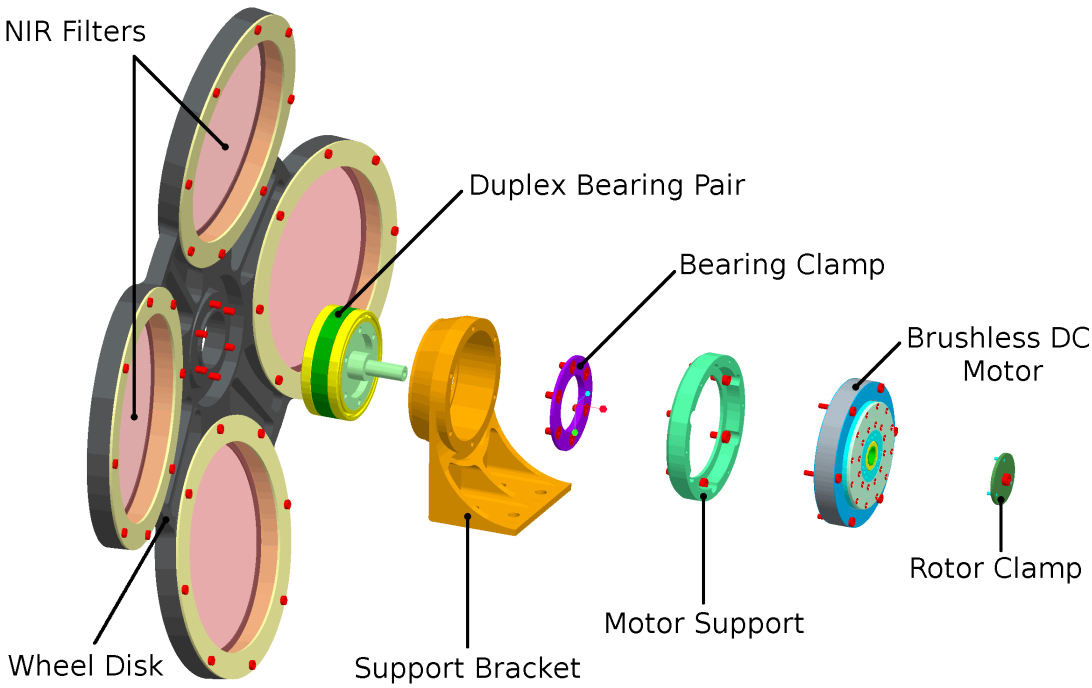


Figure 6.2: An exploded view of a filter wheel concept for the near-infrared photometric channel. This version incorporates a direct drive motor system, with no external positioning system: the feedback from the motor's Hall sensors would be used in a closed loop control.

**The Filter Wheel Disk**

As part of this assessment study, the filter wheel disk was studied in detail to confirm that the mounting of such large optical elements was feasible within realistic mass and volume envelopes. I identified a concept for this structure and I used finite element analysis to validate its performance. In this design, the wheel disk housing the four optical elements (identified in Figure 6.2), would be manufactured from titanium. The titanium grade Ti-6Al-4V was chosen due to its high specific strength, even at low temperatures, and its heritage in space missions. In the channel's optical design, the filters were angled by 8.5 deg with respect to the following focal reducing optics to prevent internal reflections causing ghost images on the detectors. The filter wheel disk was also angled by this amount, not only to allow the mechanism and the following optics to be mounted to a common baseplate, but also to increase the structure's stiffness and to ensure that the center of mass of the moving parts fell within the bearing system.

To validate this design, I have performed finite element analysis with the *ANSYS* Software Package. A subsample of these simulations is presented in Figure 6.3. The two main requirements on this structure were: (i) it must support the four optical elements, with a total mass of $\sim$ 1.3 kg, under launch vibrations and (ii) is must be stiff so that the first resonant frequency of the complete wheel disk is above the low frequency, high amplitude inputs from the launcher. These simulations have included the major components of the wheel disk: the titanium disk

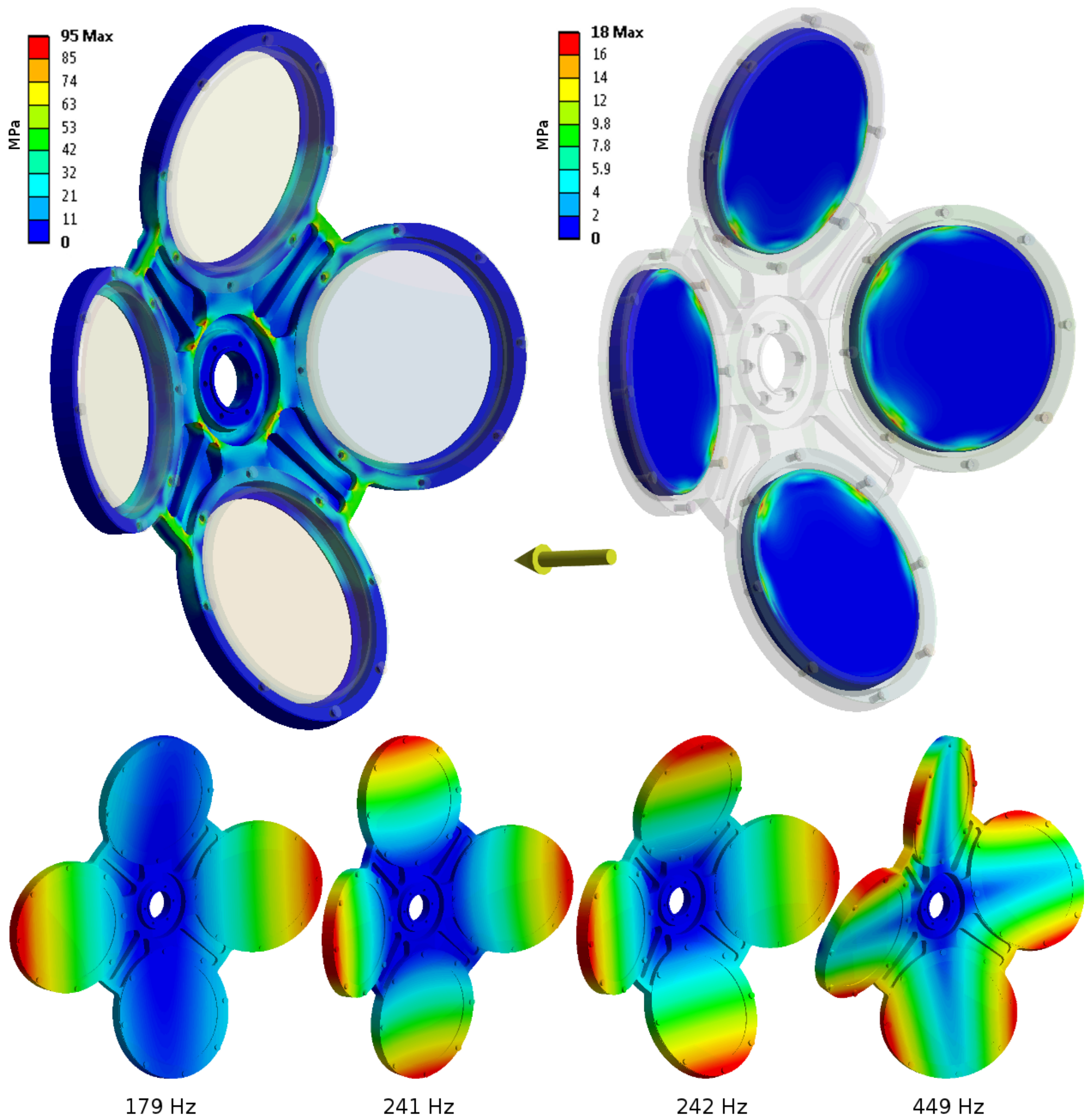


Figure 6.3: Finite element analysis of the wheel disk concept for the near-infrared photometric channel's filter wheel mechanism. Top: The behavior of the total wheel disk structure (wheel disk, filters and filter mounting structures) under a 50 g static acceleration in the axial direction (shown with the yellow arrow). Although the analysis was performed with the complete structure, the stresses in the titanium wheel disk (left) and the four fused silica filters (right) are shown separately for clarity. The displacements are amplified by a factor of 50 in these images. Bottom: The simulated modal shapes of the four lowest resonant frequencies of the complete wheel disk structure.

itself, the four fused silica filters and a simplified version of the Invar (Type 36) filter mounting structures (see Section 6.4). The performance of this structure under simulated launch vibrations is shown in Figure 6.3. In this analysis, launch vibrations were modeled as high static accelerations of 50 g. The peak stresses induced in the system are comfortably below the materials' yield strengths. The maximum stress in the fused silica filters was found to be $\sim$ 18 MPa (compared to a compressive strength of 1150 MPa and a tensile strength of 50 MPa [38]) and the maximum stress in the titanium wheel disk was found to be $\sim 95$ MPa (compressive strength 970 MPa, tensile strength 880 MPa [39]). Similar simulations have been performed with an axial acceleration in the opposite direction. Here the peak stresses in the wheel and filter were found to be $\sim 89$ and $\sim 25$ MPa respectively. Similar results are obtained with a 50 g static acceleration in the radial direction, with peak stresses of $\sim 28$ MPa calculated in the wheel and $\sim 17$ MPa in the filters. Modal analysis has also been performed on the finite element model of the complete wheel disk: the lowest resonant frequency is found at 179 Hz, confirming that the wheel disk was suitably stiff. The first four resonant frequencies and the associated modal shapes are shown in Figure 6.3. This finite element analysis validates this wheel disk concept, confirming that the mounting of such large optical elements in a space-based wheel mechanism is feasible within a realistic mass and volume envelope.

### The Mechanism's Drive and Positioning System

A number of drive and positioning systems were considered for this mechanism. The final trade-off between these options was not performed as the required prototyping campaign was not conducted in the Assessment Study. In this subsection, I discuss the options for the drive and positioning system for the filter wheel mechanism. The two main requirements on the drive and positioning system were: (i) to rotate the filter wheel to the required position accurately ($<$ 1 arcmin) and (ii) to hold the wheel stationary during scientific observations – and importantly – during launch.

A ratchet system was considered for the Euclid filter wheel mechanism. Such systems have heritage from the wheel mechanisms planned for the Mid-Infrared Instrument [40] and NIRSpec [41] instrument proposed for the James Webb Space Telescope (JWST). With such a system, the wheel is rotated to the required position, where a mechanical ratchet engages index bearings on the wheel's circumference, which very accurately forces it to the required position. This system has a number of advantages: (i) the wheel can be held accurately in position without the need for current in the motor coils (both during a scientific observation and during launch) and (ii) the filters can be positioned to a very high rotational accuracy ($<$ 6 arcsec [40]). These JWST mechanisms use brushless DC motor drives[2]. This motor has a permanent magnet rotor that does not have its own bearing; instead it runs on the wheel's main bearing when attached with a fixed axis.

Since the Euclid filter wheel will require a lower rotational precision than these JWST mechanisms, it may also be possible to drive and position the mechanism with the brushless motor alone. Active feedback from the two Hall sensors built into the motor (an additional two are included for cold redundancy) could be combined with predetermined waveforms to generate the drive signals for the two motor phases. When in a stationary position, and without external moments, no power would be required in the motor coils. If external impulses try to

[2]Cryotorquer motor series, designed at the Tieftemperaturlaboratorium (TTL) at Freie Universität (Berlin).

rotate the wheel from the required stationary position, the closed loop control system could generate drive currents in the coils to keep the correct position. This concept would remove the need for a ratchet system, which would simplify the design and reduce the number of critical components that could potentially fail during the large number of wheel operations. In such a design, the number of lifetime critical components would be reduced to only the main wheel bearing, as this would be supporting both the wheel, the motor rotor and the other rotating parts. This concept would require prototyping to prove its effectiveness. An example of this concept is shown in Figure 6.2. A mechanical launch lock mechanism would be required with such a concept to hold the wheel steady during launch, but this would only be required to operate once to release the wheel, and not approximately half a million times.

The possibility driving the wheel with a stepper motor alone was also investigated. Stepper motors offer a fixed number of small steps that make up the full 360 deg rotation. The rotor aligns with one of these steps and altering the current in the stator coils entices the rotor to the next step. Stepper motors usually have a "self detent torque", a residual force holding the rotor in a certain position in the absence of power in the stator coils, that could be utilized to hold a filter wheel at the required position during a science exposure. If the precise position the rotor occupies in a certain step is within the repeatability requirement of the filter wheel mechanism, then a stepper motor drive system alone could be used in this mechanism. Stepper motors are used extensively in space missions, and they are relatively simple to command. A disadvantage of this method would be that it does not protect against the filter wheel being misaligned as the result of a power failure, but redundant motor windings and redundant drive electronics (as usual for such an application) would reduce this risk.

To assess the suitability of the stepper motor drive concept for this mechanism, repeatability tests were performed on an unloaded representative device[3]. That is to say, how repeatable would the positioning of the filters in the optical beam be with such a drive system? For example, consistency between the filter positioning during the calibration and the science exposures would be important. This stepper motor was tested with and without a 6:1 planetary gear[4]. The advantage of including a gear in the drive system is that the overall mass of the system can be reduced. The repeatability of the drive system with, and without, the gear is shown in Figure 6.4. In these measurements, the drive system was rotated in sets of $10 \times 360$ deg in each direction, with the accuracy of the positioning measured after each rotation by an autocollimator targeting a mirror fixed to the drive systems output axis. That is to say, the motor was rotated ten times in one direction, with measurements taken after each complete rotation, then ten times in the opposite direction, again with measurements taken after each complete rotation, and so on. The difference in the positioning with the two rotation directions can be clearly seen as the steps in the profiles in Figure 6.4. Both the rotation angle $x$ and the transverse angle $y$ were measured after each rotation. Tests were performed with and without holding currents in the

[3]Phytron VSS42.200 cryogenic stepper motor. Phytron-Elektronik GmbH, Germany
[4]Phytron VGPL41.1 cryogenic gear. Phytron-Elektronik GmbH, Germany

motor coils. These currents actively maintain the rotor at a particular step, without them, it is only the motor's self detent torque maintaining the position.

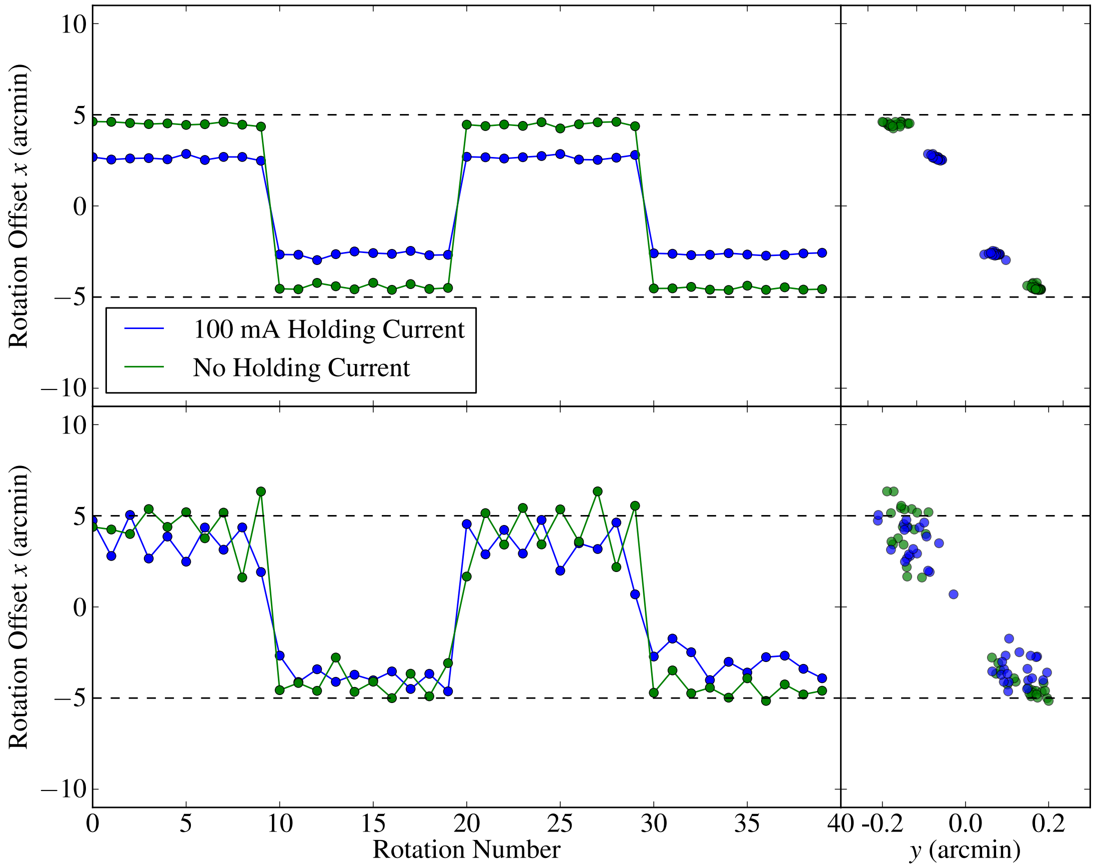


Figure 6.4: The rotational repeatability of an unloaded Phytron VSS42.200 cryogenic stepper motor with (bottom) and without (top) a 6:1 planetary gear (Phytron VGPL41.1 cryogenic gear). Left: The rotational accuracy $x$ to which the drive system returns to a given position. *Ten rotations were performed in each direction, before the rotation direction was reversed.* Right: The same measurements as a function of the transverse repeatability $y$. Data are presented for two cases: (green) no holding current is provided to the motor coils when the drive system reaches its final position and (blue) a 100 mA holding current is maintained in the motor coils after the drive system reaches its target position.

The results from this testing campaign are clear. Without the gear, the stepper motor is able to return to a position with a better than 1 arcmin repeatability *when the rotation angle is kept constant*. When the motor is rotated in the opposite direction, it is also able to a return accurately to a (albeit different) constant position. Maintaining a holding current in the motor coils reduces the offset between the two returned positions, but does not significantly affect the repeatability with a constant rotation direction. When a gear is included in the drive system, the repeatability is far worse. This can be attributed to tolerances within the gear: the gear's "backlash". From these tests, I conclude that a direct drive with a stepper motor could be a potential solution for the near-infrared photometry channel's filter wheel mechanism *if* the rotation direction is kept constant. From these measurements, I also conclude that drive systems with planetary gears are not suitable for this mechanism. Another concern with such a geared system would be its lifetime. Not only would the gear need to survive a large number of operations, but it would also amplify the number of motor rotations required.

With this assessment, I have identified three drive and positioning systems for the channel's filter wheel mechanism. These are: (i) a brushless DC motor with a ratchet system, (ii) a brushless DC motor with a closed loop control system and (iii) direct drive using a stepper motor with a constant rotation direction. A prototyping campaign, at the mechanism's operating temperature (150 K), would be required to down-select these three drive systems for the near-infrared channel's wheel mechanism. Due to changes in the responsibilities within the Euclid Consortium, it was not possible to perform such a campaign before the development of the mechanism was shifted from the Max-Planck-Institut für Astronomie.

**The Bearing System**

The bearing system will be another critical component of the filter wheel mechanism. As introduced in Subsection 6.2.2, the mechanism will have to survive a large number of operations and this will apply stringent requirements on the bearing system. In the filter wheel concept presented in Figure 6.2, the wheel disk is mounted on a duplex bearing pair, which is capable of supporting axial loads in both directions. To reduce launch loads, the center of mass of the rotating parts in the wheel mechanism is designed to fall between the two bearings. Due to the mechanism's operating temperature and environment, fluid lubricants cannot be implemented. Instead a solid lubricant was proposed, specifically molybdenum disulfide ($MoS_2$), which has a large heritage in space missions[5].

## 6.3 Momentum Exported to the Satellite

To accommodate the large optical elements, the wheel concepts presented required a large diameter of $\sim 400$ mm. When rotated, these mechanisms would therefore export a large amount of torque to the satellite (see Section 2.3.5). In this section, I quantify the maximum exported momentum from the mechanism shown in Figure 6.2. This information would be valuable for mission planning, as either the satellite's stabilization system must compensate for this, or an appropriate settling time must be included in the survey strategy. The total mass of the mechanism shown in Figure 6.2, which is typical for the multiple designs considered, is less than 5 kg (including optical elements). The moment of inertia of the rotating parts is $\sim 0.06$ kg m$^2$. The maximum exported angular momentum from the wheel can be estimated with a simple wheel rotation profile. Assuming a 3 s uniform acceleration phase, an 8 s free running phase

[5]For example, see [40].

and a 3 s uniform deceleration phase (and therefore leaving 1 s remaining from the 15 s requirement for settling), the maximum angular momentum exported to the satellite would be $I_{\max} \simeq 4 \times 10^{-3}$ N m s.

## 6.4 Filter Mounting Structure

This chapter now turns its attention to the mounting of the filters to the wheel disk introduced in Subsection 6.2.2. This mounting structure must protect the brittle optical elements during all phases of the mission: the integration, the storage, the launch, the cool down to the channel's operating temperature (150 K) and during the 5+ years of scientific operation. During the Euclid Assessment Study, I identified two concepts for this mounting structure.

### 6.4.1 Design Considerations

These mounting concepts were designed to limit the stresses in the fragile optical elements in all mission phases. The design was therefore driven by two concerns: (i) the vibration loads induced in the assembly during launch and (ii) the stress introduced by inconsistent thermal contractions between the fused silica filters and the titanium (Ti-6Al-4V) filter wheel disk during cool down. To address (i), I required a stiff mount, with high resonant frequencies to avoid the low frequency, high amplitude vibrations from the launcher. To reduce the stresses in the optics from launch vibrations, a large contact area between the filter and the mount was also required. To satisfy (ii), I carefully considered the coefficients thermal expansion (CTEs) of the different materials to ensure that the stresses induced during the cool down from ambient to the operating temperature are minimized. Not only must the optical elements survive this transition, but the mechanical stresses at the operating temperature must be minimal in order not to deform the element and therefore introduce additional wavefront errors in the optical system. Fused silica has a very low thermal expansion coefficient and, in fact, begins to expand under cooling at $\sim 175$ K. A significant mechanical offset of $\sim 82$ μm[6] (in the radius) will be generated between the fused silica elements and the Ti-6Al-4V wheel disk during cool down, and this must be compensated for by the filter mounting structure.

### 6.4.2 Mounting Concepts

In both of the mounting concepts identified, the filters are mounted in an Invar (Type 36) element, which is in turn fixed into a recess in the titanium filter wheel. Invar was chosen for this element as its CTE well matches fused silica's over the required temperature range. The majority of the stresses induced during the cool down would therefore be focused in this element and not in the filter. During the cool down, there would be a $\sim 67$ μm offset (in the radius) at the interface between the Invar element and the Ti-6Al-4V wheel disk, the remaining $\sim 15$ μm

[6] Cryogenic thermal expansion coefficients: Fused Silica - Okaji et al. (1995) [42], Ti-6Al-4V - Cryogenic Material Properties Database [43], Invar - Cryogenic Material Properties Database [43].

offset would be at the interface between the Invar element and the filter. The two mounting concepts only differ at the interface between the Invar element and the filter wheel: in one design a rigid interface is implemented (the "rigid mount") and in the other a flexible interface (the "flexible mount"). In both designs, the Invar element is fixed to the filter wheel disk with $8 \times$ M3 screws. In the flexible mount concept, I cut 0.5 mm strips into the Invar structure at the screw positions to create flexible elements. These are designed to compensate for the offset in the thermal contractions between the Invar element and the Ti-6Al-4V wheel disk. Kapton foil is included between the filter and the metallic components, to prevent small protrusions in these hard materials causing high localized stresses in the optical element. The rigid mounting concept is shown in Figure 6.5 and the flexible concept can be seen in Figure 6.6. In these concepts, the Invar elements (like the filter wheel) will be finished with an optically black coating.

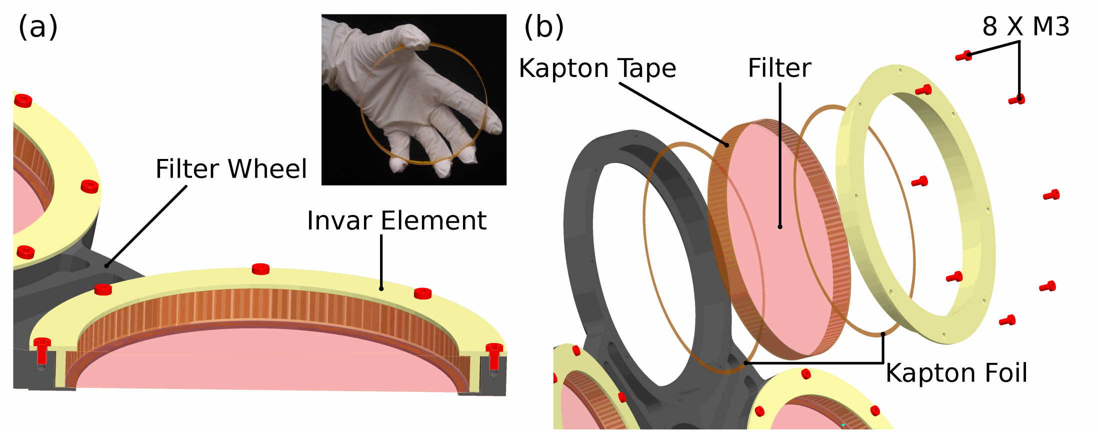


Figure 6.5: The rigid version of the filter mounting concept identified for the near-infrared photometric channel: (a) a cross section through the mount and (b) an exploded view. The large size of the near-infrared filters is shown in the inset. The Kapton tape can be seen around the filter's circumference in preparation for integration into the mount prototypes.

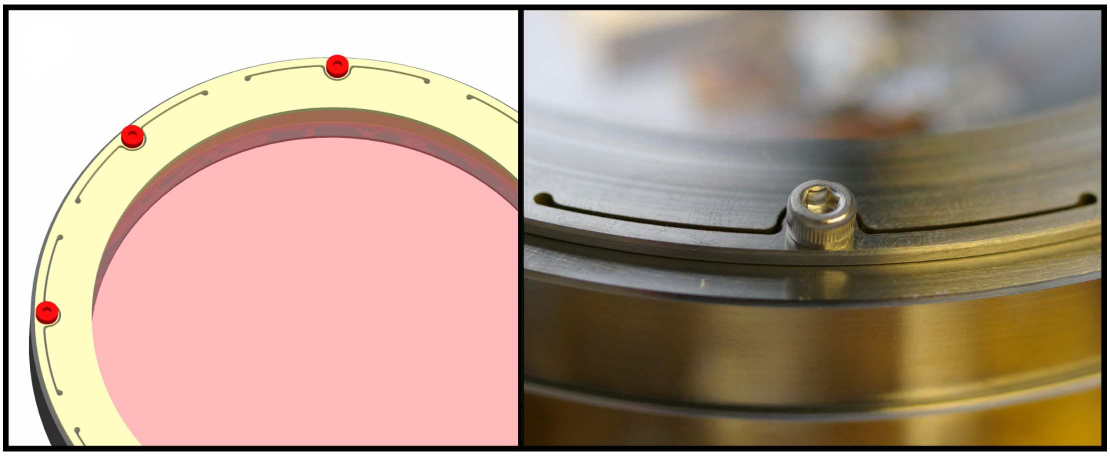

Figure 6.6: Left: The more complex, flexible version of the proposed filter mounting concept. The design is identical to that shown in Figure 6.5 apart from the flexible elements cut into the Invar structure at the screw positions. Right: A close up of the flexible elements on the mount prototype.

### 6.4.3 Finite Element Analysis of the Filter Mounting Concept

I have analyzed the two mounting concepts presented in Subsection 6.4.2 with the *ANSYS* Finite Element Software Package. These simulations included all the main mount components, except for the thin Kapton pieces. In this subsection, I present the analysis conducted on the critical flex elements in the flexible mount, particularly relating to their behavior under launch conditions and cool down. Figure 6.7 shows the stresses induced in the Invar structure under a 50 g static z-axis acceleration; the corresponding stresses in the filter are also shown. The peak stress in the Invar element is $\sim 314$ MPa (yield strength 345 MPa [44]). Note that the vibration levels simulated are at a high "worst-case" magnitude, and in reality the actual levels should be much lower. With this acceleration, the maximum stress in the filter is $< 1$ MPa, well below the limiting stress of fused silica.

To simulate the cool down behavior of the flexible mount, I model the $\sim 67$ μm thermal contraction offset between the Invar element and the Ti-6Al-4V wheel disk as a displacement of the screws by this amount. I therefore made the worst case assumption that the wheel disk and the screws do not flex. I find that the flexible elements can compensate for this offset with a peak stress of $\sim 195$ MPa. If I assume that there is no sliding at the Invar-filter interface, the peak stress in the optics coming from this displacement would be again $< 1.0$ MPa (see Figure 6.8). This is a worst case assumption, as sliding will occur at this interface, especially since Kapton foil is included between these two materials.

These simulations, and others, have validated both mounting concepts. The soft Kapton foil between the hard filter and metal elements has not been considered in this analysis; the inclusion of this would reduce the stresses in the filters, as it would not only provide more padding at the interfaces, it would also permit these surfaces to slide more.

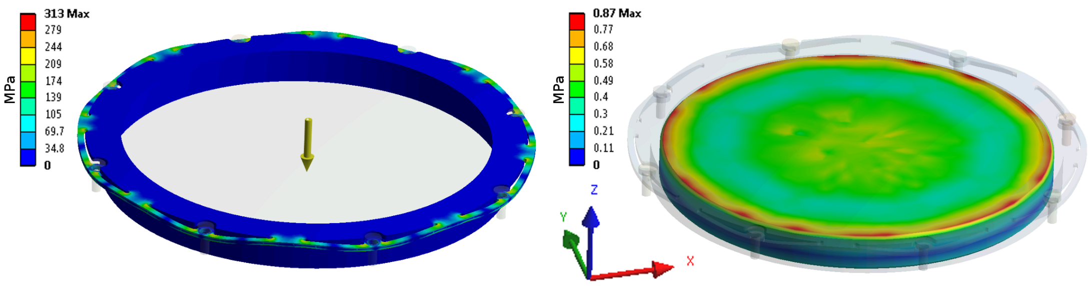


Figure 6.7: Finite element analysis of the flexible mount under 50 g accelerations in the z-axes (yellow arrow). The stresses induced in the Invar structure and the filter are shown on the left and right respectively. The displacement of the flexible elements is magnified by 10. The coordinate system referred to in this chapter is also identified.

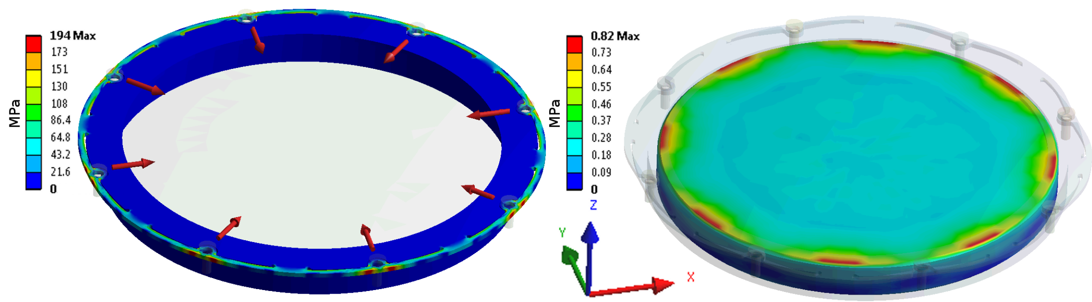


Figure 6.8: Finite element analysis of the flexible elements cut into the flexible mount during cool down. The stresses in the Invar element are shown on the left. The stresses in the filter coming from these displacements are shown on the right, assuming a bonded contact between these two elements (worst case). The red arrows show the direction of the $\sim 67$ µm displacement applied to the 8 screws. The displacement of the flexible elements is magnified by a factor of 5. The coordinate system referred to in this chapter is also shown.

### 6.4.4 Prototyping

Prototypes of both of the mounting concepts have been manufactured at the Fine Mechanics Workshop at the Max-Planck-Institut für Astronomie. For the prototyping campaign, the mounting concepts were tested with mechanical representative filter dummies. These fused silica elements had the same mechanical dimensions as the actual filters, but they were not coated or highly polished. The prototyping campaign did not include a representative wheel disk, instead a locally representative Ti-6Al-4V element was used. These prototypes have been subjected to the cool down and vibration tests discussed in the following subsections.

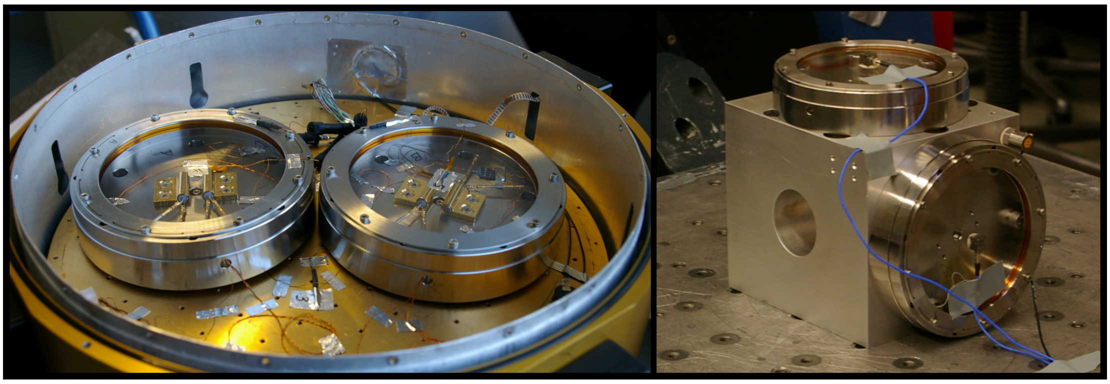

Figure 6.9: Left: The two mount prototypes in the cryostat at Max-Planck-Institut für Astronomie. The prototypes are attached to Ti-6Al-4V filter wheel dummies, which in turn are mounted to Ti-6Al-4V interface elements with heaters (gold) for temperature regulation. For a better temperature control, washers are implemented between the interface elements and the cold baseplate to limit the thermal contact. Right: The filter mount prototypes on the vibration bench at the Umweltlabor at Carl Zeiss Optronics GmbH. An interface cube was used to allow simultaneous testing of both mounts. The three-axis accelerometers can be seen at the center of the filter dummies (blue cables) and the control accelerometer can be seen on the mounting cube (cable not connected).

### Cool Down Tests[7]

A test setup at MPIA has been used to cool the prototypes to the operating temperature. A liquid nitrogen cryostat, with heaters, was used to cool the mounts and maintain a temperature of 150 K for over 24 hours. The test setup can be seen in Figure 6.9 (left). Both mounting structures successfully completed the cool down tests.

### Vibration Tests

The prototypes have been subjected to vibration tests in the x- and z-axes (as defined in Figure 6.7) at the Umweltlabor at Carl Zeiss Optronics GmbH[8] up to the levels given in Tables 6.1 and 6.2. The two prototypes can be seen on the vibration bench in Figure 6.9 (right). Both prototypes were mounted to a common interface cube, allowing simultaneous testing. A three-axis accelerometer was attached to the center of each of the filter dummies.

The response spectra of the two mounts, before and after the vibration testing campaign, can be seen in Figures 6.10 and 6.11. These measurements show that both of the mounting concepts are very stiff. The rigid mount is much stiffer than the flexible mount, with its lowest resonant frequency above 1000 Hz. The first resonant frequency of the flexible mount (pre-testing) was measured at 314 Hz in the z-axis.

The rigid filter mount was successfully vibrated with both sinusoidal and random vibrations

[7] I would like to thank U. Grözinger (MPIA – Germany) for his support with this test.

[8] I would like to thank N. Wittekind and A. Kolb at Carl Zeiss Optronics GmbH for their support with this test.

| Frequency (Hz) | Level (0-peak) |
|---|---|
| 5 – 21 | 9 mm |
| 21 – 60 | 16 g |
| 60 – 100 | 4.8 g |
| Sweep Rate | 2 Oct/min |

Table 6.1: The sinusoidal vibration levels that the filter mount prototypes were tested to. The low frequencies are expressed in displacements and the high level frequencies in accelerations.

| Frequency (Hz) | Level (0-peak) |
|---|---|
| 20 – 100 | +3 dB/oct |
| 100 – 300 | 0.4 $g^2$/Hz |
| 300 – 2000 | −5 dB/oct |
| Overall | 15.15 $g_{RMS}$ |
| Duration | 150 s |

Table 6.2: The random vibration levels that the filter mount prototypes were tested to.

up to the levels given in Tables 6.1 and 6.2 in both the x- and z-axes. The mount and optical element both survived and, as can be seen from Figure 6.10, the shapes of the pre- and post-test response spectra are similar, confirming that there was no significant change in the mechanical properties of the system. I therefore conclude that the rigid filter mount successfully completed the vibration testing campaign.

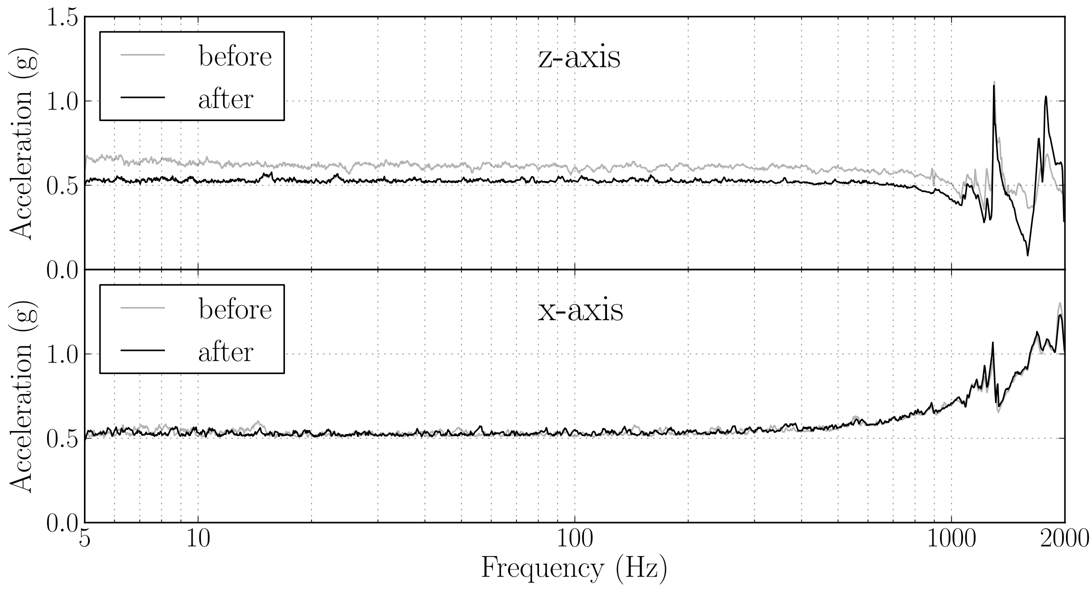


Figure 6.10: The response spectra of the rigid filter mount when driven by a 0.5 g sinusoidal input before (grey) and after (black) the vibration testing campaign. The top and bottom plots show the response spectrum in z- and x-axes respectively, as defined in Figure 6.7. The offset between the z-axes' response spectra is a measurement issue and is not due to a fundamental change in the mount's mechanical properties.

The flexible mount, on the other hand, did not successfully complete the vibration testing campaign. A complete testing run was performed on the x-axis, but the vibration tests had to be aborted prematurely during the tests on the z-axis. For the x-axis tests, the flexible mount was vibrated both with sinusoidal and random vibrations up to the levels shown in Tables 6.1

and 6.2. Although both the optical element and mount survived this test, the optical element rotated by $\sim 5-10^{\circ}$ from its original orientation in the mount. This change can be seen at the higher frequencies of the mount's x-axis response spectra shown in Figure 6.11 (bottom). No such change was observed with the rigid mount. In the z-axis tests, the mount and filter survived the sine-load run to the levels presented in Table 6.1. Due to impact sounds coming from the mount, the z-axis random vibration test was aborted prematurely at dB$=-12$. From Figure 6.11, it is clear that there had been a significant change to the mechanical properties of the mount assembly as the lowest z-axis resonant frequency shifted from 314 Hz to 273 Hz. From this result, and from the rotating of the filter in the x-axis tests, I conclude that the clamping of the filter to the recess in the wheel dummy is not sufficient with the flexible elements cut into the Invar structure. This conclusion is confirmed with the finite element reanalysis of the design presented in the next subsection.

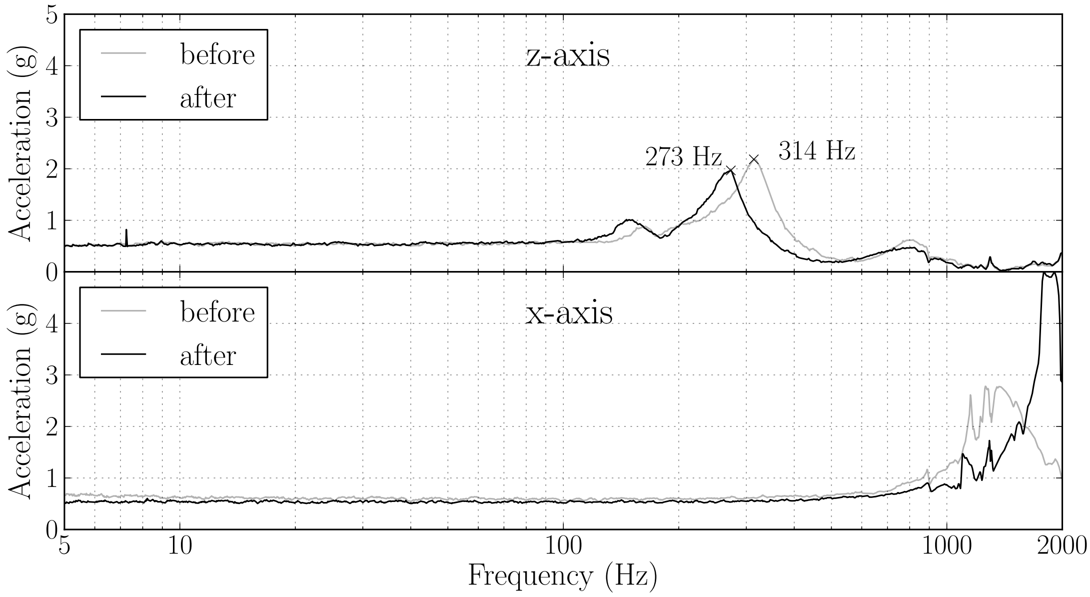


Figure 6.11: The bottom panel shows the x-axis response spectrum of the flexible mount, when driven by a 0.5 g sinusoidal input, before (grey) and after (black) the sinusoidal and random vibrations to the levels given in Table 6.1 and 6.2 respectively. The top panel shows the z-axis response spectrum of the flexible mount, when driven by a 0.5 g sinusoidal input, before (grey) and after (black) the sinusoidal load *only* - the random vibration tests were aborted prematurely.

### 6.4.5 Reanalysis of the Design

The results of the vibration tests of the prototypes suggest that the flexible mount will not be able to clamp the filter securely in place during launch. The design was re-investigated with finite element analysis, with the aim of reproducing the observations. The behavior of the flexible elements was investigated and it was found that a displacement of the filter by 216 μm in the z-axis is expected under a static vibration load of 16 g in this direction, a value consistent with the peak sinusoidal level in Table 6.1. This matches the results of the vibration test and I conclude that the clamping of the filter to the recess in the titanium filter wheel would not be sufficient with these flexible elements.

### 6.4.6 Filter Mount Design Down-Selection

Based on the results from the prototyping campaign, and in particular those from the vibrations tests, I conclude that the rigid mount design is the most appropriate candidate for the near-infrared photometric channel. Although relatively simple, this concept has been validated with the finite element analysis and a prototyping campaign. One of the main conclusions from this work is that, despite the temptation to complexify, sometimes the simplest concepts are the best!

## 6.5 Outlook

Through the work presented in this chapter, I have assessed the feasibility of the near-infrared channel's filter wheel mechanism. This work has identified promising concepts for this mechanism, although a prototyping campaign is now required to develop them further. The critical mounting structures for the filter elements have been considered in more detail. Here, finite element analysis and a prototyping campaign have allowed me to identify a promising solution for this structure. Ultimately, from this work I concluded that this mechanism is feasible and that it should not be a barrier for a successful implementation of the Euclid Mission.

The responsibility for this mechanism and the filter mounting structure has shifted away from the Max-Planck-Institut für Astronomie after the Euclid Assessment Phase. As a result this work was stopped prematurely. Unfortunately, the designs presented here will therefore no longer be developed for the Euclid Mission.

# Chapter 7

# Outlook

The Euclid Mission is currently competing in the last down-selection phase of the European Space Agency's Cosmic Vision Program. If successful, the mission will be launched at the end of the decade. In my opinion, the Euclid Mission is very special. Not only will it address some very fundamental and wide reaching problems with our understanding of the Universe, it will also provide vast datasets that will have a huge legacy value. An almost complete coverage of the extragalactic sky with high precision visible imaging, near-infrared multi-band photometry and near-infrared spectroscopy will impact on many aspects of modern astronomy. Much like with the Sloan Digital Sky Survey, I anticipate that many more scientific papers will come from the legacy science conducted on these datasets than the primary science. I also expect that these datasets will be used in ways that none of us currently working on the project have even considered. Regarding the primary science goals, I see four possible outcome of the mission:

1. That the accelerated expansion of the Universe remains well-explained by a cosmological constant ($w_0 = -1$, $w_a = 0$). This result would be far from boring and would require that the $\sim 10^{60}$ discrepancy between particle physicists' and cosmologists' view of vacuum energy be addressed.

2. That dark energy is found to be an evolving quantity and that the Euclid Mission will constrain its equation of state parameter at multiple cosmological epochs.

3. That a modification to Einstein's General Relative better explains the large scale growth of structure in the Universe, perhaps even making the concepts of dark matter and dark energy obsolete.

4. That the two different science probes, Weak Lensing and Galaxy Clustering, do not give the consistent results expected!

Even if the Euclid Mission is not able to distinguish between these outcomes, I still think that – due to the vast legacy potential – it will be a hugely successful mission. It is this unique quality that makes the Euclid Mission special. I consider myself very lucky to have worked on the Euclid Mission during such an important development phase. I urge the European Space Agency to launch this mission!

# Acknowledgements

I have been lucky enough to work with a fantastic group of people over the last three years and I am very pleased to acknowledge them here. Firstly, I would like to thank Hans-Walter Rix for entrusting me with such a important role within the Euclid Consortium. I hope I carried out my duties as Photometry Instrument Scientist adequately. His support during this time has been invaluable. I would also like to thank Oliver Krause for giving me the opportunity to work at the Max-Planck-Institut für Astronomie and for his support during my thesis. Ulrich Grözinger has been of constant support, particularity in technical matters, and I am very luck to have had the benefit of his knowledge and experience. I also owe Silvia Scheithauer many thanks for her kind support during my time in Germany, both professionally and privately. I would also like to thank Peter Bizenberger and Tom Herbst for patiently answering all my questions. I am very grateful to Armin Huber and Marcus Mellein for their support with the specialist software packages I used during this work. Over the past year, I have also enjoyed working closely with Gregor Seidel and I would like to thank him for all the help he has given me. I would like to thank David W. Hogg not only for working with me in a very fruitful collaboration on self-calibration (Chapter 4), but also for all the little bits of advice and the small tips he has given me on vast range of topics. Armin Böhm and his colleagues at the Fine Mechanical Workshop at the Max-Planck-Institut für Astronomie have also been excellent; they have always manufactured high quality components for me, often on a very short timescale! I would also like to acknowledge Friedrich Müller and Örs Detre for all the helpful tips they have given me over the last three years.

I have also received a lot of support from people outside the Max-Planck-Institut für Astronomie. I would like to thank Mario Schweitzer for his support with my hardware development during the Euclid Assessment Study. Jerome Amiaux has not only been an invaluable source of technical information on Euclid over the last three years, but he has always been willing to help and guide me; for that I am very grateful. I would also like to thank all the members of the NISP Instrument Team who have helped and supported me during my time as the NISP Photometry Scientist.

Finally, I would like to thank everyone at the Max-Planck-Institut für Astronomie for making the last three years so enjoyable!

# Bibliography

[1] R. Laureijs. Euclid Assessment Study Report for the ESA Cosmic Visions. December 2009.

[2] European Space Agency. Euclid Definition Study Report. *ESA/SRE(2011)12*, July 2011.

[3] J. Peacock, P. Schneider, G. Efstathiou, J. R. Ellis, B. Leibundgut, S. Lilly, and Y. Mellier. Report by the ESA-ESO Working Group on Fundamental Cosmology. Technical report, ESA-ESO, September 2006.

[4] N. Jarosik, C. L. Bennett, J. Dunkley, B. Gold, M. R. Greason, M. Halpern, R. S. Hill, G. Hinshaw, A. Kogut, E. Komatsu, D. Larson, M. Limon, S. S. Meyer, M. R. Nolta, N. Odegard, L. Page, K. M. Smith, D. N. Spergel, G. S. Tucker, J. L. Weiland, E. Wollack, and E. L. Wright. Seven-year Wilkinson Microwave Anisotropy Probe (WMAP) Observations: Sky Maps, Systematic Errors, and Basic Results. February 2011.

[5] European Space Agency. Plato Definition Study Report. *ESA/SRE(2011)14*, July 2011.

[6] European Space Agency. Plato Definition Study Report. *ESA/SRE(2011)13*, July 2011.

[7] A. Réfrégier, O. Boulade, Y. Mellier, B. Milliard, R. Pain, J. Michaud, F. Safa, A. Amara, P. Astier, E. Barrelet, E. Bertin, S. Boulade, C. Cara, A. Claret, L. Georges, R. Grange, J. Guy, C. Koeck, L. Kroely, C. Magneville, N. Palanque-Delabrouille, N. Regnault, G. Smadja, C. Schimd, and Z. Sun. DUNE: the Dark Universe Explorer. *SPIE 6265*, July 2006.

[8] A. Cimatti, M. Robberto, C. Baugh, S. V. W. Beckwith, R. Content, E. Daddi, G. De Lucia, B. Garilli, L. Guzzo, G. Kauffmann, M. Lehnert, D. Maccagni, A. Martínez-Sansigre, F. Pasian, I. N. Reid, P. Rosati, R. Salvaterra, M. Stiavelli, Y. Wang, M. Z. Osorio, M. Balcells, M. Bersanelli, F. Bertoldi, J. Blaizot, D. Bottini, R. Bower, A. Bulgarelli, A. Burgasser, C. Burigana, R. C. Butler, S. Casertano, B. Ciardi, M. Cirasuolo, M. Clampin, S. Cole, A. Comastri, S. Cristiani, J.-G. Cuby, F. Cuttaia, A. de Rosa, A. D. Sanchez, M. di Capua, J. Dunlop, X. Fan, A. Ferrara, F. Finelli, A. Franceschini, M. Franx, P. Franzetti, C. Frenk, J. P. Gardner, F. Gianotti, R. Grange, C. Gruppioni, A. Gruppuso, F. Hammer, L. Hillenbrand, A. Jacobsen, M. Jarvis, R. Kennicutt, R. Kimble, M. Kriek,

J. Kurk, J.-P. Kneib, O. Le Fevre, D. Macchetto, J. MacKenty, P. Madau, M. Magliocchetti, D. Maino, N. Mandolesi, N. Masetti, R. McLure, A. Mennella, M. Meyer, M. Mignoli, B. Mobasher, E. Molinari, G. Morgante, S. Morris, L. Nicastro, E. Oliva, P. Padovani, E. Palazzi, F. Paresce, A. Perez Garrido, E. Pian, L. Popa, M. Postman, L. Pozzetti, J. Rayner, R. Rebolo, A. Renzini, H. Röttgering, E. Schinnerer, M. Scodeggio, M. Saisse, T. Shanks, A. Shapley, R. Sharples, H. Shea, J. Silk, I. Smail, P. Spanó, J. Steinacker, L. Stringhetti, A. Szalay, L. Tresse, M. Trifoglio, M. Urry, L. Valenziano, F. Villa, I. Villo Perez, F. Walter, M. Ward, R. White, S. White, E. Wright, R. Wyse, G. Zamorani, A. Zacchei, W. W. Zeilinger, and F. Zerbi. SPACE: the spectroscopic all-sky cosmic explorer. *Experimental Astronomy*, 23:39–66, March 2009.

[9] J. W. Beletic, R. Blank, D. Gulbransen, D. Lee, M. Loose, E. C. Piquette, T. Sprafke, W. E. Tennant, M. Zandian, and J. Zino. Teledyne Imaging Sensors: infrared imaging technologies for astronomy and civil space. *SPIE 7021*, August 2008.

[10] A. Ealet, B. Garilli, and R. Holmes. NISP Performance Analysis Report. Technical Report Version 2.1, Euclid Consortium, July 2011. EUCL-MPI-NPS-RP-00079.

[11] P. Eric, A. Ealet, R. Holmes, and T. Maciaszek. NISP Requirement Flow Down Report. Technical Report Version 1.0, Euclid Consortium, July 2011. EUCL-LAM-NPS-RP-00128.

[12] R. Laureijs. Euclid Science Requirements Document. Technical Report Version 5.8, European Space Agency, July 2011. DEM-SA-Dc-00001.

[13] E. Prieto and The NISP Team. NISP Detector System Report. Technical Report Version 1.0, Euclid Consortium, May 2011. EUCL-LAM-NPS-RP-00094.

[14] O. Boulade. Computation of the zodiacal light background. Technical Report Version 1.0, Euclid Consortium, July 2009. EUCL-TN-0020-CEA.

[15] R. Scaramella and J. Amiaux. Mission Operation Concept Document: Reference Survey. Technical Report Version 4.3.2, Euclid Consortium, July 2011. EUCL-PL-00050-SYS.

[16] A. Ealet and R. Holmes. NISP Calibration Plan. Technical Report Version 1.31, Euclid Consortium, July 2011. EUCL-MPI-NPS-PL-00078.

[17] G. A. Kriss, K. Long, S. Casertano, S Friedman, A. Fullerton, P. McCullough, J. Valenti, R. Van der Marel, and D. Hunter. An end-to-end calibration error budget for the jwst science instruments. Technical report, Space Telescope Science Institute, jan 2007. JWST-STScI-001007.

[18] R. Holmes, O. Krause, and H.-W. Rix. Justification of the NISP Instrument's Calibration Source. Technical Report Version 0.1, Euclid Consortium, March 2011. EUCL-NISP-TN-009.

[19] F. Bortoletto, C. Bonoli, L. Corcione, S. Ligori, E. Giro, M. D'Alessandro, and L. Nicastro. NISP FPA On-Board Pre-Processing Description. Technical report, Euclid Consortium, August 2011. EUCL-OPD-NPS-TN-00134.

[20] N. Padmanabhan, D. J. Schlegel, D. P. Finkbeiner, J. C. Barentine, M. R. Blanton, H. J. Brewington, J. E. Gunn, M. Harvanek, D. W. Hogg, Ž. Ivezić, D. Johnston, S. M. Kent, S. J. Kleinman, G. R. Knapp, J. Krzesinski, D. Long, E. H. Neilsen, Jr., A. Nitta, C. Loomis, R. H. Lupton, S. Roweis, S. A. Snedden, M. A. Strauss, and D. L. Tucker. An Improved Photometric Calibration of the Sloan Digital Sky Survey Imaging Data. *The Astrophysical Journal*, 674:1217–1233, February 2008.

[21] L. Valenziano and M. Trifoglio. NISP Instrument Operation Concept Document. Technical Report Version 1.1, Euclid Consortium, July 2011. EUCL-IIO-NPS-PL-077.

[22] R. A. Windhorst, S. H. Cohen, N. P. Hathi, P. J. McCarthy, R. E. Ryan, Jr., H. Yan, I. K. Baldry, S. P. Driver, J. A. Frogel, D. T. Hill, L. S. Kelvin, A. M. Koekemoer, M. Mechtley, R. W. O'Connell, A. S. G. Robotham, M. J. Rutkowski, M. Seibert, A. N. Straughn, R. J. Tuffs, B. Balick, H. E. Bond, H. Bushouse, D. Calzetti, M. Crockett, M. J. Disney, M. A. Dopita, D. N. B. Hall, J. A. Holtzman, S. Kaviraj, R. A. Kimble, J. W. MacKenty, M. Mutchler, F. Paresce, A. Saha, J. I. Silk, J. T. Trauger, A. R. Walker, B. C. Whitmore, and E. T. Young. The Hubble Space Telescope Wide Field Camera 3 Early Release Science Data: Panchromatic Faint Object Counts for 0.2-2 $\mu$m Wavelength. April 2011.

[23] P. Eric. NI-OMA Design Definition Report. Technical Report Version 1.0, Euclid Consortium, May 2011. EUCL-LAM-NPS-RP-00092.

[24] N. Padmanabhan, D. J. Schlegel, D. P. Finkbeiner, J. C. Barentine, M. R. Blanton, H. J. Brewington, J. E. Gunn, M. Harvanek, D. W. Hogg, Ž. Ivezić, D. Johnston, S. M. Kent, S. J. Kleinman, G. R. Knapp, J. Krzesinski, D. Long, E. H. Neilsen, Jr., A. Nitta, C. Loomis, R. H. Lupton, S. Roweis, S. A. Snedden, M. A. Strauss, and D. L. Tucker. An Improved Photometric Calibration of the Sloan Digital Sky Survey Imaging Data. February 2008.

[25] J. S. Kalirai and A. Rajan. The Photometric Performance and Calibration of WFC3. *The 2010 STScI Calibration Workshop*, 2010.

[26] R. Holmes, P. Bizenberger, O. Krause, M. Schweitzer, and A. M. Glauser. The Euclid near-infrared calibration source. *SPIE 7731*, June 2010.

[27] J. Amiaux, J. L. Augures, O. Boulade, C. Cara, S. Paulin-Henriksson, A. Refregier, R. Ronayette, A. Amara, A. M. Glauser, C. Dumesnil, A. Di Giorgio, J. Booth, M. Schweitzer, R. Holmes, M. Cropper, and E. Atad-Ettedgui. Euclid imaging channels: from science to system requirements. *SPIE 7731*, June 2010.

[28] A. M. Glauser, J. Amiaux, J. L. Augures, S. Lilly, and A. Refregier. An optical shutter for the Euclid imager. *SPIE 7731*, June 2010.

[29] Micro-Glühlampen-Gesellschaft Menzel GmbH, Germany. Catalog #3. `http://www.mgg-lamps.de/`, 2009.

[30] Labsphere, Inc., USA. Space-grade Spectralon material. `http://www.labsphere.com/productdetail.aspx?id=334`. Data Sheet.

[31] J. A. Walker, M. M. Pavlov, and M. L. Byers. Characterization of the solar diffuser as the primary standard for onboard calibration of the Moderate Resolution Imaging Spectroradiometer. *SPIE 3498*, December 1998.

[32] B. Chommeloux, G. Baudin, G. Gourmelon, J.-L. Bezy, C. van Eijk-Olij, J. G. Schaarsberg, H. G. Werij, and E. Zoutman. Spectralon diffusers used as in-flight optical calibration hardware. October 1998.

[33] E.A Early, P.Y. Barnes, B.C. Johnson, J.J Butler, C.J Bruegge, S.F. Biggar, P.R. Spyak, and M.M. Pavlov. Bidirectional Reflectance Round-Robin in Support of the Earth Observing System Program. *Journal of Atmospheric and Oceanic Technology*, 17(8):1077–1091, August 2000.

[34] M. Schweitzer, R. Bender, R. Katterloher, F Eisenhauer, R. Hofmann, R. Holmes, O. Krause, H. W. Rix, J. Booth, P. Fagrelius, J. Rhodes, S. Seshadri, A. Refregier, J. Amiaux, J. L. Augures, O. Boulade, C. Cara, A. Amara, S. Lilly, E. Atad-Ettedgui, A. Di Giorgio, and L. Duvet. NIP: the near-infrared imaging photometer for Euclid. *SPIE 7731*, June 2010.

[35] Acktar Ltd., Israel. Advanced Coatings. `http://www.acktar.com/`. Data Sheet.

[36] R. Holmes, U. Grözinger, O. Krause, and M. Schweitzer. A filter wheel mechanism for the Euclid near-infrared imaging photometer. *SPIE 7731*, July 2010.

[37] R. Holmes, U. Grözinger, P. Bizenberger, and O. Krause. A Filter Mount for the Euclid Mission. *SPIE 7731*, August 2011.

[38] Heraeus. Quartz Glass for Optics, Data and Properties. Data Sheet. `http://www.optics.heraeus-quarzglas.com`.

[39] ASM Aerospace Specification Metals Inc. Titanium Ti-6Al-4V (Grade 5) Technical Data. Data Sheet. `http://www.aerospacemetals.com/`.

[40] O. Krause, F. Müller, S. Birkmann, A. Böhm, M. Ebert, U. Grözinger, T. Henning, R. Hofferbert, A. Huber, D. Lemke, R.-R. Rohloff, S. Scheithauer, T. Gross, T. Fischer, G. Luichtel, H. Merkle, M. Übele, H.-U. Wieland, J. Amiaux, R. Jager, A. Glauser, P. Parr-Burman,

and J. Sykes. High-precision cryogenic wheel mechanisms of the JWST/MIRI instrument: performance of the flight models. *SPIE 7739*, July 2010.

[41] K. Weidlich, M. Fischer, M. M. Ellenrieder, T. Gross, J.-C. Salvignol, R. Barho, C. Neugebauer, G. Königsreiter, M. Trunz, F. Müller, and O. Krause. High-precision cryogenic wheel mechanisms for the JWST NIRSpec instrument. *SPIE 7018*, July 2008.

[42] M. Okaji, N. Yamada, K. Nara, and H. Kato. Laser interferometric dilatometer at low temperatures: application to fused silica SRM 739 . *Cryogenics*, 1995.

[43] E.D. Marquardt, J.P. Le, and R. Radebaugh. Cryogenic Material Properties Database. pages 681–687. Springer US, May 2007.

[44] Eagle Alloys Corporation. Invar 36 Technical Data. Data Sheet. `http://www.eaglealloys.com/`.